Impacts of Degradation on Water, Energy, and Carbon Cycling of the Amazon Tropical Forests

Marcos Longo[1,1], Sassan S. Saatchi[1], Michael Keller[2,2], Kevin W. Bowman[3,3], Antonio Ferraz[4,5], Paul R Moorcroft[6,6], Douglas Morton[7,8], Damien Bonal[9], Paulo Brando[10], Benoît Burban[11,11], Géraldine Derroire[12,12], Maiza Nara dos-Santos[13,13], Victoria Meyer[14,15], Scott Saleska[16,16], Susan Trumbore[17,17], Grégoire Vincent[18,19], Sassan Saatchi[15], Damien Bonal[20], and Paulo Brando[21]

[1]Jet Propulsion Laboratory, California Institute of Technology
[2]USDA Forest Service
[3]Jet Propulsion Lab (NASA)
[4]Unknown
[5]NASA Jet Propulsion Laboratory,University of California Los Angeles Institute of the Environment and Sustainability
[6]Harvard University
[7]Goddard Space Flight Center (NASA)
[8]NASA Goddard Space Flight Center
[9]INRA
[10]Woods Hole Research Center
[11]INRAE UMR 0745 EcoFoG
[12]CIRAD
[13]Brazilian Agricultural Research Corporation
[14]Jet Propulsion Laboratory
[15]NASA Jet Propulsion Laboratory
[16]University of Arizona
[17]Max Planck Institute for Biogeochemistry
[18]Institut de Recherche pour le Developpement
[19]Univ Montpellier, IRD, CIRAD, CNRS, INRAE
[20]INRAE Centre Grand-Est Nancy
[21]University of California Irvine,Instituto de Pesquisa Ambiental da Amazônia

November 30, 2022

Abstract

Selective logging, fragmentation, and understory fires directly degrade forest structure and composition. However, studies addressing the effects of forest degradation on carbon, water, and energy cycles are scarce. Here, we integrate field observations and high-resolution remote sensing from airborne lidar to provide realistic initial conditions to the Ecosystem Demography Model (ED–2.2) and investigate how disturbances from forest degradation affect gross primary production (GPP), evapotranspiration (ET), and sensible heat flux (H). We used forest demography information retrieved from airborne lidar samples (13,500 ha) and calibrated with 817 inventory plots (0.25 ha) across precipitation and degradation gradients in the Eastern Amazon as initial

conditions to ED-2.2 model. Our results show that the magnitude and seasonality of fluxes were modulated by changes in forest structure caused by degradation. During the dry season and under typical conditions, severely degraded forests (biomass loss [?] 66%) experienced water-stress with declines in ET (up to 34%) and GPP (up to 35%), and increases of H (up to 43%) and daily mean ground temperatures (up to 6.5°C) relative to intact forests. In contrast, the relative impact of forest degradation on energy, water, and carbon cycles markedly diminishes under extreme, multi-year droughts, as a consequence of severe stress experienced by intact forests. Our results highlight that the water and energy cycles in the Amazon are not only driven by climate and deforestation, but also the past disturbance and changes of forest structure from degradation, suggesting a much broader influence of human land use activities on the tropical ecosystems.

Impacts of Degradation on Water, Energy, and Carbon Cycling of the Amazon Tropical Forests

Marcos Longo[1],Sassan Saatchi[2,3],Michael Keller[2,4,5],Kevin Bowman[2],António Ferraz[2,3],Paul R. Moorcroft[6],Douglas C Morton[7], Damien Bonal[8],Paulo Brando[9,10,11],Benoît Burban[12],Géraldine Derroire[13],Maiza N dos-Santos[5],Victoria Meyer[2],Scott Saleska[14],Susan Trumbore[15],Grégoire Vincent[16]

[1]NASA Postdoctoral Program Fellow, Jet Propulsion Laboratory, California Institute of Technology, Pasadena CA, United States
[2]Jet Propulsion Laboratory, California Institute of Technology, Pasadena, CA, United States
[3]Institute of Environment and Sustainability, University of California, Los Angeles, CA, United States
[4]International Institute of Tropical Forestry, USDA Forest Service, Rio Piedras, Puerto Rico
[5]Embrapa Informática Agropecuária, Campinas, SP, Brazil
[6]Department of Organismic and Evolutionary Biology, Harvard University, Cambridge, MA, United States
[7]NASA Goddard Space Flight Center, Greenbelt, MD, United States
[8]Université de Lorraine, INRAE, AgroParisTech, UMR Silva, F-54000 Nancy, France
[9]Department of Earth System Science, University of California, Irvine, CA, United States
[10]Woods Hole Research Center, Woods Hole, MA, United States
[11]Instituto de Pesquisa Ambiental da Amazônia, Brasília, DF, Brazil
[12]Institut National de Recherche en Agriculture, Alimentation et Environnement (INRAE), UMR 0745 EcoFoG, Campus Agronomique, Kourou 97379, France
[13]Centre de Coopération Internationale en Recherche Agronomique pour le Développement (CIRAD), UMR EcoFoG (Agroparistech, CNRS, INRAE, Université des Antilles, Université de Guyane), Campus Agronomique, Kourou 97379, France
[14]University of Arizona, Tucson, AZ, United States
[15]Max-Planck-Institut für Biochemie, Jena, Germany
[16]AMAP, Univ Montpellier, IRD, CIRAD, CNRS, INRAE, Montpellier, 34000 France

Key Points:

- Airborne lidar can be used to inform degradation-driven changes in structure to vegetation models

Corresponding author: Marcos Longo, mdplongo@gmail.com

- Forest degradation typically depletes evapotranspiration and productivity and increases flammability
- Extreme droughts reduce functional differences between degraded and intact tropical forests

Abstract

Selective logging, fragmentation, and understory fires directly degrade forest structure and composition. However, studies addressing the effects of forest degradation on carbon, water, and energy cycles are scarce. Here, we integrate field observations and high-resolution remote sensing from airborne lidar to provide realistic initial conditions to the Ecosystem Demography Model (ED–2.2) and investigate how disturbances from forest degradation affect gross primary production (GPP), evapotranspiration (ET), and sensible heat flux (H). We used forest structural information retrieved from airborne lidar samples ($13,500\,\text{ha}$) and calibrated with 817 inventory plots ($0.25\,\text{ha}$) across precipitation and degradation gradients in the Eastern Amazon as initial conditions to ED-2.2 model. Our results show that the magnitude and seasonality of fluxes were modulated by changes in forest structure caused by degradation. During the dry season and under typical conditions, severely degraded forests (biomass loss $\geq 66\%$) experienced water-stress with declines in ET (up to 34%) and GPP (up to 35%), and increases of H (up to 43%) and daily mean ground temperatures (up to 6.5°C) relative to intact forests. In contrast, the relative impact of forest degradation on energy, water, and carbon cycles markedly diminishes under extreme, multi-year droughts, as a consequence of severe stress experienced by intact forests. Our results highlight that the water and energy cycles in the Amazon are not only driven by climate and deforestation, but also the past disturbance and changes of forest structure from degradation, suggesting a much broader influence of human land use activities on the tropical ecosystems.

Plain Language Summary

In the Amazon, timber extraction and forest fires ignited by people are the chief causes of damages that we call forest degradation. Degradation is as widespread as deforestation, and changes how forests behave. Degraded forests may pump less water to the atmosphere and absorb less carbon dioxide from the atmosphere. To understand the differences in behavior between degraded and intact forests, we used high-resolution scanning laser data collected from aircraft flights over regions in the Amazon where we knew if and when forests were degraded. Then, we provided these data to a computer program that calculates the exchange of water and carbon between the forest and the atmosphere. We found that, during the dry season, degraded forests are 6.5°C warmer, pump 1/3 less water (i.e., $40,000\,\text{L}\,\text{ha}^{-1}\,\text{month}^{-1}$), absorb 1/3 less carbon (i.e., $1\,\text{tonC}\,\text{ha}^{-1}\,\text{month}^{-1}$),

and show higher fire risk than intact forests. To our surprise, when the Amazon is hit by severe droughts, intact forests start to behave like degraded forests, because all forests run out of water and become hot. Our results are important because they show that forest degradation caused by people can have large impacts on dry-season climate and favor more fire, especially during typical, non-drought years.

1 Introduction

Tropical forests account for 25–40% of total carbon stocks in terrestrial ecosystems (Sabine et al., 2004; Meister et al., 2012), but their maintenance and functioning have been weakened by climate and land-use change. As a result, tropical forests may shift to net sources of carbon to the atmosphere, with residence time of carbon in forests declining by 50% (Davidson et al., 2012; Grace et al., 2014; Lewis et al., 2015; Erb et al., 2016). Land use and land cover changes contribute to nearly 15% of total annual carbon emissions (Harris et al., 2012; Friedlingstein et al., 2019). However, most studies assessing the effects of land use change on tropical forest stocks and fluxes have focused on the effects of deforestation (e.g., Harris et al., 2012; Achard et al., 2014). Logging, understory fires and forest fragmentation — collectively known as *forest degradation* (Hosonuma et al., 2012) — could play a comparable role in the forest's energy, water, and carbon cycle and induce locally warmer and drier conditions that could be detrimental to their functioning (Grossiord et al., 2020; Sullivan et al., 2020), but these effects remain poorly quantified.

Significant fractions of the remaining tropical forests are located within 1 km from the forest's edge (Haddad et al., 2015; Lewis et al., 2015) and thus are probably degraded (Asner et al., 2006; Morton et al., 2013; Pütz et al., 2014; Tyukavina et al., 2016; Potapov et al., 2017). The area impacted by forest degradation in the Amazon each year is highly uncertain, but likely comparable to deforestation (Asner et al., 2006; Morton et al., 2013; Tyukavina et al., 2017). Total carbon losses attributable to degradation may be similar or exceed deforestation-related losses in tropical forests (Berenguer et al., 2014; Pearson et al., 2017; Baccini et al., 2017; Aragão et al., 2018; Erb et al., 2018), and degradation may even dominate the carbon losses in indigenous lands and protected areas (Walker et al., 2020). At the local scale, carbon stocks in degraded forests are extremely variable. Lightly disturbed forests (e.g., reduced-impact logging) store as much carbon as intact forests, while forests impacted by severe or multiple disturbances may lose a significant

fraction or nearly all of their original carbon stocks (Berenguer et al., 2014; Alamgir et al., 2016; Longo et al., 2016; Rappaport et al., 2018; Ferraz et al., 2018). Transitions between lightly and heavily degraded forests may be non-linear and abrupt (Brando et al., 2014). Unquestionably, estimates of fluxes from forest degradation and regeneration are more uncertain than emissions from deforestation (Aragão et al., 2014; Morton, 2016; Bustamante et al., 2016), because their impacts on forests are more subtle than deforestation and thus more difficult to detect and quantify with traditional remote sensing techniques.

Selective logging and fires also modify the forest structure, composition and functioning. For example, selective logging in the tropics generally targets large trees (diameter at breast height, DBH $\geq$ 40–60 cm) from a few marketable species (e.g., Feldpausch et al., 2005; Blanc et al., 2009; Pinagé et al., 2019), but the other logging structures such as skid trails and log decks kill or damage mostly small trees (DBH $<$ 20 cm) (Feldpausch et al., 2005). Likewise, fire mortality decreases with tree size and the bark thickness (e.g., Brando et al., 2012; Pellegrini et al., 2016), although areas disturbed by recurrent fires also show significant losses of large trees (Barlow et al., 2003; Martins et al., 2012; Brando, Silvério, et al., 2019; Silvério et al., 2019). Consequently, degradation creates more open canopies and thinner understory (e.g., d'Oliveira et al., 2012; Pinagé et al., 2019; Silvério et al., 2019) and increased abundance of grasses and fast-growing, low wood-density tree species (Barlow et al., 2016; Both et al., 2019; Brando, Silvério, et al., 2019).

Previous studies indicate an increase in dry-season length in parts of the Amazon where both deforestation and forest degradation are pervasive (e.g., Fu et al., 2013; Sena et al., 2018), and that the onset of the wet season is modulated by forest transpiration (J. S. Wright et al., 2017). Temperature and vapor pressure deficit (VPD), important drivers of evapotranspiration (ET), were found by Kapos (1989) to be significantly higher near forest edges. Likewise, Jucker et al. (2018) installed a network of micrometeorological measurements across a study area in Sabah, Malaysia, that included intact forests, a broad range of degraded forests and oil-palm plantations, and found that forest structure, along with topographic features, explained most of the variance in understory temperature. Yet, only a few studies on experimental sites quantified the magnitude, seasonality, and interannual variability of water, and energy cycles in degraded forests. For example, S. D. Miller et al. (2011) analyzed the impact of reduced-impact, low-intensity selective logging in the Amazon using eddy covariance towers and found only minor im-

pacts of logging on sensible and latent heat fluxes. Recently, Brando, Silvério, et al. (2019) compared eddy covariance data from two towers at an experimental fire site in the Amazon forest, and found declining differences in gross primary productivity and small differences in evapotranspiration between the control and burned area between 4 and 8 years after the last burn.

Field inventory plots are fundamental to sample the structure and species composition of tropical forests, but they also have important limitations to characterize the heterogeneity of degraded landscapes. First, the number of plots required to characterize stands increase with heterogeneity, often reaching impractical numbers (Marvin et al., 2014). In addition, most tropical forest degradation occurs in private landholdings and privately managed logging concessions, where limited access by researchers may create sampling bias towards well-managed areas, which generally experience less intensive degradation. However, airborne laser scanning (airborne lidar) can circumvent these limitations over large areas with sub-meter resolution. Airborne lidar data have been used successfully to quantify structural characteristics of the canopy such as height and leaf area distribution (Hunter et al., 2013; Vincent et al., 2017; Shao et al., 2019). Moreover, these data have also been used to quantify changes in canopy structure and carbon stocks at local to regional scale that experienced multiple levels of degradation (e.g., Asner et al., 2010; Longo et al., 2016; Ferraz et al., 2018; Meyer et al., 2019).

Numerical models can be used to understand the links between changes in forest structure, light and water availability for different local plant communities, and the overall impact on energy, water, and carbon fluxes between forests and the atmosphere. In the past, *big-leaf* models have been modified to account for the long-term impacts of selectively logged tropical forests on the carbon cycle of tropical forests (e.g., Huang et al., 2008; Huang & Asner, 2010). However, big-leaf models generally do not represent the mechanisms that control access and availability of light and water in complex and heterogeneous forest structures (D. Purves & Pacala, 2008; Fisher et al., 2018) (but see Braghiere et al., 2019). Individual-based models can represent the changes in the population structure and micro-environments due to degradation (R. Fischer et al., 2016; Maréchaux & Chave, 2017), but the complexity and computational burden of these simulations often limit their application to single sites. Cohort-based models, such as the Ecosystem Demography (ED-2.2) model (Medvigy et al., 2009; Longo, Knox, Medvigy, et al., 2019), strike a balance between these end-members because they can efficiently represent the

horizontal and vertical heterogeneity of forests. However, to represent the impact of heterogeneity in the energy, water, and carbon cycles, it is critical that these models are informed with realistic initial conditions that capture the landscape variability and they accurately represent the complex interactions between climate and the micro-environment variability. Previous studies using a variety of cohort-based models have demonstrated that cohort-based models can realistically reproduce the micro-environment heterogeneity and the long-term dynamics of ecosystems, compared to both individual-based models (Moorcroft et al., 2001; Strigul et al., 2008) and observations (D. W. Purves et al., 2008; Longo, Knox, Levine, et al., 2019; Koven et al., 2019).

In this study, we use airborne lidar data to quantify forest structure variability across the Amazon in order to provide critical initial conditions for ecosystem demography models. We also investigate the role of forest degradation on the Amazon forest productivity, flammability, as well as the degradation impacts on the water and energy cycles. Specifically, we seek to answer the following questions:

1. What are the relationships between degradation metrics (e.g. biomass loss) and changes in carbon, water, and energy fluxes, and how does it vary across seasons and regions with different rainfall regimes?
2. How do droughts affect the relationships between degradation and ecosystem functioning?
3. Does forest degradation make Amazon forests more susceptible to fires? If so, which parts of the Amazon experience the largest flammability response to degradation?

To this end, we integrate field inventory plots with high-resolution airborne lidar data over five study regions in the Eastern Amazon along a precipitation gradient and with a broad range of anthropogenic disturbance histories, to provide initial conditions to ED-2.2 that realistically represent the structural diversity of degraded forests. While limited to specific regions in the Amazon where detailed degradation information exists, our goal is to provide a framework that can be extended to larger scales, including biome- and pantropical scales.

193 ## 2 Materials and Methods

194 ### 2.1 Study regions

195 We selected five study regions across a gradient of disturbance and climate con-
196 ditions where ground and airborne lidar are available to study the forest function (Fig-
197 ure 1; Table 1). Three of these sites include eddy covariance tower measurement of en-
198 ergy, water, and carbon dioxide fluxes for comparison with the model simulations, and
199 have been the focus of several ecological studies in the past. Additional details on the
200 disturbance history of each region are available at Text S1.

201 1. *Paracou, French Guiana (GYF)* is a field station where a logging experiment was
202 conducted between 1987 and 1988 that includes intact forest controls and three
203 selective logging treatments: timber extraction using conventional logging tech-
204 niques, timber extraction and canopy thinning, and timber and fuelwood extrac-
205 tion followed by canopy thinning (Gourlet-Fleury et al., 2004). The eddy covari-
206 ance tower at the site is located in the undisturbed forest and has been operational
207 since 2004 (Guyaflux; Bonal et al., 2008).
208 2. *Belterra, Brazil (BTE).* Over the past 100 years, this region experienced cycles
209 of economic growth and recession that created a complex landscapes dominated
210 by deforestation, degradation and second-growth. The Tapajós National Forest
211 is this region, and has areas of intact forests and selectively logged forests using
212 reduced-impact techniques (VanWey et al., 2007; Pyle et al., 2008; Lei et al., 2018).
213 An eddy covariance tower known as Km 67 overlaps with one of the surveyed sites
214 and has data for 2001–2005, and 2008–2011 (Hayek et al., 2018).
215 3. The *Paragominas, Brazil (PRG)* region used to be within the largest timber pro-
216 duction area in Brazil and has undergone selective logging since the 1970s (Veríssimo
217 et al., 1992). Since the 1990s, the economy has shifted towards agriculture, intro-
218 ducing large-scale deforestation such that nearly half of the original forest cover
219 has been lost, and most of the remaining areas have been logged (Pinto et al., 2009).
220 4. *Feliz Natal, Brazil (FZN)* is located at the southern fringe of the Amazon in a mo-
221 saic landscape of soybean fields, grazing lands, and logged forests. This region reg-
222 ularly experiences severe dry seasons and frequent understory fires (Morton et al.,
223 2013; Rappaport et al., 2018).

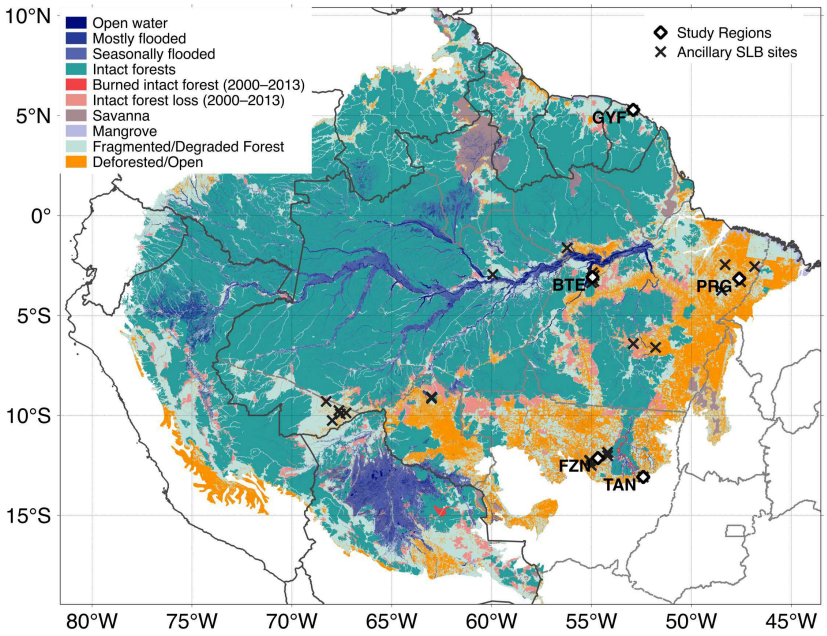

Figure 1. Location of the five study regions within the Amazon biome region, along with land classification as of 2013. Intact forest and intact forest loss were obtained from Potapov et al. (2017); open and deforested areas were obtained from PRODES-INPE (2018) (Brazil) and areas with tree cover below 20% according to Hansen et al. (2013) (other countries); wetlands and water bodies in the Amazon River Basin were from Hess et al. (2015) and savannas and mangroves were obtained from Olson et al. (2001).

5. *Tanguro, Brazil (TAN)* is located in an experimental fire study area within a larger landscape covered by intact forests and forests that were disturbed with low-intensity understory fires (one, three, and six times) between 2004 and 2010 (Balch et al., 2008; Brando et al., 2014). The surveyed region also includes two eddy covariance towers that have been operating since 2014 both at the intact and burned forests (Brando, Silvério, et al., 2019).

These five study regions were sampled at multiple sites by small-footprint, multiple-return airborne lidar. The lidar data provided both the terrain elevation at high spatial resolution (1-m) and detailed information about the vertical structure of forests from a uniform point cloud density to meet a minimum return density of 4 returns per m^2 over 99.5% of the area (Leitold et al., 2015). Living trees of diameter at breast height DBH $\geq$ 10 cm were either botanically identified (experimental plots in GYF) or identified from field characteristics by local parataxonomists. To characterize the disturbance history,

Table 1. Overview of the study regions, including mean annual precipitation (MAP) and dry-season length (DSL).

Region (Code)	Coordinates	MAP[a] [mm]	DSL[b] [mo]	Lidar [ha]	Inventory [ha]	Disturbances[c]
Paracou (GYF)	5.28°N; 52.91°W	3040	2(0)	963	79.8	INT, CL1, LTH
Belterra (BTE)	3.09°S; 54.95°W	1890	5(1)	4057	16.7	INT, RIL, BN1, BN2, BN3
Paragominas (PRG)	3.15°S; 47.61°W	1850	6(2)	3217	35.6	INT, RIL, CL1, BN1, LB1, BN2, BN3
Feliz Natal (FZN)	12.14°S; 54.68°W	1940	5(4)	4210	14.0	INT, CL1, CL2, BN1, LB1, BN2, BN3
Tanguro (TAN)	13.08°S; 52.41°W	1800	5(4)	1006	22.9	INT, BN1, BN3, BN6

[a] Source for mean annual precipitation (MAP) data: GYF – Gourlet-Fleury et al. (2004); other regions – nearest site available at INMET (2019).
[b] Dry-season length (DSL): number of months with precipitation below 100 mm; numbers in parentheses indicate number of severely dry months (precipitation below 30 mm).
[c] Disturbance history classes: INT – intact; RIL – reduced-impact logging; CLx – conventional logging (x times); LTH – conventional logging and thinning; LB1 – conventional logging and burned (once); BNx – burned x times.

we used either published information from the experimental regions GYF (Gourlet-Fleury et al., 2004; Bonal et al., 2008; Wagner et al., 2013) and TAN (Brando et al., 2012, 2014), or the disturbance history analysis from (Longo et al., 2016), which was based on a visual interpretation of the Normalized Burn Ratio (NBR) of cloud-free Landsat images since 1984, and complemented with information from logging companies for the reduced-impact logging sites (e.g., Pinagé et al., 2019). Details on site-specific data used in this study are available in Text S2 and previous work (Longo et al., 2016; Vincent et al., 2017; Brando, Silvério, et al., 2019), and were obtained through the Paracou Experimental Station and the Sustainable Landscapes Brazil data servers (Paracou Portal, 2016; Sustainable Landscapes Brazil, 2019; dos-Santos et al., 2019).

2.2 Overview of the modeling framework

In this study, we used the Ecosystem Demography model, version 2.2 (ED-2.2) (Moorcroft et al., 2001; Medvigy et al., 2009; Longo, Knox, Medvigy, et al., 2019) to simulate the impacts of forest structure on energy, water, and carbon cycles. For any point of interest, the ED-2.2 model simulates the forest structure and functional diversity across a landscape, and simulates the energy, water, and carbon budgets for multiple canopy environments, which represent the forest heterogeneity (Longo, Knox, Medvigy, et al., 2019). ED-2.2 has been successfully evaluated and used in both short-term and long-term studies in the Amazon forest (Powell et al., 2013; Zhang et al., 2015; Levine et al., 2016; Longo, Knox, Levine, et al., 2019). In ED-2.2, the horizontal and vertical heterogeneities of forests are represented through a hierarchical structure. Each area with the same climate (e.g.,

footprint of an eddy covariance tower or a grid cell in a gridded meteorological driver) is called a *polygon*. Each polygon is subdivided into *patches*, which represent collections of forest gaps within a polygon that share a similar age since last disturbance and same disturbance type (although not necessarily contiguous in space). Patches are further subdivided into *cohorts*, which are collections of individual plants that have similar size and similar functional group. Importantly, because ED-2.2 incorporates the horizontal heterogeneity of the plant community structure and composition, the model can efficiently incorporate and simulate the dynamics of degraded forests.

Most of the ED-2.2 modules used in this study have been previously described in Longo, Knox, Medvigy, et al. (2019). The main changes used in this study include (1) a modified height-diameter allometry based on the Jucker et al. (2017) approach and locally collected field data that can be used consistently by the initialization and model; (2) an improved allocation to living and structural tissues, which is now based on more recent allometric equations (Chave et al., 2014; Falster et al., 2016) and datasets (Falster et al., 2015); (3) a revised photosynthesis solver, which now accounts for the maximum electron transport ratio and the maximum triose-phosphate utilization (von Caemmerer, 2000; Oleson et al., 2013; Lombardozzi et al., 2018); (4) updated values of traits that are used to define trade-offs in tropical plant functional types in ED-2.2 (wood density and leaf turnover rate), and updated the trade-off relationships of traits that directly or indirectly influence gross primary productivity and light- and water-use efficiency (specific leaf area and leaf carbon:nitrogen ratio, maximum carboxylation rate, maximum electron transport ratio and maximum triose-phosphate utilization), using multiple studies and trait databases, including GLOPNET, TRY, and NGEE-Tropics (I. J. Wright et al., 2004; Santiago & Wright, 2007; Chave et al., 2009; Kattge et al., 2009, 2011, 2020; Baraloto et al., 2010; Powers & Tiffin, 2010; Gu et al., 2016; Bahar et al., 2017; Norby et al., 2017). These changes are described in Text S3. Moreover, we used an approach developed by X. Xu (unpublished) and based on Lloyd et al. (2010) to account for light-dependent plasticity of three leaf traits (specific leaf area, leaf turnover rate, and carboxylation capacity), and calibrated using existing data (Lloyd et al., 2010; Russo & Kitajima, 2016; Keenan & Niinemets, 2016).

To obtain initial conditions for ED-2.2 from airborne lidar, we devised a multi-step approach that links airborne lidar data with ecosystem properties (Figure 2). Here we provide a summary of the initialization procedure; the technical details of this approach

are described in Text S4. For step 1, we split all collected point cloud data into 50×50 m columns, simulated waveforms from the discrete returns (Blair & Hofton, 1999; Popescu et al., 2011; Hancock et al., 2019) to obtain unscaled leaf area density profiles based on the vertical distribution of returns (e.g., MacArthur & Horn, 1969; Ni-Meister et al., 2001; Stark et al., 2012; Antonarakis et al., 2014; Tang & Dubayah, 2017), and assigned the relative proportion of each plant functional type provided by one of the 769 training plots that had the most similar vertical structure; the similarity was based on the profile comparison that yielded the smallest Kolmogorov-Smirnov statistic. The vertical profile was split into cohort layers centered around local maxima or saddle points, using a modified procedure based on function `peaks` (package `RSEIS`, Lees, 2017) of the `R` statistical software (R Core Team, 2019). For step 2, we used a collection of 817 forest inventory plots (0.16–0.26 ha) that were also surveyed by airborne lidar, which included plots from all study regions as well additional sites available from Sustainable Landscapes Brazil (SLB) and used in a previous study (ancillary SLB sites, Figure 1; Longo et al., 2016); we developed statistical models based on subset selection of regression (A. J. Miller, 1984) and heteroskedastic distribution of residuals (Mascaro et al., 2011) to estimate plot-level properties (aboveground biomass, basal area, stem number density, leaf area index) from point cloud metrics and field estimates, following the approach by Longo et al. (2016). For step 3, we sought to obtain a plot-specific scaling factor to the leaf area density profile that produced the best agreement between the four estimated plot-level properties from step 1 and the plot-level properties obtained by integrating the vertical distribution from step 2, by minimizing the sum of relative square differences of the four properties. For step 4, we analyze the scaling factor distribution for all plots for which we could test the approach, and define a unique and global scaling factor, based on the median scaling factor, that is used to correct all predicted profiles.

Once we obtained the initial conditions for each 50×50 m column, we grouped individual columns based the disturbance history (degradation level) and the study region (Table 1). We used the following broad categories for disturbance history: intact (INT), reduced-impact logging (RIL), conventional logging (CLx, where x is the number of logging disturbances), conventional logging and thinning (LTH), logged and burned once (LB1) and burned (BNx, where x is the number of burns). Importantly, we did not perform any averaging or sampling of the individual columns before providing them to ED-

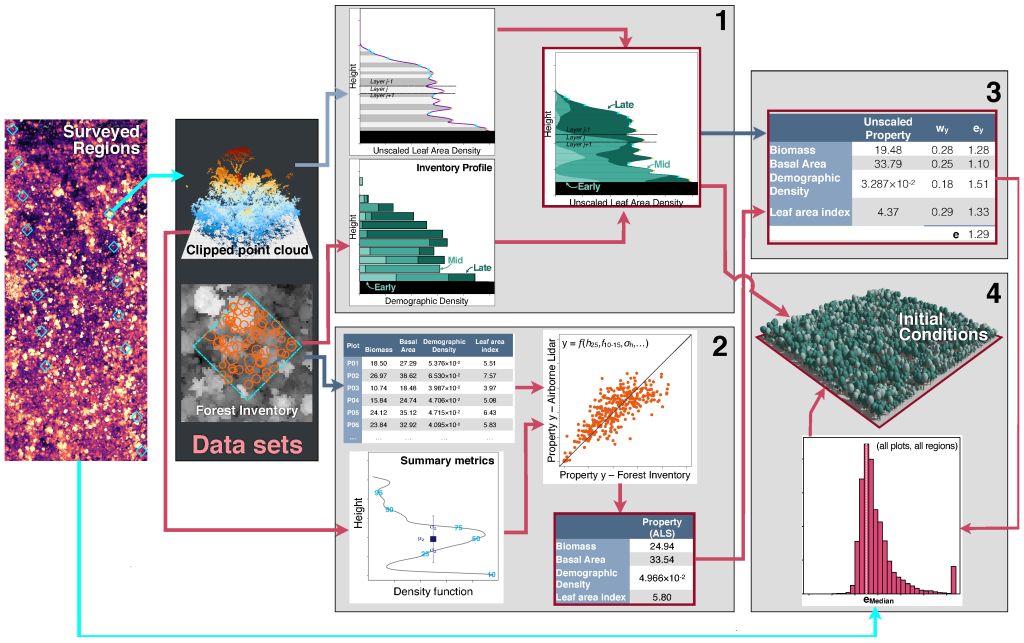

Figure 2. Schematic representation of the method to obtain initial conditions for ED-2 from airborne lidar. Each light box represents one step in the procedure. The results of each step are highlighted with a red border. Dark blue arrows are stages that require individual-based allometric equations, and light blue arrows are stages that require a light extinction model.

2.2; instead, we provided all columns to the model, so the initial conditions characterize the observed distribution of forest structures that exist within each group.

2.3 Assessment of the modeling framework

We evaluated three characteristics to assess the ability of model framework to represent the forest structure heterogeneity caused by degradation, and to represent components of the energy, water, and carbon cycle. First, we quantified the ability of the airborne lidar initialization to capture the differences in forest structure caused by degradation. Second, we assessed whether the model can realistically represent fluxes and storage of water, energy and carbon across different regions. Third, we compared the model sensitivity to degradation-driven effects on fluxes and storage with independent observations.

To evaluate the airborne lidar initialization, we used a cross-validation approach in which we replicated the procedure described above (Section 2.2) 2000 times, using a

hierarchical bootstrap approach. We first sampled regions (with replacement), to ensure that some regions would be entirely excluded from the replicate, then we sampled plots (also with replacement), to ensure that the replicate had the same number of plots as the original training data set. We then predicted the structure of all plots in the excluded regions, using iterations that did not have any plot in the training data set; to make this number consistent across regions, we used the smallest number of iterations that met this criterion across all regions (n = 612). Finally, for each region, we compared the average forest structure from all cross-validation replicates that excluded the region from the training stage. Because estimates of forest properties have larger uncertainties in smaller plots (Chave et al., 2004; Meyer et al., 2013; Mauya et al., 2015), we only evaluated the method when a disturbance class within a region had at least 20 plots.

To verify the model's ability to realistically represent the regional variability of fluxes and storage, we carried out ED-2.2 simulations initialized with airborne lidar for the intact forests regions where eddy covariance tower and forest inventory plots co-located with airborne lidar were available (GYF and BTE). Region TAN had two eddy-covariance towers, one within the footprint of the burned forests and a second in intact forest (Brando, Silvério, et al., 2019), which allowed us to contrast the model's predicted impacts of degradation on fluxes and biophysical properties with the pair of tower measurements.

2.4 Model configuration and analyses

Our main focus is to understand the role of degradation-driven changes in forest structure in altering both the state and the fluxes of energy, water, and carbon, both under typical and extreme climate. To account for regional differences in climate and to sample a broad range of interannual variability, we used time series of meteorological drivers pooled from gridded reanalyses (one set of time series per region). For most meteorological variables required by ED-2.2 (pressure, temperature, humidity, incoming shortwave and longwave radiation, and winds), we used $0.625° \times 0.5°$, hourly averages (1980–2016) from the version 2 of the Modern-Era Retrospective Analysis for Research and Applications (MERRA-2, Gelaro et al., 2017). MERRA-2 precipitation is known to have significant negative biases in the tropics (Beck et al., 2019); therefore we used the $0.1° \times 0.1°$, 3-hourly precipitation rates from the version 2 of the Multi-Source Weighted Ensemble Precipitation product (MSWEP-2, Beck et al., 2019). To ensure that the only difference between simulations in the same study region was the distribution of forest structures,

we imposed the same edaphic conditions: free-drainage soils with 8 m deep, and nearly equal fractions of sand (32%), silt (34%), and clay (34%). To avoid confounding effects from post-disturbance mortality and recovery, all simulations were carried out without enabling dynamic vegetation, such that the differences in forest structure would remain the same for the entire time series, and all differences between simulations in the same region could be attributable to well-characterized differences in forest structure. However, disabling dynamic vegetation also precluded us from investigating the effects of climate-driven changes in the canopy structure on the energy, water, and carbon cycle, and thus potentially increasing biases in our estimates of fluxes following extreme events such as droughts.

To investigate the role of degradation on fire risk, we built on the original fire model from ED-1 (Moorcroft et al., 2001) to determine when fire-prone conditions would occur in each patch. The flammable area α_F ($\%\,\mathrm{yr}^{-1}$) is calculated from the fire disturbance rate λ_F (yr^{-1}):

$$\alpha_F = 100\,\left[1-\exp\left(-\lambda_F\,\Delta t\right)\right], \tag{1}$$

$$\lambda_F = \begin{cases} I\,C_{\mathrm{Fuel}} & \text{, if } \left[\dfrac{1}{|z_F|}\displaystyle\int_{z_F}^{0}\vartheta\left(z\right)\mathrm{d}z\right] < \left(1-f\right)\,\vartheta_{\mathrm{Wp}}+f\,\vartheta_{\mathrm{Fc}} \\ 0 & \text{, otherwise} \end{cases}. \tag{2}$$

where $\Delta t = 1\,\mathrm{yr}$; $I = 0.5\,\mathrm{m^2\,kgC\,yr^{-1}}$ is a fire intensity parameter; $z_F = 30\,\mathrm{cm}$ is the depth of the soil layer used to estimate dryness; ϑ ($\mathrm{m^3\,m^{-3}}$) is the soil moisture; ϑ_{Wp} is the permanent wilting point and ϑ_{Fc} is the field capacity, both defined as in Longo, Knox, Medvigy, et al. (2019); and $f = 0.02$ is a phenomenological parameter that defines dry conditions. The values of I and f were selected based on the results from a previous model evaluation using ED-2.2 (Longo, Knox, Levine, et al., 2019). Because understory fires are the dominant type of fire in the Amazon (A. Alencar et al., 2006; Morton et al., 2013), we considered fuels to be comprised by above-ground litter, above-ground coarse woody debris, and above-ground biomass from grasses and seedlings (trees with height $< 2\,\mathrm{m}$); canopy trees were not considered to be fuels. The fire parameterization, although simple, has been previously demonstrated to capture the general features of fire regime across tropical South America (Longo, Knox, Levine, et al., 2019).

3 Results

3.1 Evaluation of the model initialization and simulated seasonal dynamics

The ED-2.2 model initialization approach from airborne lidar (Figure 3) captured the main differences in forest structure and composition, both across study regions and along degradation gradients. To illustrate the initialization, we focus on the basal area distribution obtained from cross-validation at disturbance histories within study regions that had at least 20 plots (Figure 3). At sites GYF, PRG, and TAN, the airborne lidar initialization predicted the total basal area with absolute biases ranging from 3% (GYF) to 13% (TAN), and root mean square error of the order of 18–27% (Figures 3c, 3f and 3i). The largest absolute discrepancies occurred for intermediate-sized trees ($20 \leq$ DBH $< 40\,$cm) at GYF and PRG, where the airborne lidar initialization underestimated basal area by 2.9 and $4.3\,\mathrm{cm^2\,m^{-2}}$, respectively (Figures 3c and 2f). The largest overestimation of airborne lidar was observed among larger trees ($60 \leq$ DBH $< 100\,$cm) in intact forests at GYF ($2.4\,\mathrm{cm^2\,m^{-2}}$; Figure 3c). The size distribution of most degraded forests were well characterized (Figures 3a-b, 3d-e and 3g); the largest deviations from inventory were observed in logged and burned forests in PRG, where airborne lidar underestimated total basal area by $3.0\,\mathrm{cm^2\,m^{-2}}$ (Figure 3d). Likewise, the initialization algorithm represented the higher relative abundance of early successional plants in the most degraded sites, and the dominance of mid- and late-successional plants at intact forests at GYF and PRG (Figure S1), and realistically represented the leaf area distribution across regions and degradation levels (Figure S2).

ED-2.2 simulations using forest inventory and airborne lidar as initial conditions were compared with eddy covariance tower estimates of all sites (Figures 4 and S4-S9, and Table S1). Gross primary productivity (GPP) generally showed small biases relative to tower estimates (-0.046 to $+0.394\,\mathrm{kgC\,m^{-2}\,yr^{-1}}$), and relatively small errors (less than observed variability) at all sites, regardless of the initial conditions (Figure 4; Table S1). While the GPP seasonality was correctly represented at GYF, the model did not capture the late wet-season decrease and early dry-season increase of GPP at BTE, and it showed a delayed dry-season decline GPP at TAN compared to tower estimates (Figure S4). Net ecosystem productivity (NEP), on the other hand, showed significant biases, large errors, and relatively small correlation with tower estimates (Figure 4; Ta-

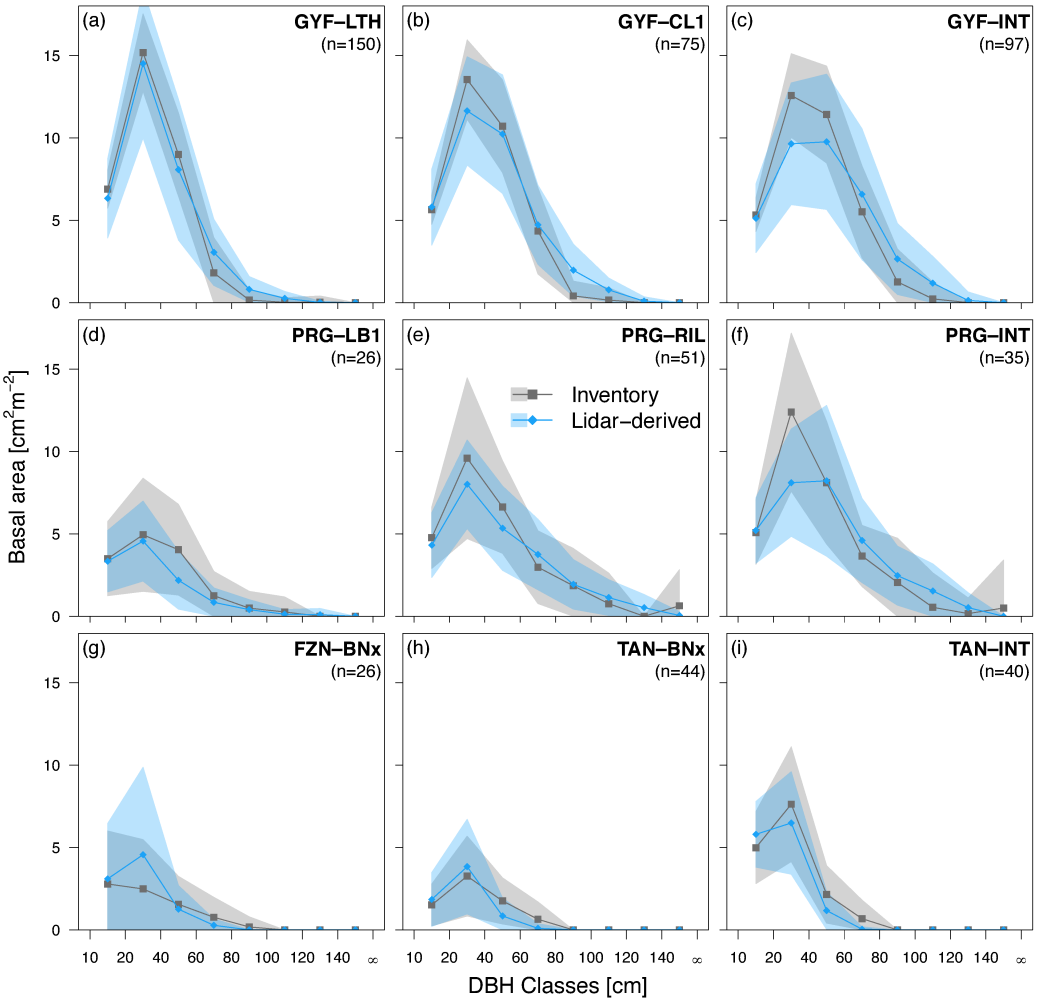

Figure 3. Assessment of basal area distribution as a function of diameter at breast height (DBH) for different study regions and degradation levels. Grey points are obtained from forest inventory plots, and blue points are obtained from the airborne lidar initialization (Figure 2) using a 612-fold regional cross-validation (i.e. excluding all plots from region in the calibration stage). Bands around points correspond to the standard deviation either across all plots in the same category (inventory) or across all plots and replicates (lidar). Sites: GYF – Paracou, PRG – Paragominas, FZN – Feliz Natal, TAN – Tanguro. Disturbance classes: BNx – Burned twice or more, CL1 – conventional logging (once), LB1 – logged and burned once, LTH – logged and thinned, RIL – reduced-impact logging, INT – intact. Additional comparisons are shown in the Supporting Information: basal area as functions of plant functional type (Figure S1); leaf area index profiles as functions of height (Figure S2); comparisons for Belterra (BTE-RIL) (Figure S3).

ble S1), which were driven by excessive seasonality of heterotrophic respiration (Figure S5). Because the initial carbon stocks in necromass pools are uncertain, and the results on magnitude and seasonality of ecosystem respiration (and consequently NEP) are inconsistent with tower estimates, we will not discuss the simulation results in terms of respiration and NEP.

Water fluxes also showed small biases relative to the observed variability at GYF, TNF and TAN (Burned), regardless of the initialization (-0.01 to $+0.54\,\mathrm{mm\,day^{-1}}$; Figures 4a and 4c; Table S1); biases at TAN (Intact) were larger ($0.69-0.82\,\mathrm{mm\,day^{-1}}$). With the exception of TAN (Burned), the correlation between ED-2.2 and tower was high at daily averages (Figures 4b and 4d; Table S1). At TAN (Burned), the poorer agreement with tower estimates was caused by the model predicting a similar seasonality of water flux at both control and burned forests, whereas towers suggest an increase in water flux during the earlier part of the dry season (Figure S6). ED-2.2 predictions of sensible heat flux had high correlation with observations at all sites (Figures 4b and 4d; Table S1), although sensible heat flux shows significant biases at BTE, and dampened seasonality at GYF and TAN (Burned) (Figures 4a and 4c; Table S1; Figure S6). Outgoing shortwave radiation correctly captured the seasonality at the wettest sites, but it did not capture the sharp dry-season increase at TAN (Figure S8), which may be associated with dry-season leaf senescence and shedding that was likely underestimated by ED-2.2. In addition, ED-2.2 simulations overestimated outgoing longwave radiation at all sites except at TAN (Burned) using inventory initialization (Figure S9). Nonetheless, the seasonality and the intra-seasonal variation of outgoing longwave radiation were correctly captured by ED-2.2, resulting in generally high correlation and small standard deviation of residuals at most sites (Figure 4; Table S1).

3.2 Degradation effects on seasonality of fluxes

From ED-2.2, we found that forest degradation can have substantial impacts on the ecosystem function such as evapotranspiration (ET) or ground temperature in severely or recently degraded forests, and in parts of the Amazon with a longer dry season. At GYF, the airborne lidar survey sampled only intact forests and areas that were logged 25 years prior to the data acquisition: consequently, the average water vapor flux and ground temperature were nearly indistinguishable across degraded and intact forests (Figures 5a,S10a). At the equatorial sites, degradation effects were small during the wet sea-

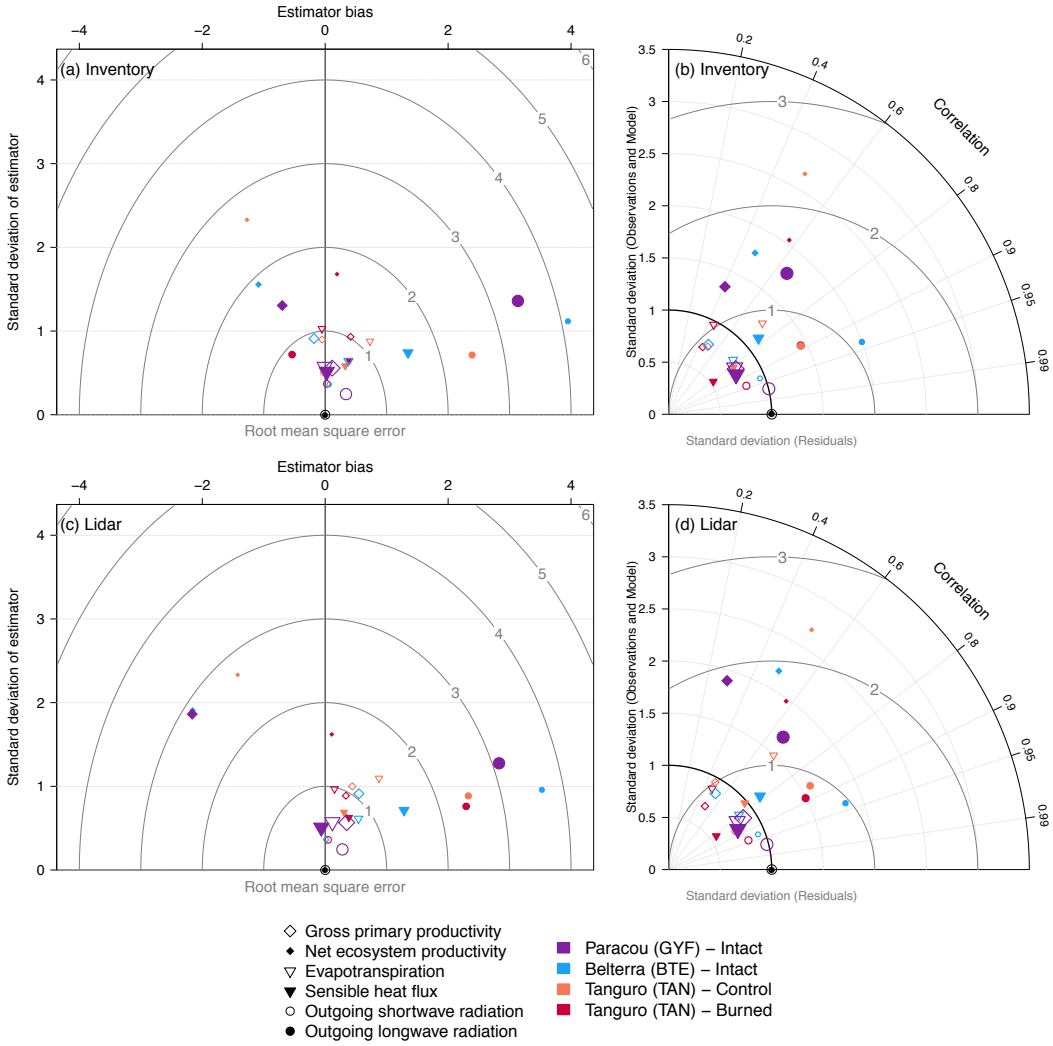

Figure 4. Summary of ED-2.2 model assessment using eddy covariance towers as benchmarks, using simulations initialized with forest inventory and airborne lidar. (a,c) Bias-variance diagram and (b,d) Taylor diagram of multiple daily-averaged fluxes of carbon, energy, and water for Paracou (GYF), Belterra (BTE) and Tanguro (TAN, control and burned), for simulations initialized with (a,b) forest inventory plots and (c,d) airborne lidar. In the bias-variance diagram, bias (x axis), standard deviation of residuals (y axis) and root mean square error (concentric arcs) are normalized by the standard deviation of observations, as is the standard deviation of models in the Taylor diagram. In both diagrams, $\odot$ corresponds to the perfect model prediction. In all plots, we only compare daily averages of days with no measurement gaps. Comparisons of the seasonal cycle for all variables included in the diagrams are available at Figures S4-S9.

son but showed marked reduction in ET (2.1–6.7% in BTE and 4.3–31.8% in PRG) and increase in daytime temperature (0.4–0.9°C in BTE and 1.0–6.0°C in PRG) during the dry season, with the largest changes relative to intact forests found at burned areas (Figures 5b, 5c, S10b,c). At the southern (driest) sites, the seasonal changes were even more pronounced: at both FZN and TAN, ET decreased by 21–25% early in the dry season (Jun) at the most severely burned forests, whereas ET in intact forests peaked in the middle of the dry season (Jul–Aug; Figures 5d and 5e). Similarly, burned forests were warmer year-round than intact forests at the southern sites (FZN and TAN), with minimum warming during the wet season (Dec–Mar; 0.5–0.8°C), and maximum warming occurring at the peak of the dry season (Jul–Aug; 1.0–6.5°C; Figures S10d and S10e).

Importantly, the ED-2.2 results in Figures 5 and S10 emerge from the different distribution of forest structures associated with degradation histories. ED-2.2 accounts for the diversity of forest structures within each disturbance history by means of patches; each patch represents a different forest structure found within any disturbance regime, and patch area is proportional to the probability of finding such forest structure (Longo, Knox, Medvigy, et al., 2019). For example, the ground temperature is consistently warmer at the low biomass patches, but the differences between the lowest and highest patch temperatures are as low as 1°C at GYF (Figure 6a) and less than 4°C during the wet season even at the southern regions (Figures 6d and 6e). In contrast, differences along biomass gradients exceed 9°C during the dry season at all regions except GYF (Figure 6).

Likewise, when all simulated patches are considered, we observe strong coherence between biomass and gross primary productivity (GPP) across all regions and throughout the year (Figures 7 and S11). However, the effect of local communities on GPP is seasonal: differences in typical GPP between low-biomass and high-biomass patches do not exceed $1.1\,\mathrm{kgC\,m^{-2}\,yr^{-1}}$ during the wettest months (Figures 7a–7c), whereas the range of GPP reaches $0.7\,\mathrm{kgC\,m^{-2}\,yr^{-1}}$ at the short dry-season at GYF and exceeds $2.0\,\mathrm{kgC\,m^{-2}\,yr^{-1}}$ during the dry season at the most degraded and driest sites (Figures 7e and 7f). Similar effects were observed in evapotranspiration, where differences along biomass are the strongest during the dry season (Figure S12).

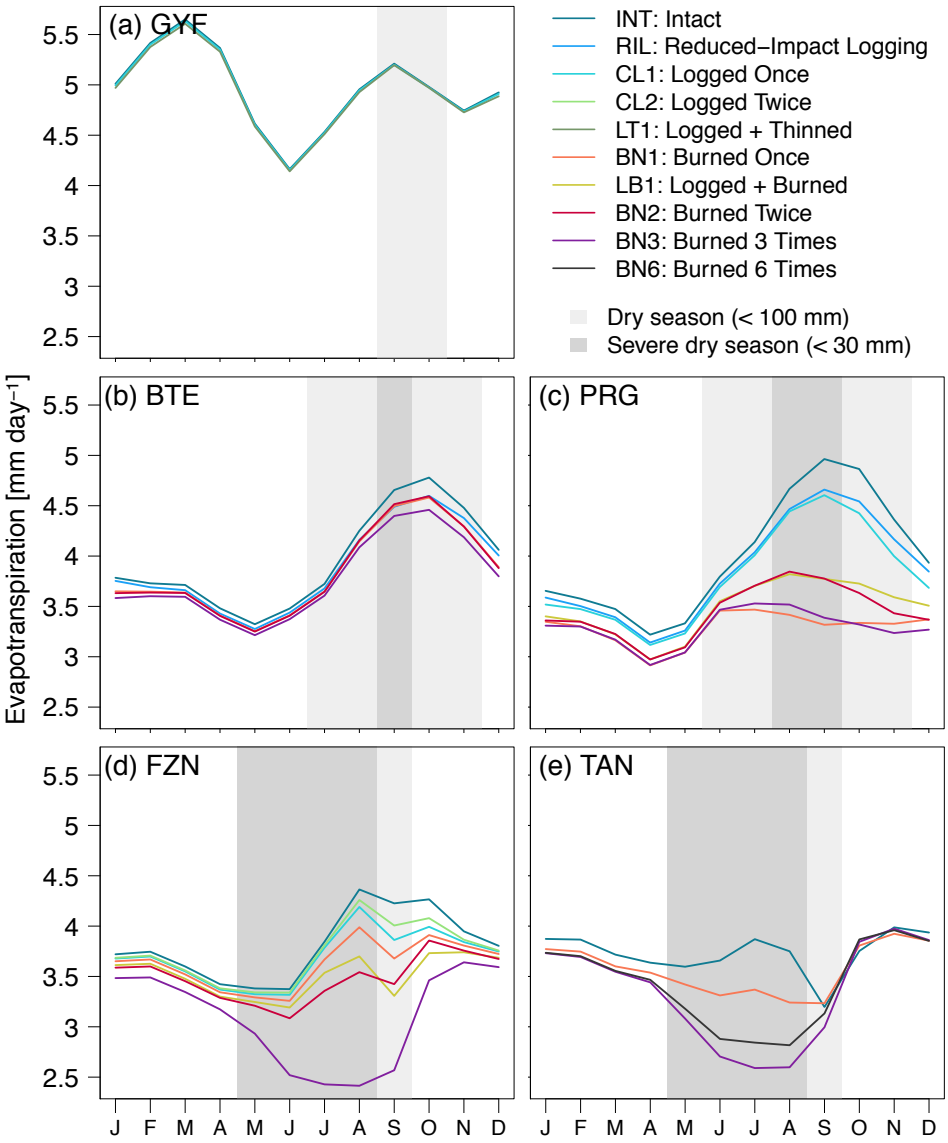

Figure 5. Monthly mean evapotranspiration (ET) as a function of region and degradation. Monthly averages correspond to the 1980–2016 period, simulated by ED-2.2 for (a) Paracou (GYF), (b) Belterra (BTE), (c) Paragominas (PRG), (d) Feliz Natal (FZN), and (e) Tanguro (TAN), aggregated by degradation history within each region (lines). Grey rectangles in the background correspond to the average dry season.

3.3 Degradation impacts on forest flammability

The impact of forest degradation on ecosystem functioning showed important year-to-year variability, and differences between intact and degraded forests were generally

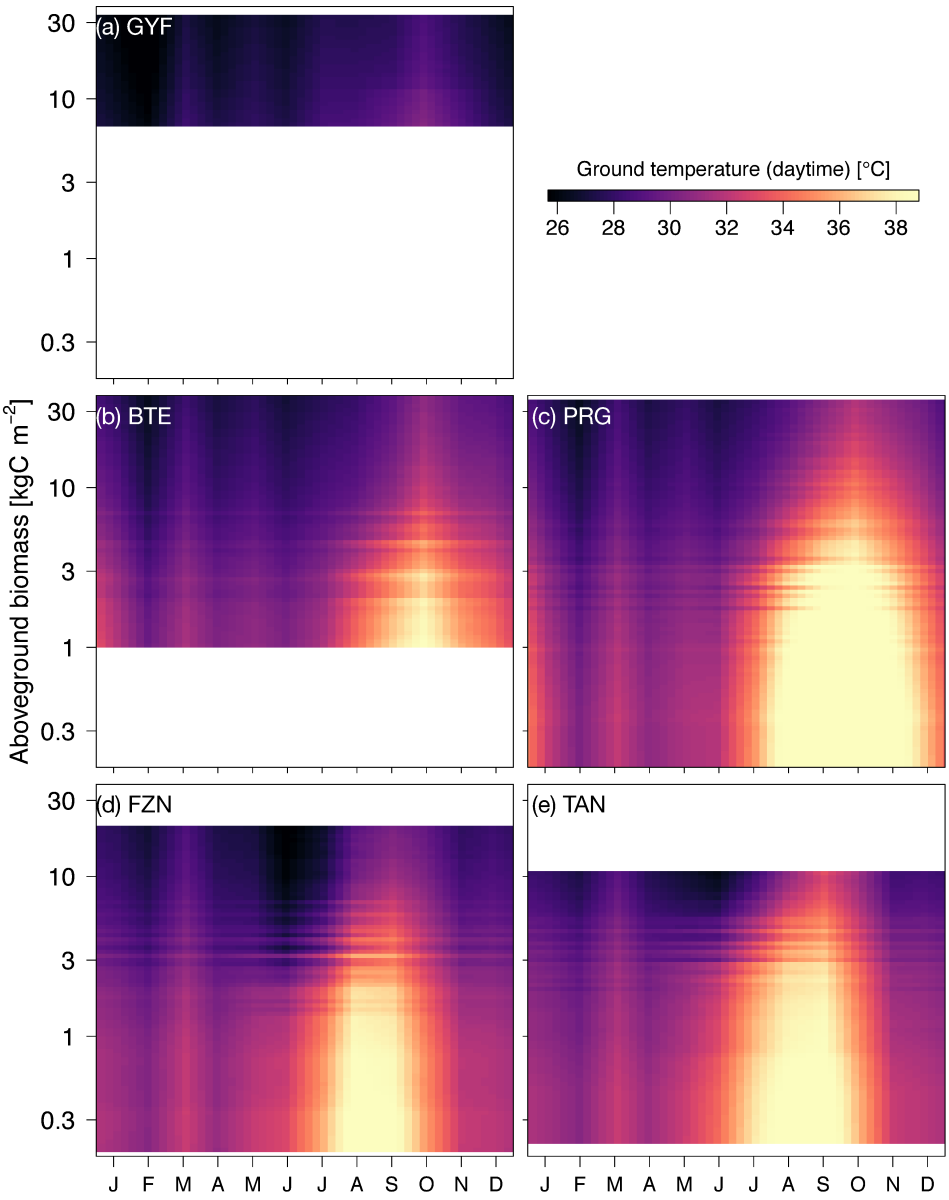

Figure 6. Monthly mean daytime ground temperature as a function of region and local (patch) aboveground biomass. Monthly averages correspond to the 1980–2016 period, simulated by ED-2.2 for (a) Paracou (GYF), (b) Belterra (BTE), (c) Paragominas (PRG), (d) Feliz Natal (FZN), and (e) Tanguro (TAN), and the y axis corresponds to the aboveground biomass for each patch, linearly interpolated for visualization. White areas are outside the range of biomass of each region and thus excluded.

490 larger during typical years than during extreme droughts. For this section, we calculate
491 the monthly water deficit based on the difference between potential evapotranspiration

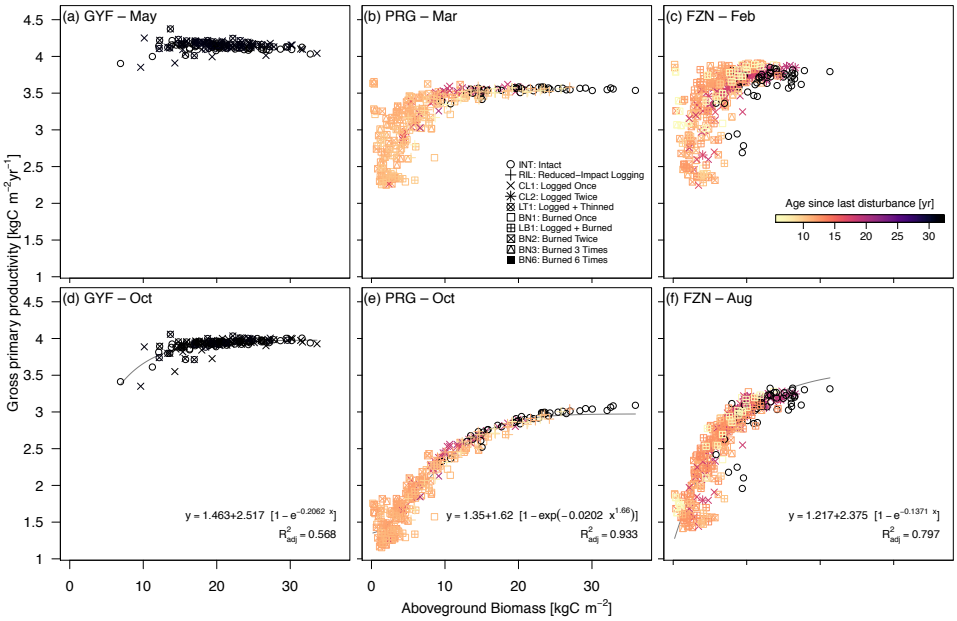

Figure 7. Variability of gross primary productivity (GPP) as a function of local (patch) aboveground biomass (AGB). Scatter plot of AGB (x axis) and GPP (y axis) at sites (a,d) Paracou (GYF), (b,e) Paragominas (PRG), (c,f) Feliz Natal (FZN), for (a-c) the peak of wet season — May (GYF), March (PRG), and February (FZN) — and (d-f) peak of dry season — October (GYF and PRG), and August (FZN). Each point represents the 1980–2016 average GPP of each patch solved by ED-2.2; point shapes correspond to the disturbance history, and point colors represent the time between the last disturbance (undetermined for intact forests) and lidar data acquisition. Curves correspond to non-linear least squares fits of the most parsimonious function, defined from Bayesian Information Criterion (Schwarz, 1978), between shifted exponential or shifted Weibull functions. Only fits that produced $R^2_{adj} > 0.5$ were included.

(calculated following Priestley & Taylor, 1972) and rainfall, and relate the 12-month running averages of multiple response variables with the maximum cumulative water deficit over the previous 12 months, and define drought length as the number of consecutive months in water deficit exceeds 20 mm. Using region PRG as an example, as the region has the broadest range of recent disturbances and maximum cumulative water deficit, we found that, during typical rainfall periods, evapotranspiration in logged forests and burned forests were 3–6% and 11–22% lower than intact forests, respectively (Figure 8a); this difference was significantly reduced or even reversed during severe droughts, when evapotranspiration of degraded forests were up to 4% higher than in intact forests (Figure 8a). De-

graded forests have a lower proportion of shade-tolerant, late-successional trees, and typical stomatal conductance is higher by 19–34% in burned forests and by 5–13% in logged forests (Figure 8b). This result indicates that the reduced typical evapotranspiration results from degraded forests having lower leaf area index relative to intact forests, as local leaf area index is related to local aboveground biomass (Figure S13). In addition, extreme droughts did not substantially reduce the differences in stomatal conductance between degraded and intact forests (Figure 8b). While evapotranspiration was generally lower in degraded forests, total evaporation (from ground and canopy intercepted water) was higher in most degraded forests, with burned forests experiencing 3–26% more evaporation in typical years and 0–14% during severe droughts (Figure 8c). The combination of higher evaporation and relatively shorter canopy (shallower roots) in degraded forests were typically translated into slightly drier near-surface soils (Figure 8d): during typical years, soil water availability at the top 30 cm layers was 1.2–12% lower in burned forests than intact forests, whereas the differences were more modest in logged forests (0.2–3%) and even reversed during extreme droughts (Figure 8d). Carbon and energy fluxes showed similar behavior. Gross primary productivity in intact forests steadily decreased with increased drought severity, and the depletion of productivity caused by degradation is most marked during typical years but is reduced during severe droughts (Figure S14a). While ground temperature is always higher in degraded forests (Figure S14b), differences in sensible heat fluxes and outgoing longwave radiation also diminish during extreme drought conditions (Figure S14c,d).

Degraded forests show drier near-surface soils (Figure 8d) and warmer surface temperatures (Figure S14) than intact forests for most years, yet the interannual variability of climate also modulates the differences in water, carbon, and energy cycles between degraded and intact forests (Figures 8 and S14). Therefore, both degradation and climate may influence the flammability of forests. The average flammable area predicted by ED-2.2 (Section 2.4) shows large variation across regions, ranging from nearly zero at GYF forests (the wettest region) to over $25\%\,\mathrm{yr}^{-1}$ at some of the forests in TAN (the driest region) (Figure 9a). Within each region (i.e. under the same prescribed climate), the model generally predicted higher flammability for the shortest forests (< 10 m), although predictions also indicate large within-region variability of flammable area for forests with intermediate canopy height (10–25 m) (Figure 9a). For most forests, flammable conditions were predicted mostly during moderate or severe droughts, regardless of the degra-

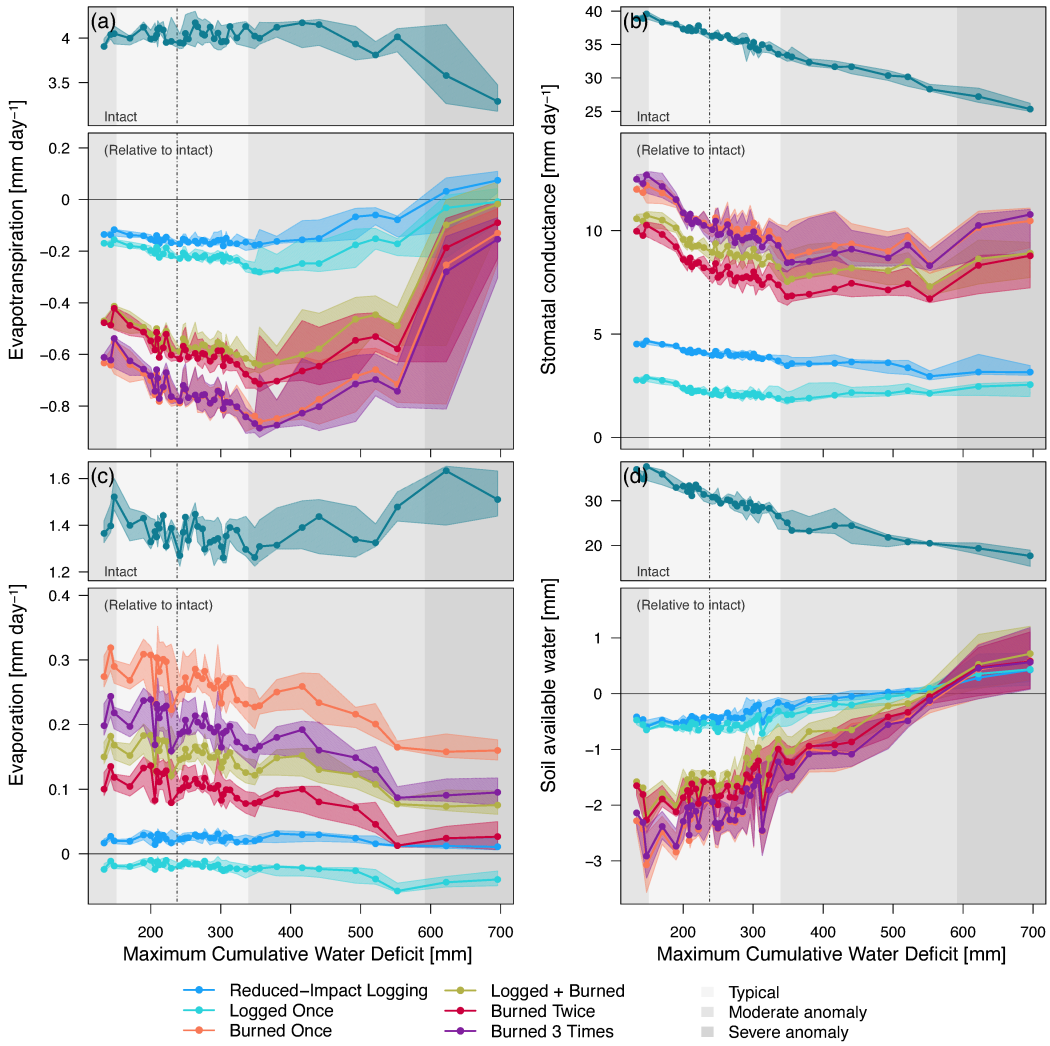

Figure 8. Response of the water cycle components across a forest degradation gradient and drought severity in Paragominas (PRG). Selected components: (a) Total water vapor flux, (b) stomatal conductance, averaged by leaf area, (c) evaporation, and (d) soil available water (i.e. in excess of permanent wilting point) of the top 30 cm. Points correspond to the median value of 12-month running averages, aggregated into 40 quantiles along the range of maximum cumulative water deficit (MCWD). Bands around the points correspond to the 95% range within each MCWD bin. Top panels are the absolute value for intact forests, and bottom panels are the absolute difference between degraded and intact forests. Background shades denote the MCWD anomaly: light gray – 68% range around the median (dot-dash vertical line); intermediate gray – 95% range; dark gray – anomalies exceeding the 95% range.

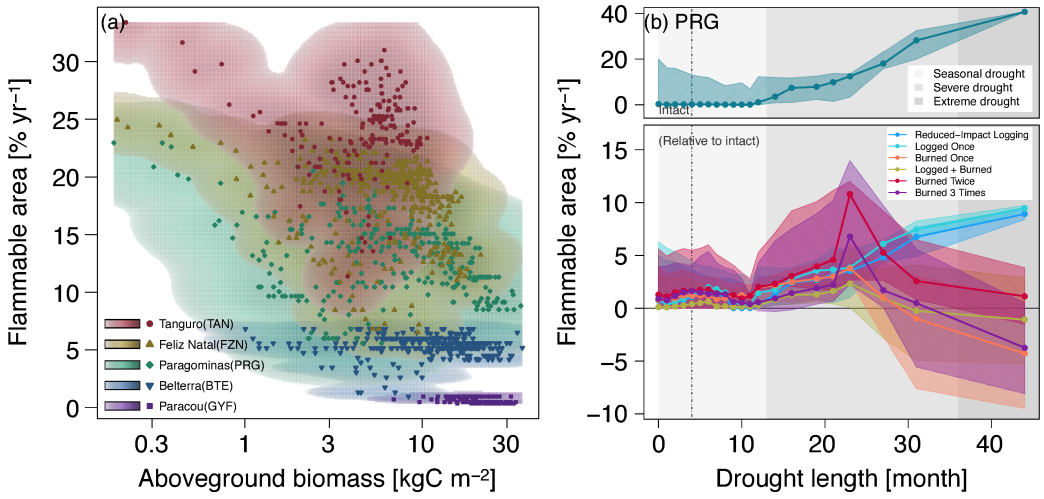

Figure 9. Average flammability as functions of degradation and climate variability. (a) Scatter plot shows the average flammable area (1980–2016) for each simulated patch across all regions, as a function of canopy height. Density cloud (background color) was produced through a bi-dimensional kernel density estimator; points are the averages used to generate each density cloud. Color ramps (logarithmic) range from 0.1 – 100% of the maximum computed scale. (b) Flammable area at region PRG, as a function of degradation history and drought length (number of consecutive months with water deficit in excess of 20 mm). Points correspond to the median value of 12-month running averages, aggregated into quantiles along the drought length. Bands around the points correspond to the 95% range within each drought length bin. Top panels are the absolute value for intact forests, and bottom panels are the absolute difference between degraded and intact forests. Background shades denote drought-length classes used in the text: seasonal (light gray, less than 12 months); severe (intermediate gray, 12–36 months); extreme (dark grey; more than 36 months). Flammability response to degradation and drought duration for other regions are shown in Figure S15.

dation history, as exemplified by region PRG (Figure 9b). While the time series of flammable area were synchronized across degradation types, ED-2.2 predictions of flammable area were generally higher for burned forests than intact or lightly logged forests (Figures 9b and S15). The one exception was the driest region (TAN), where forests that burned multiple times experienced lower flammability than intact forests (Figure S15d); at TAN, even intact forests were relatively short (Figure 9a), which caused ED-2.2 to predict limited access to deeper soils and increased desiccation.

4 Discussion

4.1 Initialization of forest structure from remote sensing

Our method to derive the vertical structure of the canopy from high-resolution airborne lidar successfully characterized the diversity of forest structures of the Amazon, captured differences in forest structure variability along a precipitation gradient, and described the within-region variability in forest structure caused by forest degradation (Figures 3 and S2-S3). Previous studies have used forest structure derived from remote-sensing data to initialize vegetation demography models in tropical forests (e.g., Hurtt et al., 2004; Antonarakis et al., 2011; Rödig et al., 2018). However, these studies often assume a relationship between forest structure and canopy height with stand age. While this assumption has been successfully applied to intact and second-growth tropical forests (Hurtt et al., 2004; Antonarakis et al., 2011), the association between forest structure and succession is unlikely to be preserved in degraded forests. For example, understory fires proportionally kill more smaller trees than large trees (Uhl & Kauffman, 1990; Brando et al., 2012; Silva et al., 2018), and selective logging creates complex mosaics of forest structure, with substantial losses of large trees from harvesting, and extensive damage to smaller trees in skid trails (Feldpausch et al., 2005). In contrast, our approach accounts for the entire vertical profile at local (50-m) scale, similarly to Antonarakis et al. (2014), which does not require any assumption on the successional stage of the forest. Importantly, our approach requires only the vertical distribution of returns, and could be adapted to large-footprint, airborne or spaceborne lidar data, including the NASA's Global Ecosystem Dynamics Investigation (GEDI, Hancock et al., 2019).

We demonstrated that the initialization from airborne lidar profiles captures most of the variability across and within regions, yet it has important assumptions and limitations. First, our approach relies on allometric equations to determine both the diameter at breast height (DBH), and the individual leaf area (L_i, Text S4.3), with the implicit assumption, that the contribution of branches, twigs, and stems to the lidar return signal is negligible. In reality, allometric equations have either large uncertainties (DBH) or limited number of samples (Figure S16). Previous studies using destructive sampling and terrestrial laser scanning suggest that wood area index may constitute 7–15% of the plant area index (Olivas et al., 2013; Schneider et al., 2019). The use of allometric equations that account for regional variation (e.g., Feldpausch et al., 2011, 2012), and the ex-

pansion of open-source databases, such as the Biomass And Allometry Database (BAAD, Falster et al., 2015) used in our study, could further improve the characterization of the vertical structure. In addition, the increased availability of terrestrial laser scanning (TLS) and high-resolution, low-altitude unmanned aerial vehicle lidar could substantially increase the data availability and thus improve the overall quality of allometric equations and constrain the relative contribution of woody tissues to the total plant area (Calders et al., 2015; Stovall et al., 2018; Schneider et al., 2019). Alternatively, techniques that extract individual tree crowns from lidar point clouds readily provide highly accurate local stem density and local size-frequency distributions (e.g., tree height or crown size; Ferraz et al., 2016, 2020). These distributions can be used to attribute DBH to individuals and generate initial conditions akin to forest inventory to the ED-2.2 model, and data-model fusion techniques that leverage the growing availability of data could reduce uncertainties on many model parameters, including allometry (F. J. Fischer et al., 2019). Finally, ED-2.2 overestimated the seasonality of gross primary productivity and evapotranspiration at the driest region (TAN) (Figures S4 and S6). This result suggests that simulated rooting depth for TAN was underestimated in the model. Rooting profiles in tropical forests remain largely uncertain: some site studies have sought to relate individual tree size with rooting depth using isotopic measurements (e.g., Stahl et al., 2013; Brum et al., 2019), whereas regional studies that provide spatial distribution of rooting depth still show important discrepancies in the tropics (e.g., Yang et al., 2016; Fan et al., 2017). Constraining the below-ground allocation of tropical ecosystems should be a priority in future studies.

In our study we inferred the functional diversity from forest structure obtained from existing forest inventory plots. The functional group attribution captured the general characteristics of functional composition along degradation gradients (Figure S1), including the more frequent occurrence of early-successional individuals in degraded forests, consistent with field-based studies (Both et al., 2019); nonetheless, uncertainties in functional attribution from field measurements are high. The increased availability of coordinated airborne laser scanning (ALS) and airborne imaging spectroscopy (AIS) data in mid-latitudes has lead to opportunities to link structural variability with functional diversity (e.g., Antonarakis et al., 2014; Schneider et al., 2017), and previous studies have successfully integrated ALS and AIS data to attribute functional groups in the ED-2 model (e.g., Antonarakis et al., 2014; Bogan et al., 2019). Overlapping ALS and AIS data over

tropical forests are becoming increasingly common (Asner et al., 2014; de Almeida et al., 2019; Laybros et al., 2019) and could provide new opportunities to reduce uncertainties in functional attribution in future studies. Likewise, ongoing and upcoming spaceborne missions at the International Space Station such as GEDI (Hancock et al., 2019), and the Hyperspectral Imaging Suite (HISUI, Matsunaga et al., 2017) will allow for large-scale characterization of structure and function of ecosystems at global scale (Stavros et al., 2017; Schimel et al., 2019).

4.2 Degradation impacts on ecosystem functioning

In addition to carbon losses and structural changes, degradation has substantial impacts on energy and water cycles in Amazonian forests, especially in severely degraded forests with marked dry season. According to the ED-2.2 simulations, ground temperature of logged forests ranged from nearly-identical to intact forests (low-impact logging or old logging disturbances) to 0.7°C warmer (recently logged forests), whereas severely burned forests experienced daytime near-surface temperatures increases of as much as 4°C (Figure S10), and differences between the lowest and highest biomass patches exceeded 9°C (Figure 6). Observed differences in understory temperatures show large variability, but they generally agree with the ED-2.2 results. For example, results of temperature differences between logged and intact areas in the wet forests of Sabah, Malaysia, ranged from negligible to 1.2°C for average maximum temperature (Senior et al., 2018; Jucker et al., 2018). The predicted warmer daytime understory temperatures at recurrently burned forests also yielded drier near-surface conditions: daytime ground vapor pressure deficit was on average 15–25 hPa greater than in intact forests (equivalent to 5–15% reduction in relative humidity), which is within the range observed after the most damaging experimental fire at TAN in 2007 (Brando et al., 2014), and similar to differences in understory relative humidity reported in the dry season between open-canopy seasonally flooded forests and closed-canopy upland forests in the Central Amazon (de Resende et al., 2014). Because temperatures are higher in degraded forests, the simulated changes in energy and water cycle caused by degradation also point to a reduction of entropy production in degraded forests, which is consistent with the results across pastures and intact forests across the Amazon (Holdaway et al., 2010).

ED-2.2 showed various degrees of agreement with the few existing observational studies comparing changes in evapotranspiration due to degradation. Evapotranspira-

tion response to reduced-impact logging was minor (−1.9% reduction relative to intact in BTE), consistent with eddy covariance tower estimates in a logging experiment in the same region (−3.7% reduction after accounting for site differences and interannual variability, S. D. Miller et al., 2011). The model results for the experimental fire at TAN, however, suggested similar wet-season ET between burned and intact forests ($\Delta\mathrm{ET} = \mathrm{ET}_{\mathrm{Brn}} - \mathrm{ET}_{\mathrm{Int}} = 0.002\,\mathrm{mm\,day^{-1}}$), with stronger depletion of ET in burned forests during the dry season ($\Delta\mathrm{ET} = -0.31\,\mathrm{mm\,day^{-1}}$) (Figures 5 and S6). In contrast, Brando, Silvério, et al. (2019) found higher ET in burned forests over a period of 4 years, albeit ΔET also showed significant interannual variability. A few other studies suggest that the significant decline in dry-season ET in burned forests may be expected in some areas: for example, Hirano et al. (2015) found that evapotranspiration of drained and burned peatlands with second-growth vegetation in Central Kalimantan (Indonesia) was $0.43\,\mathrm{mm\,day^{-1}}$ lower than drained forests; Quesada et al. (2004) inferred ET changes from soil water budget in savannas and found significant reductions following fires in a savanna site in Central Brazil. The advent of high-resolution remote sensing products that quantify energy, water, and carbon fluxes, such as the ECOsystem Spaceborne Thermal Radiometer Experiment on Space Station (ECOSTRESS) and the Orbiting Carbon Observatory 3 (OCO-3), will provide new opportunities to quantify the role of tropical forest degradation on ecosystem functioning at regional scale (Schimel et al., 2019), as well as to provide new benchmark data for ecosystem models.

Our model results indicate that severe degradation substantially alters the magnitude and seasonality of energy, water, and carbon fluxes (Figures 5-7 and S10-S12). In our study, we disabled the vegetation dynamics in ED-2.2 to ensure that predicted differences in ecosystem functioning could be unequivocally attributed to structural diversity, but the differences in ecosystem functioning between degraded and intact forests may diminish over time as the forest recovers from previous disturbance. This pathway is consistent with the relatively small differences in ET and surface temperature (Figures 5-6) observed at logged forests at GYF (25 years since last disturbance) and burned forests at BTE (15 years since last disturbance). However, the recovery trajectory is one out of multiple possible pathways: degraded forests may be more prone to subsequent disturbances (Silvério et al., 2019; Hérault & Piponiot, 2018); the recovery dynamics can be long or not attainable if multiple stable states exist or if succession is arrested (Mesquita et al., 2015; Ghazoul & Chazdon, 2017), potentially prolonging the impacts of forest degra-

dation on energy and water cycles; and feedbacks on precipitation caused by degradation could affect the spatial distribution of rainfall similarly to the effect observed with deforestation (Spracklen et al., 2018), although to our knowledge this impact has not yet been quantified for degraded forests.

In this study, we focused on the effects of forest structure on ecosystem function, and thus we used idealized, homogeneous soil with intermediate hydraulic characteristics in all simulations. In reality, soils across the Amazon are highly heterogeneous and directly affect forest structure across the biome (Quesada et al., 2012). Likewise, soil depth and texture and variability in local topography also modulate the effects of tropical forest degradation on microclimate (Jucker et al., 2018). A previous study using ED-2.2 found that evapotranspiration in Central Amazonia could decrease by 12–16% under scenarios of recurrent yearlong droughts (40% reduction in rainfall), but the severity of the decrease varied by 7% under the same climate scenarios but different soil hydraulic properties (Longo et al., 2018). These results suggest that degraded forests in clay-rich, compact soils and deeper water table could amplify reductions in evapotranspiration and gross primary productivity during the dry season, while degradation effects on energy, water, and carbon cycle would likely be dampened in regions where the water table is near the surface for most of the year, or soils with higher water storage capacity.

4.3 Interactions between forest degradation and climate variability

The predicted reductions in evapotranspiration (ET) in the most degraded areas during the dry season suggest that land-use change impacts on the water cycle may be more widespread and pervasive than indicated by earlier studies. Previous model-based studies showed that biome-wide deforestation could cause ET to decrease by 25–40% relative to intact forests in the Amazon during the dry season (e.g., von Randow et al., 2004; Zemp et al., 2017). These reductions are comparable to the ET reductions predicted by ED-2.2 at the most degraded forests (21–32%, Figure 5). Because tropical forest degradation affects an area comparable to deforestation in the Amazon (Tyukavina et al., 2017), it may further reduce the strength of the Amazon water vapor source to the atmosphere. In our study, we focused on understanding how climate and structure variability impacts the water and energy fluxes, but degradation-driven changes in these fluxes are likely to feed back into the atmosphere. For example, changes in evapotranspiration and sensible heat flux associated with deforestation are known to either redistribute or reduce to-

tal rainfall in tropical forests (Spracklen et al., 2018, and references therein), and a substantial fraction of South American precipitation water comes from evapotranspiration from Amazonian forests (van der Ent et al., 2010). Recent estimates of ET for the Amazon Basin from the Gravity Recovery and Climate Experiment (GRACE) suggest that the basin-wide ET (including intact forests) has decreased by 1.7% between 2002 and 2015 (Swann & Koven, 2017). In addition, several studies suggest that the dry season in the Amazon is becoming longer (Fu et al., 2013; Sena et al., 2018), and land use change is one of the main drivers of the drying trend (Barkhordarian et al., 2018). The role of forest degradation on ongoing and future changes in climate across the Amazon remains uncertain and deserves further investigation, potentially with coupled biosphere-atmosphere models that represent heterogeneity in forest structure and functioning (Swann et al., 2015; Knox et al., 2015; Wu et al., 2017). Likewise, we could not account for cascading effects of climate on the energy, water, and carbon cycle in this study because we disabled dynamic vegetation. However, severe droughts are known to increase mortality rates and canopy turnover in tropical forests (Phillips et al., 2010; Feldpausch et al., 2016; Leitold et al., 2018); such disturbances may increase gap fraction and thus reduce gross primary productivity and evapotranspiration in the years immediately following the drought. Future studies that include dynamic vegetation can provide further insights on the resilience and resistance of degraded and intact forests to climate extreme.

Our results show that structural changes resulting from forest degradation make the forest surface drier and warmer (Figures 5-8 and S10). Drier and warmer conditions near the surface increase flammability (Brando, Paolucci, et al., 2019, and references therein), and it has been long suggested that forest degradation and canopy opening make forests more likely to burn (e.g., Uhl & Buschbacher, 1985; Cochrane et al., 1999; Ray et al., 2005; A. A. C. Alencar et al., 2015). The ED-2.2 simulations indeed predicted higher flammability in degraded (more open-canopy) forests on any given year (Figures 9 and S15). However, our results also suggest that climate strongly drives the variability of flammable area across most of our study regions (Figures 9b and S15), which is consistent with the significant increases in forest fires in the Amazon during extreme drought years (Morton et al., 2013; Aragão et al., 2018). Moreover, our results indicate that differences in flammable area between intact and degraded forests are reduced or even reversed during extreme droughts, which indicates that under extreme conditions, the level of degradation is less critical to create flammable conditions. This effect was predicted for most years at TAN,

which typically experiences severe and longer dry seasons compared to the other study regions (Figure S15).

Previous studies suggest that parts of the Eastern Amazon could become drier by the end of the century and experience more extreme events, including droughts (IPCC, 2014; Duffy et al., 2015), and thus potentially more susceptible to future fires (De Faria et al., 2017; Brando et al., 2020). However, how tropical forest flammability will respond in the long-term to ongoing changes in climate and land use is still uncertain, and recent studies have shown that either climate (Le Page et al., 2017) or land use (Fonseca et al., 2019) could be dominant on predicted shifts in fire regime. Importantly, while our analysis focused on flammability, and ED-2.2 fire model captures the general patterns of fire disturbance across the Amazon (Longo, Knox, Levine, et al., 2019), it does not represent many mechanisms and processes that are critical to describe fire dynamics in tropical forests, such as anthropogenic ignitions, diurnal cycle of fire intensity, and fire termination, therefore we could not quantify the effects of fire on further forest degradation. The use of process-based fire disturbance models within the ED-2.2 (e.g., Thonicke et al., 2010; Le Page et al., 2015) framework could contribute to further improve our understanding of interactions between forest degradation, climate, and flammability across the Amazon.

5 Conclusion

Our study showed that tropical forest degradation can markedly modify the ecosystem functioning in the Amazon, with substantial reductions in evapotranspiration (ET) and gross primary productivity (GPP), and increase in surface temperature (Figures 5-8). Within the regions included in our study, the effects of degradation on energy, water, and carbon cycles were the strongest in the Eastern and Southern Amazon, where the dry season is more pronounced. Notably, in areas where severe forest degradation resulted in substantial changes in forest structure, reductions in dry-season evapotranspiration are similar to those found in deforested areas (Figure 5; von Randow et al., 2004). The area of the Amazon forest impacted by degradation is comparable to the deforested area (Asner et al., 2005; Morton et al., 2013; Souza Jr. et al., 2013; Tyukavina et al., 2017), and thus degradation-driven changes in water, energy, and carbon cycles are potentially important. However, the extent to which degradation affects the biophysical and biogeochemical cycles at regional scale ultimately depends on (1) annual degradation rates;

(2) recovery time of degraded forests; and (3) the likelihood that degraded forests are cleared. For example, (Brando, Silvério, et al., 2019) found that ET in burned forests was indistinguishable from intact forests 7 years after the last fire. While their result suggests fast recovery of degraded forests, the impacts of degradation on ET can still be regionally relevant if degradation rates are sufficiently high to maintain low average age since last disturbance in degraded forests. Moreover, we found that the impacts of tropical forest degradation on energy, water, and carbon cycles and on flammability are more pronounced during typical years than during extreme droughts (when all forests become flammable), which highlights the complex interactions between climate and forest structure. To understand and reduce uncertainties of climate-structure interactions, it would be valuable to leverage the recent advances in remote sensing of forest structure, including the recently launched GEDI mission (Hancock et al., 2019), and terrestrial biosphere models that can represent complex and heterogeneous ecosystems (Fisher et al., 2018). Our study, while focusing on airborne lidar data, has demonstrated the opportunities to integrate remote sensing and terrestrial biosphere models even in regions with complex forest structure such as degraded forests.

Acknowledgments

Airborne lidar and forest inventory data were obtained from Sustainable Landscapes Brazil (2019), dos-Santos et al. (2019) (Brazil) and Paracou Portal (2016) (French Guiana). MERRA-2 reanalyses are available from GMAO (2015a, 2015b, 2015c, 2015d) and MSWEP-2.2 data were downloaded from `http://www.gloh2o.org`. The ED-2.2 model used in this study is available at Longo et al. (2019) and the scripts and ED-2.2 output are permanently stored at Longo et al. (2020). Trait data are available at the TRY initiative on plant traits (`http://www.try-db.org`), request 2751; at Gu et al. (2016); or as supporting information from the cited references (I. J. Wright et al., 2004; Santiago & Wright, 2007; Bahar et al., 2017).

The research was carried out at the Jet Propulsion Laboratory, California Institute of Technology, under a contract with the National Aeronautics and Space Administration (80NM0018D004), and supported by NASA Earth Sciences grant (NNH16ZDA001N-IDS, grant 16-IDS16-0049). Data recorded at the Guyaflux tower were obtained thanks to the support of two *Investissement d'avenir* grants from the Agence Nationale de la Recherche (CEBA, ref ANR-10-LABX-25-01; ARBRE, ref. ANR-11-LABX-0002-01). Data

in Brazil were acquired by the Sustainable Landscapes Brazil project supported by the Brazilian Agricultural Research Corporation (EMBRAPA), the U.S. Forest Service, and USAID, and the U.S. Department of State. The study has been supported by the TRY initiative on plant traits, which is hosted, developed and maintained by J. Kattge and G. Bönisch (Max Planck Institute for Biogeochemistry, Jena, Germany). TRY is currently supported by DIVERSITAS/Future Earth and the German Centre for Integrative Biodiversity Research (iDiv) Halle-Jena-Leipzig.

We thank Xiangtao Xu for sharing the trait plasticity algorithm and discussions on model results; Divino Silvério for processing and sharing the data from Tanguro; Hylke Beck for sharing the MSWEP-2.2 data; and Marcos Scaranello, Fabian Schneider, Alexandra Konings, and A. Anthony Bloom for discussions on the lidar initialization algorithm and interpretation of model results. The model simulations were carried out at the Odyssey cluster, supported by the FAS Division of Science, Research Computing Group at Harvard University; and at the Brazilian National Laboratory for Scientific Computing (LNCC). M.L. was supported by the São Paulo State Research Foundation (FAPESP, 2015/07227-6) and by the NASA Postdoctoral Program, administered by Universities Space Research Association under contract with NASA. M.K. was supported in part by the Next Generation Ecosystem Experiments-Tropics, funded by the U.S. Department of Energy, Office of Science, Office of Biological and Environmental Research.

References

Achard, F., Beuchle, R., Mayaux, P., Stibig, H.-J., Bodart, C., Brink, A., ... Simonetti, D. (2014, Aug). Determination of tropical deforestation rates and related carbon losses from 1990 to 2010. *Glob. Change Biol.*, *20*(8), 2540–2554. doi: 10.1111/gcb.12605

Alamgir, M., Campbell, M. J., Turton, S. M., Pert, P. L., Edwards, W., & Laurance, W. F. (2016, Jul). Degraded tropical rain forests possess valuable carbon storage opportunities in a complex, forested landscape. *Sci. Rep.*, *6*(30012). doi: 10.1038/srep30012

Alencar, A., Nepstad, D., & Vera Diaz, M. C. (2006, Feb). Forest understory fire in the Brazilian Amazon in ENSO and non-ENSO years: Area burned and committed carbon emissions. *Earth Interact.*, *10*(6), 1–17. doi: 10.1175/EI150.1

Alencar, A. A. C., Brando, P. M., Asner, G. P., & Putz, F. E. (2015, Sep). Land-

scape fragmentation, severe drought and the new Amazon forest fire regime. *Ecol. Appl.*, *25*(6), 1493–1505. doi: 10.1890/14-1528.1

Antonarakis, A. S., Munger, J. W., & Moorcroft, P. R. (2014, Jul). Imaging spectroscopy- and lidar-derived estimates of canopy composition and structure to improve predictions of forest carbon fluxes and ecosystem dynamics. *Geophys. Res. Lett.*, *41*(7), 2535–2542. doi: 10.1002/2013GL058373

Antonarakis, A. S., Saatchi, S. S., Chazdon, R. L., & Moorcroft, P. R. (2011, Jun). Using lidar and radar measurements to constrain predictions of forest ecosystem structure and function. *Ecol. Appl.*, *21*(4), 1120–1137. doi: 10.1890/10-0274.1

Aragão, L. E. O. C., Anderson, L. O., Fonseca, M. G., Rosan, T. M., Vedovato, L. B., Wagner, F. H., ... Saatchi, S. (2018, Feb). 21st century drought-related fires counteract the decline of Amazon deforestation carbon emissions. *Nature Comm.*, *9*(1), 536. doi: 10.1038/s41467-017-02771-y

Aragão, L. E. O. C., Poulter, B., Barlow, J. B., Anderson, L. O., Malhi, Y., Saatchi, S., ... Gloor, E. (2014, Nov). Environmental change and the carbon balance of Amazonian forests. *Biol. Rev.*, *89*(4), 913–931. doi: 10.1111/brv.12088

Asner, G. P., Broadbent, E. N., Oliveira, P. J. C., Keller, M., Knapp, D. E., & Silva, J. N. M. (2006, Aug). Condition and fate of logged forests in the Brazilian Amazon. *Proc. Natl. Acad. Sci. U. S. A.*, *103*(34), 12947–12950. doi: 10.1073/pnas.0604093103

Asner, G. P., Knapp, D. E., Broadbent, E. N., Oliveira, P. J. C., Keller, M., & Silva, J. N. (2005, Oct). Selective logging in the Brazilian Amazon. *Science*, *310*(5747), 480–482. doi: 10.1126/science.1118051

Asner, G. P., Martin, R. E., Tupayachi, R., Anderson, C. B., Sinca, F., Carranza-Jiménez, L., & Martinez, P. (2014, Apr). Amazonian functional diversity from forest canopy chemical assembly. *Proc. Natl. Acad. Sci. U. S. A.*, *111*(15), 5604–5609. doi: 10.1073/pnas.1401181111

Asner, G. P., Powell, G. V. N., Mascaro, J., Knapp, D. E., Clark, J. K., Jacobson, J., ... Hughes, R. F. (2010, Sep). High-resolution forest carbon stocks and emissions in the Amazon. *Proc. Natl. Acad. Sci. U. S. A.*, *107*(38), 16738-16742. doi: 10.1073/pnas.1004875107

Baccini, A., Walker, W., Carvalho, L., Farina, M., Sulla-Menashe, D., & Houghton,

R. A. (2017, Oct). Tropical forests are a net carbon source based on above-ground measurements of gain and loss. *Science*, *358*(6360), 230–234. doi: 10.1126/science.aam5962

Bahar, N. H. A., Ishida, F. Y., Weerasinghe, L. K., Guerrieri, R., O'Sullivan, O. S., Bloomfield, K. J., ... Atkin, O. K. (2017, May). Leaf-level photosynthetic capacity in lowland Amazonian and high-elevation Andean tropical moist forests of Peru. *New Phytol.*, *214*(3), 1002–1018. doi: 10.1111/nph.14079

Balch, J. K., Nepstad, D. C., Brando, P. M., Curran, L. M., Portela, O., de Carvalho, O., & Lefebvre, P. (2008, Oct). Negative fire feedback in a transitional forest of southeastern Amazonia. *Glob. Change Biol.*, *14*(10), 2276–2287. doi: 10.1111/j.1365-2486.2008.01655.x

Baraloto, C., Paine, C. E. T., Poorter, L., Beauchene, J., Bonal, D., Domenach, A.-M., ... Chave, J. (2010, Nov). Decoupled leaf and stem economics in rain forest trees. *Ecol. Lett.*, *13*(11), 1338–1347. doi: 10.1111/j.1461-0248.2010.01517.x

Barkhordarian, A., von Storch, H., Behrangi, A., Loikith, P. C., Mechoso, C. R., & Detzer, J. (2018, Jun). Simultaneous regional detection of land-use changes and elevated GHG levels: the case of spring precipitation in tropical South America. *Geophys. Res. Lett.*, *45*(12), 6262–6271. doi: 10.1029/2018GL078041

Barlow, J., Lagan, B. O., & Peres, C. A. (2003, 5). Morphological correlates of fire-induced tree mortality in a central Amazonian forest. *J. Trop. Ecol.*, *19*(3), 291–299. doi: 10.1017/S0266467403003328

Barlow, J., Lennox, G. D., Ferreira, J., Berenguer, E., Lees, A. C., Mac Nally, R., ... Gardner, T. A. (2016, Jul). Anthropogenic disturbance in tropical forests can double biodiversity loss from deforestation. *Nature*, *535*, 144–147. doi: 10.1038/nature18326

Beck, H. E., Wood, E. F., Pan, M., Fisher, C. K., Miralles, D. G., van Dijk, A. I., ... Adler, R. F. (2019, Mar). MSWEP V2 global 3-hourly 0.1° precipitation: methodology and quantitative assessment. *Bull. Am. Meteorol. Soc.*, *100*(3), 473–500. doi: 10.1175/BAMS-D-17-0138.1

Berenguer, E., Ferreira, J., Gardner, T. A., Aragão, L. E. O. C., de Camargo, P. B., Cerri, C. E., ... Barlow, J. (2014, Dec). A large-scale field assessment of

carbon stocks in human-modified tropical forests. *Glob. Change Biol.*, *20*(12), 3713–3726. doi: 10.1111/gcb.12627

Blair, J. B., & Hofton, M. A. (1999, Aug). Modeling laser altimeter return waveforms over complex vegetation using high-resolution elevation data. *Geophys. Res. Lett.*, *26*(16), 2509–2512. doi: 10.1029/1999GL010484

Blanc, L., Echard, M., Herault, B., Bonal, D., Marcon, E., Chave, J., & Baraloto, C. (2009, Sep). Dynamics of aboveground carbon stocks in a selectively logged tropical forest. *Ecol. Appl.*, *19*(6), 1397–1404. doi: 10.1890/08-1572.1

Bogan, S. A., Antonarakis, A. S., & Moorcroft, P. R. (2019, Jul). Imaging spectrometry-derived estimates of regional ecosystem composition for the Sierra Nevada, California. *Remote Sens. Environ.*, *228*, 14–30. doi: 10.1016/j.rse.2019.03.031

Bonal, D., Bosc, A., Ponton, S., Goret, J.-Y., Burban, B., Gross, P., ... Granier, A. (2008, Aug). Impact of severe dry season on net ecosystem exchange in the Neotropical rainforest of French Guiana. *Glob. Change Biol.*, *14*(8), 1917–1933. doi: 10.1111/j.1365-2486.2008.01610.x

Both, S., Riutta, T., Paine, C. E. T., Elias, D. M. O., Cruz, R. S., Jain, A., ... Burslem, D. F. R. P. (2019, Feb). Logging and soil nutrients independently explain plant trait expression in tropical forests. *New Phytol.*, *221*(4), 1853–1865. doi: 10.1111/nph.15444

Braghiere, R. K., Quaife, T., Black, E., He, L., & Chen, J. M. (2019, Nov). Underestimation of global photosynthesis in earth system models due to representation of vegetation structure. *Global Biogeochem. Cycles*, *33*(11), 1358–1369. doi: 10.1029/2018GB006135

Brando, P. M., Balch, J. K., Nepstad, D. C., Morton, D. C., Putz, F. E., Coe, M. T., ... Soares-Filho, B. S. (2014, Apr). Abrupt increases in Amazonian tree mortality due to drought–fire interactions. *Proc. Natl. Acad. Sci. U. S. A.*, *111*(17), 6347–6352. doi: 10.1073/pnas.1305499111

Brando, P. M., Nepstad, D. C., Balch, J. K., Bolker, B., Christman, M. C., Coe, M., & Putz, F. E. (2012, Feb). Fire-induced tree mortality in a neotropical forest: the roles of bark traits, tree size, wood density and fire behavior. *Glob. Change Biol.*, *18*(2), 630–641. doi: 10.1111/j.1365-2486.2011.02533.x

Brando, P. M., Paolucci, L., Ummenhofer, C. C., Ordway, E. M., Hartmann, H.,

Cattau, M. E., ... Balch, J. (2019, May). Droughts, wildfires, and forest carbon cycling: A pantropical synthesis. *Annu. Rev. Earth Pl. Sc.*, *47*(1), 555–581. doi: 10.1146/annurev-earth-082517-010235

Brando, P. M., Silvério, D., Maracahipes-Santos, L., Oliveira-Santos, C., Levick, S. R., Coe, M. T., ... Trumbore, S. E. (2019, Sep). Prolonged tropical forest degradation due to compounding disturbances: implications for CO_2 and H_2O fluxes of an experimental forest. *Glob. Change Biol.*, *25*(9), 2855–2868. doi: 10.1111/gcb.14659

Brando, P. M., Soares Filho, B., Rodrigues, L., Assunção, A., Morton, D., Tuchschneider, D., ... Coe, M. T. (2020, Jan). The gathering firestorm in southern Amazonia. *Sci. Adv.*, *6*(2), eaay1632. doi: 10.1126/sciadv.aay1632

Brum, M., Vadeboncoeur, M. A., Ivanov, V., Asbjornsen, H., Saleska, S., Alves, L. F., ... Oliveira, R. S. (2019, Jan). Hydrological niche segregation defines forest structure and drought tolerance strategies in a seasonal Amazon forest. *J. Ecol.*, *107*(1), 318–333. doi: 10.1111/1365-2745.13022

Bustamante, M. M. C., Roitman, I., Aide, T. M., Alencar, A., Anderson, L., Aragão, L., ... Vieira, I. C. (2016, Jan). Towards an integrated monitoring framework to assess the effects of tropical forest degradation and recovery on carbon stocks and biodiversity. *Glob. Change Biol.*, *22*(1), 92–109. doi: 10.1111/gcb.13087

Calders, K., Newnham, G., Burt, A., Murphy, S., Raumonen, P., Herold, M., ... Kaasalainen, M. (2015, Feb). Nondestructive estimates of above-ground biomass using terrestrial laser scanning. *Methods Ecol. Evol.*, *6*(2), 198–208. doi: 10.1111/2041-210X.12301

Chave, J., Condit, R., Aguilar, S., Hernandez, A., Lao, S., & Perez, R. (2004, Mar). Error propagation and scaling for tropical forest biomass estimates. *Philos. Trans. R. Soc. B-Biol. Sci.*, *359*(1443), 409–420. doi: 10.1098/rstb.2003.1425

Chave, J., Coomes, D., Jansen, S., Lewis, S. L., Swenson, N. G., & Zanne, A. E. (2009, Apr). Towards a worldwide wood economics spectrum. *Ecol. Lett.*, *12*(4), 351–366. doi: 10.1111/j.1461-0248.2009.01285.x

Chave, J., Réjou-Méchain, M., Búrquez, A., Chidumayo, E., Colgan, M. S., Delitti, W. B., ... Vieilledent, G. (2014, Oct). Improved allometric models to estimate the aboveground biomass of tropical trees. *Glob. Change Biol.*, *20*(10),

3177–3190. doi: 10.1111/gcb.12629

Cochrane, M. A., Alencar, A., Schulze, M. D., Souza, C. M., Nepstad, D. C., Lefebvre, P., & Davidson, E. A. (1999, Jun). Positive feedbacks in the fire dynamic of closed canopy tropical forests. *Science*, *284*(5421), 1832–1835. doi: 10.1126/science.284.5421.1832

Davidson, E. A., de Araújo, A. C., Artaxo, P., Balch, J. K., Brown, I. F., Bustamante, M. M. C., ... Wofsy, S. C. (2012, Jan). The Amazon basin in transition. *Nature*, *481*(7381), 321–328. doi: 10.1038/nature10717

de Almeida, C. T., Galvão, L. S., Aragão, L. E. d. O. C. e., Ometto, J. P. H. B., Jacon, A. D., Pereira, F. R. d. S., ... Longo, M. (2019, Oct). Combining LiDAR and hyperspectral data for aboveground biomass modeling in the Brazilian Amazon using different regression algorithms. *Remote Sens. Environ.*, *232*, 111323. doi: 10.1016/j.rse.2019.111323

De Faria, B. L., Brando, P. M., Macedo, M. N., Panday, P. K., Soares Filho, B. S., & Coe, M. T. (2017, Sep). Current and future patterns of fire-induced forest degradation in Amazonia. *Environ. Res. Lett.*, *12*(9), 095005. doi: 10.1088/1748-9326/aa69ce

de Resende, A. F., Nelson, B. W., Flores, B. M., & de Almeida, D. R. (2014, Nov). Fire damage in seasonally flooded and upland forests of the Central Amazon. *Biotropica*, *46*(6), 643–646. doi: 10.1111/btp.12153

d'Oliveira, M. V. N., Reutebuch, S. E., McGaughey, R. J., & Andersen, H.-E. (2012, Sep). Estimating forest biomass and identifying low-intensity logging areas using airborne scanning lidar in Antimary State Forest, Acre state, western Brazilian Amazon. *Remote Sens. Environ.*, *124*, 479–491. doi: 10.1016/j.rse.2012.05.014

dos-Santos, M., Keller, M., & Morton, D. (2019, Dec). *LiDAR surveys over selected forest research sites, Brazilian Amazon, 2008–2018.* Retrieved 31 Jan 2020, from `https://daac.ornl.gov/cgi-bin/dsviewer.pl?ds_id=1644` doi: 10.3334/ORNLDAAC/1644

Duffy, P. B., Brando, P., Asner, G. P., & Field, C. B. (2015, Oct). Projections of future meteorological drought and wet periods in the Amazon. *Proc. Natl. Acad. Sci. U. S. A.*, *112*(43), 13172–13177. doi: 10.1073/pnas.1421010112

Erb, K.-H., Fetzel, T., Plutzar, C., Kastner, T., Lauk, C., Mayer, A., ... Haberl, H.

(2016, Sep). Biomass turnover time in terrestrial ecosystems halved by land use. *Nature Geosci.*, *9*(9), 674–678. doi: 10.1038/ngeo2782

Erb, K.-H., Kastner, T., Plutzar, C., Bais, A. L. S., Carvalhais, N., Fetzel, T., ... Luyssaert, S. (2018, Jan). Unexpectedly large impact of forest management and grazing on global vegetation biomass. *Nature*, *553*(7686), 73–76. doi: 10.1038/nature25138

Falster, D. S., Duursma, R. A., Ishihara, M. I., Barneche, D. R., FitzJohn, R. G., Vårhammar, A., ... York, R. A. (2015, May). BAAD: a biomass and allometry database for woody plants. *Ecology*, *96*(5), 1445–1445. doi: 10.1890/14-1889.1

Falster, D. S., FitzJohn, R. G., Brännström, Å., Dieckmann, U., & Westoby, M. (2016, Feb). `plant`: A package for modelling forest trait ecology and evolution. *Methods Ecol. Evol.*, *7*(2), 136–146. doi: 10.1111/2041-210X.12525

Fan, Y., Miguez-Macho, G., Jobbágy, E. G., Jackson, R. B., & Otero-Casal, C. (2017, Oct). Hydrologic regulation of plant rooting depth. *Proc. Natl. Acad. Sci. U. S. A.*, *114*(40), 10572–10577. doi: 10.1073/pnas.1712381114

Feldpausch, T. R., Banin, L., Phillips, O. L., Baker, T. R., Lewis, S. L., Quesada, C. A., ... Lloyd, J. (2011, May). Height-diameter allometry of tropical forest trees. *Biogeosciences*, *8*(5), 1081–1106. doi: 10.5194/bg-8-1081-2011

Feldpausch, T. R., Jirka, S., Passos, C. A. M., Jasper, F., & Riha, S. J. (2005, 11). When big trees fall: Damage and carbon export by reduced impact logging in southern Amazonia. *Forest Ecol. Manag.*, *219*(2–3), 199–215. doi: 10.1016/j.foreco.2005.09.003

Feldpausch, T. R., Lloyd, J., Lewis, S. L., Brienen, R. J. W., Gloor, M., Monteagudo Mendoza, A., ... Phillips, O. L. (2012, Aug). Tree height integrated into pantropical forest biomass estimates. *Biogeosciences*, *9*(8), 3381–3403. doi: 10.5194/bg-9-3381-2012

Feldpausch, T. R., Phillips, O. L., Brienen, R. J. W., Gloor, E., Lloyd, J., Lopez-Gonzalez, G., ... Vos, V. A. (2016, Jul). Amazon forest response to repeated droughts. *Global Biogeochem. Cycles*, *30*(7), 964–982. doi: 10.1002/2015GB005133

Ferraz, A., Saatchi, S., Longo, M., & Clark, D. B. (2020). Tropical tree size demography from airborne lidar. *Ecol. Appl.*. (advance online publication) doi: 10

.1002/eap.2154

Ferraz, A., Saatchi, S., Mallet, C., & Meyer, V. (2016, Sep). Lidar detection of individual tree size in tropical forests. *Remote Sens. Environ.*, *183*, 318–333. doi: 10.1016/j.rse.2016.05.028

Ferraz, A., Saatchi, S., Xu, L., Hagen, S., Chave, J., Yu, Y., ... Ganguly, S. (2018, Sep). Carbon storage potential in degraded forests of Kalimantan, Indonesia. *Environ. Res. Lett.*, *13*(9), 095001. doi: 10.1088/1748-9326/aad782

Fischer, F. J., Maréchaux, I., & Chave, J. (2019). Improving plant allometry by fusing forest models and remote sensing. *New Phytol.*. (advance online publication) doi: 10.1111/nph.15810

Fischer, R., Bohn, F., de Paula, M. D., Dislich, C., Groeneveld, J., Gutiérrez, A. G., ... Huth, A. (2016, Apr). Lessons learned from applying a forest gap model to understand ecosystem and carbon dynamics of complex tropical forests. *Ecol. Model.*, *326*, 124–133. doi: 10.1016/j.ecolmodel.2015.11.018

Fisher, R. A., Koven, C. D., Anderegg, W. R. L., Christoffersen, B. O., Dietze, M. C., Farrior, C., ... Moorcroft, P. (2018, Jan). Vegetation demographics in Earth system models: a review of progress and priorities. *Glob. Change Biol.*, *24*(1), 35–54. doi: 10.1111/gcb.13910

Fonseca, M. G., Alves, L. M., Aguiar, A. P. D., Arai, E., Anderson, L. O., Rosan, T. M., ... de Aragão, L. E. O. e. C. (2019). Effects of climate and land-use change scenarios on fire probability during the 21st century in the Brazilian Amazon. *Glob. Change Biol.*. doi: 10.1111/gcb.14709

Friedlingstein, P., Jones, M. W., O'Sullivan, M., Andrew, R. M., Hauck, J., Peters, G. P., ... Zaehle, S. (2019, Dec). Global carbon budget 2019. *Earth Syst. Sci. Data*, *11*(4), 1783–1838. doi: 10.5194/essd-11-1783-2019

Fu, R., Yin, L., Li, W., Arias, P. A., Dickinson, R. E., Huang, L., ... Myneni, R. B. (2013, Nov). Increased dry-season length over southern Amazonia in recent decades and its implication for future climate projection. *Proc. Natl. Acad. Sci. U. S. A.*, *110*(45), 18110-18115. doi: 10.1073/pnas.1302584110

Gelaro, R., McCarty, W., Suárez, M. J., Todling, R., Molod, A., Takacs, L., ... Zhao, B. (2017, Jul). The Modern-Era Retrospective analysis for Research and Applications, version 2 (MERRA-2). *J. Climate*, *30*(14), 5419–5454. doi: 10.1175/JCLI-D-16-0758.1

Ghazoul, J., & Chazdon, R. (2017, Oct). Degradation and recovery in changing forest landscapes: A multiscale conceptual framework. *Ann. Rev. Environ. Res.*, *42*(1), 161–188. doi: 10.1146/annurev-environ-102016-060736

GMAO. (2015a). *MERRA-2 tavg1_2d_flx_Nx: 2d, 1-hourly, time-averaged, single-level, assimilation, surface flux diagnostics V5.12.4.* Retrieved 06 Sep 2018, from `https://doi.org/10.5067/7MCPBJ41Y0K6` doi: 10.5067/7MCPBJ41Y0K6

GMAO. (2015b). *MERRA-2 tavg1_2d_lnd_Nx: 2d, 1-hourly, time-averaged, single-level, assimilation, land surface diagnostics V5.12.4.* Retrieved 06 Sep 2018, from `https://doi.org/10.5067/RKPHT8KC1Y1T` doi: 10.5067/RKPHT8KC1Y1T

GMAO. (2015c). *MERRA-2 tavg1_2d_rad_Nx: 2d, 1-hourly, time-averaged, single-level, assimilation, radiation diagnostics V5.12.4.* Retrieved 06 Sep 2018, from `https://doi.org/10.5067/Q9QMY5PBNV1T` doi: 10.5067/Q9QMY5PBNV1T

GMAO. (2015d). *MERRA-2 tavg1_2d_slv_Nx: 2d, 1-hourly, time-averaged, single-level, assimilation, single-level diagnostics V5.12.4.* Retrieved 06 Sep 2018, from `https://doi.org/10.5067/VJAFPLI1CSIV` doi: 10.5067/VJAFPLI1CSIV

Gourlet-Fleury, S., Ferry, B., Molino, J.-F., Petronelli, P., & Schmitt, L. (2004). Experimental plots: Key features. In S. Gourlet-Fleury, J.-M. Guehl, & O. Laroussinie (Eds.), *Ecology and management of a Neotropical rainforest: Lessons drawn from Paracou, a long-term experimental research site in French Guiana* (pp. 3–60). Paris: Elsevier.

Gourlet-Fleury, S., Guehl, J.-M., & Laroussinie, O. (2004). *Ecology and management of a Neotropical rainforest: Lessons drawn from Paracou, a long-term experimental research site in French Guiana*. Paris: Elsevier.

Grace, J., Mitchard, E., & Gloor, E. (2014, Oct). Perturbations in the carbon budget of the tropics. *Glob. Change Biol.*, *20*(10), 3238–3255. doi: 10.1111/gcb.12600

Grossiord, C., Buckley, T. N., Cernusak, L. A., Novick, K. A., Poulter, B., Siegwolf, R. T. W., ... McDowell, N. G. (2020, Jun). Plant responses to rising vapor pressure deficit. *New Phytol.*, *226*(6), 1550–1566. doi: 10.1111/nph.16485

Gu, L., Norby, R., Haworth, I., Jensen, A., Turner, B., Walker, A., ... Winter, K.

(2016). *Photosynthetic parameters and nutrient content of trees at the Panama crane sites. 1.0. NGEE Tropics data collection.* Retrieved 12 Sep 2019, from `https://ngt-data.lbl.gov` doi: 10.15486/NGT/1255260

Haddad, N. M., Brudvig, L. A., Clobert, J., Davies, K. F., Gonzalez, A., Holt, R. D., ... Townshend, J. R. (2015, Mar). Habitat fragmentation and its lasting impact on Earth's ecosystems. *Science Advances*, *1*(2), e1500052. doi: 10.1126/sciadv.1500052

Hancock, S., Armston, J., Hofton, M., Sun, X., Tang, H., Duncanson, L. I., ... Dubayah, R. (2019, Feb). The GEDI simulator: A large-footprint waveform lidar simulator for calibration and validation of spaceborne missions. *Earth Space Sci.*, *6*(2), 290–310. doi: 10.1029/2018EA000506

Hansen, M. C., Potapov, P. V., Moore, R., Hancher, M., Turubanova, S. A., Tyukavina, A., ... Townshend, J. R. G. (2013, Nov). High-resolution global maps of 21st-century forest cover change. *Science*, *342*(6160), 850–853. doi: 10.1126/science.1244693

Harris, N. L., Brown, S., Hagen, S. C., Saatchi, S. S., Petrova, S., Salas, W., ... Lotsch, A. (2012, Jun). Baseline map of carbon emissions from deforestation in tropical regions. *Science*, *336*(6088), 1573–1576. doi: 10.1126/science.1217962

Hayek, M. N., Longo, M., Wu, J., Smith, M. N., Restrepo-Coupe, N., Tapajós, R., ... Wofsy, S. C. (2018, Aug). Carbon exchange in an Amazon forest: from hours to years. *Biogeosciences*, *15*(15), 4833–4848. doi: 10.5194/bg-15-4833-2018

Hérault, B., & Piponiot, C. (2018, Feb). Key drivers of ecosystem recovery after disturbance in a neotropical forest. *Forest Ecosyst.*, *5*(1), 2. doi: 10.1186/s40663-017-0126-7

Hess, L. L., Melack, J. M., Affonso, A. G., Barbosa, C., Gastil-Buhl, M., & Novo, E. M. L. M. (2015, Aug). Wetlands of the lowland Amazon Basin: Extent, vegetative cover, and dual-season inundated area as mapped with JERS-1 synthetic aperture radar. *Wetlands*, *35*(4), 745–756. doi: 10.1007/s13157-015-0666-y

Hirano, T., Kusin, K., Limin, S., & Osaki, M. (2015, May). Evapotranspiration of tropical peat swamp forests. *Glob. Change Biol.*, *21*(5), 1914–1927. doi: 10.1111/gcb.12653

Holdaway, R. J., Sparrow, A. D., & Coomes, D. A. (2010, May). Trends in entropy production during ecosystem development in the Amazon Basin. *Philos. Trans. R. Soc. B-Biol. Sci.*, *365*(1545), 1437–1447. doi: 10.1098/rstb.2009.0298

Hosonuma, N., Herold, M., De Sy, V., De Fries, R. S., Brockhaus, M., Verchot, L., ... Romijn, E. (2012, Apr). An assessment of deforestation and forest degradation drivers in developing countries. *Environ. Res. Lett.*, *7*(4), 044009. doi: 10.1088/1748-9326/7/4/044009

Huang, M., & Asner, G. P. (2010, Sep). Long-term carbon loss and recovery following selective logging in Amazon forests. *Global Biogeochem. Cycles*, *24*(3), GB3028. doi: 10.1029/2009GB003727

Huang, M., Asner, G. P., Keller, M., & Berry, J. A. (2008, Mar). An ecosystem model for tropical forest disturbance and selective logging. *J. Geophys. Res.-Biogeosci.*, *113*(G1), G01002. doi: 10.1029/2007JG000438

Hunter, M. O., Keller, M., Vitoria, D., & Morton, D. C. (2013, Dec). Tree height and tropical forest biomass estimation. *Biogeosciences*, *10*(6), 10491–10529. doi: 10.5194/bg-10-8385-2013

Hurtt, G. C., Dubayah, R., Drake, J., Moorcroft, P. R., Pacala, S. W., Blair, J. B., & Fearon, M. G. (2004, Jun). Beyond potential vegetation: combining lidar data and a height-structured model for carbon studies. *Ecol. Appl.*, *14*(3), 873–883. doi: 10.1890/02-5317

INMET. (2019, May). *Normais climatológicas do Brasil: 1981-2010.* Retrieved 15 May 2019, from `http://www.inmet.gov.br/portal/index.php?r=clima/normaisClimatologicas` (In Portuguese)

IPCC. (2014). *Climate change 2014: impacts, adaptation, and vulnerability. part b: regional aspects. contribution of working group ii to the fifth assessment report of the Intergovernmental Panel on Climate Change* (V. R. Barros et al., Eds.). Cambridge, UK and New York, NY, USA: Cambridge Univ. Press.

Jucker, T., Caspersen, J., Chave, J., Antin, C., Barbier, N., Bongers, F., ... Coomes, D. A. (2017, Jan). Allometric equations for integrating remote sensing imagery into forest monitoring programmes. *Glob. Change Biol.*, *23*(1), 177–190. doi: 10.1111/gcb.13388

Jucker, T., Hardwick, S. R., Both, S., Elias, D. M., Ewers, R. M., Milodowski, D. T., ... Coomes, D. A. (2018, Nov). Canopy structure and topography jointly con-

strain the microclimate of human-modified tropical landscapes. *Glob. Change Biol.*, *24*(11), 5243–5258. doi: 10.1111/gcb.14415

Kapos, V. (1989, May). Effects of isolation on the water status of forest patches in the brazilian amazon. *J. Trop. Ecol.*, *5*(2), 173–185. doi: 10.1017/S0266467400003448

Kattge, J., Bönisch, G., Díaz, S., Lavorel, S., Prentice, I. C., Leadley, P., ... Wirth, C. (2020, Jan). TRY plant trait database — enhanced coverage and open access. *Glob. Change Biol.*, *26*(1), 119–188. doi: 10.1111/gcb.14904

Kattge, J., Díaz, S., Lavorel, S., Prentice, I. C., Leadley, P., Bönisch, G., ... Wirth, C. (2011, Sep). TRY – a global database of plant traits. *Glob. Change Biol.*, *17*(9), 2905–2935. doi: 10.1111/j.1365-2486.2011.02451.x

Kattge, J., Knorr, W., Raddatz, T., & Wirth, C. (2009, Apr). Quantifying photosynthetic capacity and its relationship to leaf nitrogen content for global-scale terrestrial biosphere models. *Glob. Change Biol.*, *15*(4), 976–991. doi: 10.1111/j.1365-2486.2008.01744.x

Keenan, T. F., & Niinemets, Ülo. (2016, Dec). Global leaf trait estimates biased due to plasticity in the shade. *Nat. Plants*, *3*, 16201. doi: 10.1038/nplants.2016.201

Knox, R. G., Longo, M., Swann, A. L. S., Zhang, K., Levine, N. M., Moorcroft, P. R., & Bras, R. L. (2015, Jan). Hydrometeorological effects of historical land-conversion in an ecosystem-atmosphere model of Northern South America. *Hydrol. Earth Syst. Sci.*, *19*(1), 241–273. doi: 10.5194/hess-19-241-2015

Koven, C. D., Knox, R. G., Fisher, R. A., Chambers, J., Christoffersen, B. O., Davies, S. J., ... Xu, C. (2019). Benchmarking and parameter sensitivity of physiological and vegetation dynamics using the functionally assembled terrestrial ecosystem simulator (FATES) at Barro Colorado Island, Panama. *Biogeosciences Discuss.*, *2019*, 1–46. (in press) doi: 10.5194/bg-2019-409

Laybros, A., Schläpfer, D., Féret, J.-B., Descroix, L., Bedeau, C., Lefevre, M.-J., & Vincent, G. (2019, Apr). Across date species detection using airborne imaging spectroscopy. *Remote Sens.*, *11*(7), 789. doi: 10.3390/rs11070789

Lees, J. M. (2017). RSEIS: Seismic time series analysis tools [Computer software manual]. Retrieved from `https://CRAN.R-project.org/package=RSEIS` (R package version 3.7-4)

Lei, Y., Treuhaft, R., Keller, M., dos-Santos, M., Gonçalves, F., & Neumann, M. (2018, Jun). Quantification of selective logging in tropical forest with spaceborne SAR interferometry. *Remote Sens. Environ.*, *211*, 167–183. doi: 10.1016/j.rse.2018.04.009

Leitold, V., Keller, M., Morton, D., Cook, B., & Shimabukuro, Y. (2015, Feb). Airborne lidar-based estimates of tropical forest structure in complex terrain: opportunities and trade-offs for REDD+. *Carbon Balance Manage.*, *10*(1), 3. doi: 10.1186/s13021-015-0013-x

Leitold, V., Morton, D. C., Longo, M., dos-Santos, M. N., Keller, M., & Scaranello, M. (2018, Aug). El Niño drought increased canopy turnover in Amazon forests. *New Phytol.*, *219*(3), 959–971. doi: 10.1111/nph.15110

Le Page, Y., Morton, D., Bond-Lamberty, B., Pereira, J. M. C., & Hurtt, G. (2015, Feb). HESFIRE: a global fire model to explore the role of anthropogenic and weather drivers. *Biogeosciences*, *12*(3), 887–903. doi: 10.5194/bg-12-887-2015

Le Page, Y., Morton, D., Hartin, C., Bond-Lamberty, B., Pereira, J. M. C., Hurtt, G., & Asrar, G. (2017, Dec). Synergy between land use and climate change increases future fire risk in Amazon forests. *Earth Syst. Dynam.*, *8*(4), 1237–1246. doi: 10.5194/esd-8-1237-2017

Levine, N. M., Zhang, K., Longo, M., Baccini, A., Phillips, O. L., Lewis, S. L., ... Moorcroft, P. R. (2016, Jan). Ecosystem heterogeneity determines the resilience of the Amazon to climate change. *Proc. Natl. Acad. Sci. U. S. A.*, *113*(3), 793–797. doi: 10.1073/pnas.1511344112

Lewis, S. L., Edwards, D. P., & Galbraith, D. (2015, Aug). Increasing human dominance of tropical forests. *Science*, *349*(6250), 827–832. doi: 10.1126/science.aaa9932

Lloyd, J., Patiño, S., Paiva, R. Q., Nardoto, G. B., Quesada, C. A., Santos, A. J. B., ... Mercado, L. M. (2010, Jun). Optimisation of photosynthetic carbon gain and within-canopy gradients of associated foliar traits for Amazon forest trees. *Biogeosciences*, *7*(6), 1833–1859. doi: 10.5194/bg-7-1833-2010

Lombardozzi, D. L., Smith, N. G., Cheng, S. J., Dukes, J. S., Sharkey, T. D., Rogers, A., ... Bonan, G. B. (2018, Jul). Triose phosphate limitation in photosynthesis models reduces leaf photosynthesis and global terrestrial carbon storage. *Environ. Res. Lett.*, *13*(7), 074025. doi: 10.1088/1748-9326/aacf68

Longo, M., Keller, M., dos-Santos, M. N., Morton, D., Moorcroft, P. R., Vincent, G., ... Saatchi, S. (2020, Feb). Supporting dataset for "Impacts of degradation on water, energy, and carbon cycling of the Amazon tropical forests". *Zenodo*. doi: 10.5281/zenodo.3634131

Longo, M., Keller, M., dos Santos, M. N., Leitold, V., Pinagé, E. R., Baccini, A., ... Morton, D. C. (2016, Nov). Aboveground biomass variability across intact and degraded forests in the Brazilian Amazon. *Global Biogeochem. Cycles*, *30*(11), 1639–1660. doi: 10.1002/2016GB005465

Longo, M., Knox, R., Medvigy, D. M., Levine, N. M., Dietze, M., Swann, A. L. S., ... Moorcroft, P. (2019, Aug). Ecosystem Demography model, version 2.2 (ed-2.2). *Zenodo*. doi: 10.5281/zenodo.3365659

Longo, M., Knox, R. G., Levine, N. M., Alves, L. F., Bonal, D., Camargo, P. B., ... Moorcroft, P. R. (2018, Aug). Ecosystem heterogeneity and diversity mitigate Amazon forest resilience to frequent extreme droughts. *New Phytol.*, *219*(3), 914–931. doi: 10.1111/nph.15185

Longo, M., Knox, R. G., Levine, N. M., Swann, A. L. S., Medvigy, D. M., Dietze, M. C., ... Moorcroft, P. R. (2019, Oct). The biophysics, ecology, and biogeochemistry of functionally diverse, vertically and horizontally heterogeneous ecosystems: the Ecosystem Demography model, version 2.2 – part 2: Model evaluation for tropical South America. *Geosci. Model Dev.*, *12*(10), 4347–4374. doi: 10.5194/gmd-12-4347-2019

Longo, M., Knox, R. G., Medvigy, D. M., Levine, N. M., Dietze, M. C., Kim, Y., ... Moorcroft, P. R. (2019, Oct). The biophysics, ecology, and biogeochemistry of functionally diverse, vertically and horizontally heterogeneous ecosystems: the Ecosystem Demography model, version 2.2 – part 1: Model description. *Geosci. Model Dev.*, *12*(10), 4309–4346. doi: 10.5194/gmd-12-4309-2019

MacArthur, R. H., & Horn, H. S. (1969, Sep). Foliage profile by vertical measurements. *Ecology*, *50*(5), 802–804. doi: 10.2307/1933693

Maréchaux, I., & Chave, J. (2017, Nov). An individual-based forest model to jointly simulate carbon and tree diversity in Amazonia: description and applications. *Ecol. Monogr.*, *87*(4), 632–664. doi: 10.1002/ecm.1271

Martins, F. S. R. V., Xaud, H. A. M., dos Santos, J. R., & Galvão, L. S. (2012, Nov). Effects of fire on above-ground forest biomass in the northern Brazilian

Amazon. *J. Trop. Ecol.*, *28*(6), 591–601. doi: 10.1017/S0266467412000636

Marvin, D. C., Asner, G. P., Knapp, D. E., Anderson, C. B., Martin, R. E., Sinca, F., & Tupayachi, R. (2014, Dec). Amazonian landscapes and the bias in field studies of forest structure and biomass. *Proc. Natl. Acad. Sci. U. S. A.*, *111*(48), E5224-E5232. doi: 10.1073/pnas.1412999111

Mascaro, J., Litton, C. M., Hughes, R. F., Uowolo, A., & Schnitzer, S. A. (2011, Nov). Minimizing bias in biomass allometry: Model selection and log-transformation of data. *Biotropica*, *43*(6), 649–653. doi: 10.1111/j.1744-7429.2011.00798.x

Matsunaga, T., Iwasaki, A., Tsuchida, S., Iwao, K., Tanii, J., Kashimura, O., ... Tachikawa, T. (2017, Jul). Current status of hyperspectral imager suite (HISUI) onboard international space station (ISS). In *2017 IEEE international geoscience and remote sensing symposium (IGARSS)* (pp. 443–446). doi: 10.1109/IGARSS.2017.8126989

Mauya, E., Hansen, E., Gobakken, T., Bollandsas, O., Malimbwi, R., & Næsset, E. (2015, May). Effects of field plot size on prediction accuracy of aboveground biomass in airborne laser scanning-assisted inventories in tropical rain forests of Tanzania. *Carbon Balance Manage.*, *10*(1), 10. doi: 10.1186/s13021-015-0021-x

Medvigy, D. M., Wofsy, S. C., Munger, J. W., Hollinger, D. Y., & Moorcroft, P. R. (2009, Jan). Mechanistic scaling of ecosystem function and dynamics in space and time: Ecosystem demography model version 2. *J. Geophys. Res.-Biogeosci.*, *114*(G1), G01002. doi: 10.1029/2008JG000812

Meister, K., Ashton, M. S., Craven, D., & Griscom, H. (2012). Carbon dynamics of tropical forests. In M. S. Ashton, M. L. Tyrrell, D. Spalding, & B. Gentry (Eds.), (pp. 51–75). Dordrecht, Netherlands: Springer Netherlands. doi: 10.1007/978-94-007-2232-3_4

Mesquita, R. d. C. G., Massoca, P. E. d. S., Jakovac, C. C., Bentos, T. V., & Williamson, G. B. (2015, Aug). Amazon rain forest succession: Stochasticity or land-use legacy? *BioScience*, *65*(9), 849–861. doi: 10.1093/biosci/biv108

Meyer, V., Saatchi, S., Ferraz, A., Xu, L., Duque, A., García, M., & Chave, J. (2019, Mar). Forest degradation and biomass loss along the Chocó region of Colombia. *Carbon Balance Manage.*, *14*(1), 2. doi: 10.1186/s13021-019-0117-9

Meyer, V., Saatchi, S. S., Chave, J., Dalling, J. W., Bohlman, S., Fricker, G. A., ... Hubbell, S. (2013, Aug). Detecting tropical forest biomass dynamics from repeated airborne lidar measurements. *Biogeosciences*, *10*(8), 5421–5438. doi: 10.5194/bg-10-5421-2013

Miller, A. J. (1984, Nov). Selection of subsets of regression variables. *J. R. Stat. Soc. A-Gen.*, *147*(3), 389–425. doi: 10.2307/2981576

Miller, S. D., Goulden, M. L., Hutyra, L. R., Keller, M., Saleska, S. R., Wofsy, S. C., ... de Camargo, P. B. (2011, Nov). Reduced impact logging minimally alters tropical rainforest carbon and energy exchange. *Proc. Natl. Acad. Sci. U. S. A.*, *108*(48), 19431–19435. doi: 10.1073/pnas.1105068108

Moorcroft, P. R., Hurtt, G. C., & Pacala, S. W. (2001, Nov). A method for scaling vegetation dynamics: The Ecosystem Demography model (ED). *Ecol. Monogr.*, *71*(4), 557–586. doi: 10.1890/0012-9615(2001)071{$[$}0557:AMFSVD{$]$}2.0.CO;2

Morton, D. C. (2016, Apr). Forest carbon fluxes: A satellite perspective. *Nature Clim. Change*, *6*(4), 346–348. doi: 10.1038/nclimate2978

Morton, D. C., Le Page, Y., DeFries, R. S., Collatz, G. J., & Hurtt, G. C. (2013, Jun). Understorey fire frequency and the fate of burned forests in southern Amazonia. *Philos. Trans. R. Soc. B-Biol. Sci.*, *368*(1619), 20120163. doi: 10.1098/rstb.2012.0163

Ni-Meister, W., Jupp, D., & Dubayah, R. (2001, Sep). Modeling lidar waveforms in heterogeneous and discrete canopies. *IEEE T. Geosci. Remote Sens.*, *39*(9), 1943–1958. doi: 10.1109/36.951085

Norby, R. J., Gu, L., Haworth, I. C., Jensen, A. M., Turner, B. L., Walker, A. P., ... Winter, K. (2017, Sep). Informing models through empirical relationships between foliar phosphorus, nitrogen and photosynthesis across diverse woody species in tropical forests of Panama. *New Phytol.*, *215*(4), 1425–1437. doi: 10.1111/nph.14319

Oleson, K. W., Lawrence, D. M., Bonan, G. B., Drewniak, B., Huang, M., Koven, C. D., ... Yang, Z.-L. (2013). *Technical description of version 4.5 of the community land model (CLM)* (Technical Report Nos. NCAR/TN-503+STR). Boulder, CO: NCAR. (420pp.) doi: 10.5065/D6RR1W7M

Olivas, P. C., Oberbauer, S. F., Clark, D. B., Clark, D. A., Ryan, M. G., O'Brien,

J. J., & Ordoñez, H. (2013, Aug). Comparison of direct and indirect methods for assessing leaf area index across a tropical rain forest landscape. *Agric. For. Meteorol.*, *177*, 110–116. doi: 10.1016/j.agrformet.2013.04.010

Olson, D. M., Dinerstein, E., Wikramanayake, E. D., Burgess, N. D., Powell, G. V. N., Underwood, E. C., ... Kassem, K. R. (2001, Nov). Terrestrial ecoregions of the world: A new map of life on Earth. *BioScience*, *51*(11), 933–938. doi: 10.1641/0006-3568(2001)051[0933:TEOTWA]2.0.CO;2

Paracou Portal. (2016, Dec). *Paracou research station, a large-scale forest disturbance experiment in Amazonia.* Retrieved 31 Jan 2020, from `https://paracou.cirad.fr`

Pearson, T. R. H., Brown, S., Murray, L., & Sidman, G. (2017, Feb). Greenhouse gas emissions from tropical forest degradation: an underestimated source. *Carbon Balance Manage.*, *12*(1), 3. doi: 10.1186/s13021-017-0072-2

Pellegrini, A. F. A., Franco, A. C., & Hoffmann, W. A. (2016, Mar). Shifts in functional traits elevate risk of fire-driven tree dieback in tropical savanna and forest biomes. *Glob. Change Biol.*, *22*(3), 1235–1243. doi: 10.1111/gcb.13110

Phillips, O. L., van der Heijden, G., Lewis, S. L., López-González, G., Aragão, L. E. O. C., Lloyd, J., ... Vilanova, E. (2010, Aug). Drought-mortality relationships for tropical forests. *New Phytol.*, *187*(3), 631-646. doi: 10.1111/j.1469-8137.2010.03359.x

Pinagé, E. R., Keller, M., Duffy, P., Longo, M., dos Santos, M. N., & Morton, D. C. (2019, Mar). Long-term impacts of selective logging on Amazon forest dynamics from multi-temporal airborne LiDAR. *Remote Sens.*, *11*(6), 709. doi: 10.3390/rs11060709

Pinto, A., Amaral, P., Souza Jr., C. M., Veríssimo, A., Salomão, R., Gomes, G., & Balieiro, C. (2009). *Diagnóstico socioeconômico e florestal do município de Paragominas* (Technical Report). Belém, PA, Brazil: Instituto do Homem e Meio Ambiente da Amazônia (Imazon). (Available at `http://imazon.org.br/publicacoes/diagnostico-socioeconomico-e-florestal-do-municipio-de-paragominas/`)

Popescu, S. C., Zhao, K., Neuenschwander, A., & Lin, C. (2011, Nov). Satellite lidar vs. small footprint airborne lidar: Comparing the accuracy of aboveground

biomass estimates and forest structure metrics at footprint level. *Remote Sens. Environ.*, *115*(11), 2786–2797. doi: 10.1016/j.rse.2011.01.026

Potapov, P., Hansen, M. C., Laestadius, L., Turubanova, S., Yaroshenko, A., Thies, C., ... Esipova, E. (2017, Jan). The last frontiers of wilderness: Tracking loss of intact forest landscapes from 2000 to 2013. *Sci. Adv.*, *3*(1), e1600821. doi: 10.1126/sciadv.1600821

Powell, T. L., Galbraith, D. R., Christoffersen, B. O., Harper, A., Imbuzeiro, H. M. A., Rowland, L., ... Moorcroft, P. R. (2013, Oct). Confronting model predictions of carbon fluxes with measurements of Amazon forests subjected to experimental drought. *New Phytol.*, *200*(2), 350–365. doi: 10.1111/nph.12390

Powers, J. S., & Tiffin, P. (2010, Aug). Plant functional type classifications in tropical dry forests in Costa Rica: leaf habit versus taxonomic approaches. *Funct. Ecol.*, *24*(4), 927–936. doi: 10.1111/j.1365-2435.2010.01701.x

Priestley, C. H. B., & Taylor, R. J. (1972, Feb). On the assessment of surface heat flux and evaporation using large-scale parameters. *Mon. Wea. Rev.*, *100*(2), 81–92. doi: 10.1175/1520-0493(1972)100⟨0081:OTAOSH⟩2.3.CO;2

PRODES-INPE. (2018, Nov). *Taxas anuais de desmatamento.* Retrieved 9 Jan 2019, from `http://www.obt.inpe.br/prodes/index.php` (In Portuguese)

Purves, D., & Pacala, S. (2008, Jun). Predictive models of forest dynamics. *Science*, *320*(5882), 1452-1453. doi: 10.1126/science.1155359

Purves, D. W., Lichstein, J. W., Strigul, N., & Pacala, S. W. (2008, Nov). Predicting and understanding forest dynamics using a simple tractable model. *Proc. Natl. Acad. Sci. U. S. A.*, *105*(44), 17018–17022. doi: 10.1073/pnas.0807754105

Pütz, S., Groeneveld, J., Henle, K., Knogge, C., Martensen, A. C., Metz, M., ... Huth, A. (2014, Oct). Long-term carbon loss in fragmented Neotropical forests. *Nat. Commun.*, *5*. doi: 10.1038/ncomms6037

Pyle, E. H., Santoni, G. W., Nascimento, H. E. M., Hutyra, L. R., Vieira, S., Curran, D. J., ... Wofsy, S. C. (2008, Mar). Dynamics of carbon, biomass, and structure in two Amazonian forests. *J. Geophys. Res.-Biogeosci.*, *113*(G1), G00B08. doi: 10.1029/2007JG000592

Quesada, C. A., Miranda, A. C., Hodnett, M. G., Santos, A. J. B., Miranda, H. S., & Breyer, L. M. (2004, Aug). Seasonal and depth variation of soil moisture in

a burned open savanna (campo sujo) in central Brazil. *Ecol. Appl.*, *14*(sp4), 33–41. doi: 10.1890/01-6017

Quesada, C. A., Phillips, O. L., Schwarz, M., Czimczik, C. I., Baker, T. R., Patiño, S., ... Lloyd, J. (2012, Sep). Basin-wide variations in Amazon forest structure and function are mediated by both soils and climate. *Biogeosciences*, *9*(6), 2203–2246. doi: 10.5194/bg-9-2203-2012

R Core Team. (2019). R: A language and environment for statistical computing [Computer software manual]. Vienna, Austria. Retrieved from `http://www.R-project.org/`

Rappaport, D., Morton, D., Longo, M., Keller, M., Dubayah, R., & dos-Santos, M. N. (2018, Jun). Quantifying long-term changes in carbon stocks and forest structure from Amazon forest degradation. *Environ. Res. Lett.*, *13*(6), 065013. doi: 10.1088/1748-9326/aac331

Ray, D., Nepstad, D., & Moutinho, P. (2005, Oct). Micrometeorological and canopy controls of fire susceptibility in a forested Amazon landscape. *Ecol. Appl.*, *15*(5), 1664–1678. doi: 10.1890/05-0404

Rödig, E., Cuntz, M., Rammig, A., Fischer, R., Taubert, F., & Huth, A. (2018, Apr). The importance of forest structure for carbon fluxes of the Amazon rainforest. *Environ. Res. Lett.*, *13*(5), 054013. doi: 10.1088/1748-9326/aabc61

Russo, S., & Kitajima, K. (2016, Mar). The ecophysiology of leaf lifespan in tropical forests: Adaptive and plastic responses to environmental heterogeneity. In G. Goldstein & L. S. Santiago (Eds.), *Tropical tree physiology: Adaptations and responses in a changing environment* (Vol. 6, pp. 357–383). Cham, Switzerland: Springer International Publishing. doi: 10.1007/978-3-319-27422-5_17

Sabine, C. L., Heimann, M., Artaxo, P., Bakker, D. C. E., Chen, C.-T. A., Field, C. B., ... Valentini, R. (2004). Current status and past trends of the global carbon cycle. In C. B. Field & M. R. Raupach (Eds.), *The global carbon cycle: integrating humans, climate, and the natural world* (Vol. 62, pp. 17–44). Washington, DC, USA: Island Press.

Santiago, L. S., & Wright, S. J. (2007, Feb). Leaf functional traits of tropical forest plants in relation to growth form. *Funct. Ecol.*, *21*(1), 19–27. doi: 10.1111/j.1365-2435.2006.01218.x

Schimel, D., Schneider, F., & JPL Carbon and Ecosystem Participants. (2019). Flux towers in the sky: global ecology from space. *New Phytol.*. (advance online publication) doi: 10.1111/nph.15934

Schneider, F. D., Kükenbrink, D., Schaepman, M. E., Schimel, D. S., & Morsdorf, F. (2019, Apr). Quantifying 3D structure and occlusion in dense tropical and temperate forests using close-range LiDAR. *Agric. For. Meteorol.*, *268*, 249–257. doi: 10.1016/j.agrformet.2019.01.033

Schneider, F. D., Morsdorf, F., Schmid, B., Petchey, O. L., Hueni, A., Schimel, D. S., & Schaepman, M. E. (2017, Nov). Mapping functional diversity from remotely sensed morphological and physiological forest traits. *Nat. Commun.*, *8*(1), 1441. doi: 10.1038/s41467-017-01530-3

Schwarz, G. (1978, Mar). Estimating the dimension of a model. *Ann. Stat.*, *6*(2), 461–464. doi: 10.1214/aos/1176344136

Sena, E. T., Silva Dias, M. A. F., Carvalho, L. M. V., & Silva Dias, P. L. (2018, Dec). Reduced wet-season length detected by satellite retrievals of cloudiness over Brazilian Amazonia: A new methodology. *J. Climate*, *31*(24), 9941–9964. doi: 10.1175/JCLI-D-17-0702.1

Senior, R. A., Hill, J. K., Benedick, S., & Edwards, D. P. (2018, Mar). Tropical forests are thermally buffered despite intensive selective logging. *Glob. Change Biol.*, *24*(3), 1267–1278. doi: 10.1111/gcb.13914

Shao, G., Stark, S. C., de Almeida, D. R., & Smith, M. N. (2019, Feb). Towards high throughput assessment of canopy dynamics: The estimation of leaf area structure in Amazonian forests with multitemporal multi-sensor airborne lidar. *Remote Sens. Environ.*, *221*(221), 1–13. doi: 10.1016/j.rse.2018.10.035

Silva, C. V. J., Aragão, L. E. O. C., Barlow, J., Espírito-Santo, F., Young, P. J., Anderson, L. O., ... Xaud, H. A. M. (2018, Nov). Drought-induced Amazonian wildfires instigate a decadal-scale disruption of forest carbon dynamics. *Philos. Trans. R. Soc. B-Biol. Sci.*, *373*(1760), 20180043. doi: 10.1098/rstb.2018.0043

Silvério, D. V., Brando, P. M., Bustamante, M. M., Putz, F. E., Marra, D. M., Levick, S. R., & Trumbore, S. E. (2019, Mar). Fire, fragmentation, and windstorms: a recipe for tropical forest degradation. *J. Ecol.*, *107*(2), 656–667. doi: 10.1111/1365-2745.13076

Souza Jr., C. M., Siqueira, J., Sales, M. H., Fonseca, A., Ribeiro, J., Numat, ... Barlow, J. B. (2013, Oct). Ten-year Landsat classification of deforestation and forest degradation in the Brazilian Amazon. *Remote Sens.*, *5*(11), 5493–5513. doi: 10.3390/rs5115493

Spracklen, D., Baker, J., Garcia-Carreras, L., & Marsham, J. (2018, Oct). The effects of tropical vegetation on rainfall. *Ann. Rev. Environ. Res.*, *43*(1), 193–218. doi: 10.1146/annurev-environ-102017-030136

Stahl, C., Hérault, B., Rossi, V., Burban, B., Bréchet, C., & Bonal, D. (2013, Dec). Depth of soil water uptake by tropical rainforest trees during dry periods: does tree dimension matter? *Oecologia*, *173*(4), 1191–1201. doi: 10.1007/s00442-013-2724-6

Stark, S. C., Leitold, V., Wu, J. L., Hunter, M. O., de Castilho, C. V., Costa, F. R. C., ... Saleska, S. R. (2012, Dec). Amazon forest carbon dynamics predicted by profiles of canopy leaf area and light environment. *Ecol. Lett.*, *15*(12), 1406–1414. doi: 10.1111/j.1461-0248.2012.01864.x

Stavros, E. N., Schimel, D., Pavlick, R., Serbin, S., Swann, A., Duncanson, L., ... Wennberg, P. (2017, Jun). ISS observations offer insights into plant function. *Nature Ecol. Evol.*, *1*, 0194. doi: 10.1038/s41559-017-0194

Stovall, A. E., Anderson Teixeira, K. J., & Shugart, H. H. (2018, Nov). Assessing terrestrial laser scanning for developing non-destructive biomass allometry. *Forest Ecol. Manag.*, *427*, 217–229. doi: 10.1016/j.foreco.2018.06.004

Strigul, N., Pristinski, D., Purves, D., Dushoff, J., & Pacala, S. (2008, Nov). Scaling from trees to forests: tractable macroscopic equations for forest dynamics. *Ecol. Monogr.*, *78*(4), 523–545. doi: 10.1890/08-0082.1

Sullivan, M. J. P., Lewis, S. L., Affum-Baffoe, K., Castilho, C., Costa, F., Sanchez, A. C., ... Phillips, O. L. (2020, May). Long-term thermal sensitivity of earth's tropical forests. *Science*, *368*(6493), 869–874. doi: 10.1126/science.aaw7578

Sustainable Landscapes Brazil. (2019, Nov). Retrieved 9 Jan 2019, from `https://www.paisagenslidar.cnptia.embrapa.br/webgis/`

Swann, A. L. S., & Koven, C. D. (2017, Aug). A direct estimate of the seasonal cycle of evapotranspiration over the Amazon Basin. *J. Hydrometeor.*, *18*(8), 2173–2185. doi: 10.1175/JHM-D-17-0004.1

Swann, A. L. S., Longo, M., Knox, R. G., Lee, E., & Moorcroft, P. R. (2015,

Dec). Future deforestation in the Amazon and consequences for South American climate. *Agric. For. Meteorol.*, *214–215*, 12–24. doi: 10.1016/j.agrformet.2015.07.006

Tang, H., & Dubayah, R. (2017, Mar). Light-driven growth in Amazon evergreen forests explained by seasonal variations of vertical canopy structure. *Proc. Natl. Acad. Sci. U. S. A.*, *114*(10), 2640–2644. doi: 10.1073/pnas.1616943114

Thonicke, K., Spessa, A., Prentice, I. C., Harrison, S. P., Dong, L., & Carmona-Moreno, C. (2010, Jun). The influence of vegetation, fire spread and fire behaviour on biomass burning and trace gas emissions: results from a process-based model. *Biogeosciences*, *7*(6), 1991–2011. doi: 10.5194/bg-7-1991-2010

Tyukavina, A., Hansen, M. C., Potapov, P. V., Krylov, A. M., & Goetz, S. J. (2016, Feb). Pan-tropical hinterland forests: mapping minimally disturbed forests. *Global Ecol. Biogeogr.*, *25*(2), 151–163. doi: 10.1111/geb.12394

Tyukavina, A., Hansen, M. C., Potapov, P. V., Stehman, S. V., Smith-Rodriguez, K., Okpa, C., & Aguilar, R. (2017, Apr). Types and rates of forest disturbance in Brazilian Legal Amazon, 2000–2013. *Sci. Adv.*, *3*(4), e1601047. doi: 10.1126/sciadv.1601047

Uhl, C., & Buschbacher, R. (1985, Dec). A disturbing synergism between cattle ranch burning practices and selective tree harvesting in the eastern Amazon. *Biotropica*, *17*(4), 265–268. doi: 10.2307/2388588

Uhl, C., & Kauffman, J. B. (1990, Apr). Deforestation, fire susceptibility, and potential tree responses to fire in the Eastern Amazon. *Ecology*, *71*(2), 437–449. doi: 10.2307/1940299

van der Ent, R. J., Savenije, H. H. G., Schaefli, B., & Steele-Dunne, S. C. (2010, Sep). Origin and fate of atmospheric moisture over continents. *Water Resour. Res.*, *46*(9), W09525. doi: 10.1029/2010WR009127

VanWey, L. K., D'Antona, A. O., & Brondízio, E. S. (2007, Jan). Household demographic change and land use/land cover change in the Brazilian Amazon. *Popul. Environ.*, *28*(3), 163–185. doi: 10.1007/s11111-007-0040-y

Veríssimo, A., Barreto, P., Mattos, M., Tarifa, R., & Uhl, C. (1992, Dec). Logging impacts and prospects for sustainable forest management in an old Amazonian frontier: The case of Paragominas. *Forest Ecol. Manag.*, *55*(1–4), 169–199. doi: 10.1016/0378-1127(92)90099-U

Vincent, G., Antin, C., Laurans, M., Heurtebize, J., Durrieu, S., Lavalley, C., & Dauzat, J. (2017, Sep). Mapping plant area index of tropical evergreen forest by airborne laser scanning. a cross-validation study using LAI2200 optical sensor. *Remote Sens. Environ.*, *198*, 254–266. doi: 10.1016/j.rse.2017.05.034

von Caemmerer, S. (2000). *Biochemical models of leaf photosynthesis* (No. 2). Collingwood, VIC, Australia: CSIRO Publishing. doi: 10.1006/anbo.2000.1296

von Randow, C., Manzi, A. O., Kruijt, B., de Oliveira, P. J., Zanchi, F. B., Silva, R. L., ... Kabat, P. (2004, Jun). Comparative measurements and seasonal variations in energy and carbon exchange over forest and pasture in south west amazonia. *Theor. Appl. Climatol.*, *78*(1–3), 5–26. doi: 10.1007/s00704-004-0041-z

Wagner, F., Rossi, V., Stahl, C., Bonal, D., & Hérault, B. (2013, Nov). Asynchronism in leaf and wood production in tropical forests: a study combining satellite and ground-based measurements. *Biogeosciences*, *10*(11), 7307–7321. doi: 10.5194/bgd-10-8247-2013

Walker, W. S., Gorelik, S. R., Baccini, A., Aragon-Osejo, J. L., Josse, C., Meyer, C., ... Schwartzman, S. (2020). The role of forest conversion, degradation, and disturbance in the carbon dynamics of Amazon indigenous territories and protected areas. *Proc. Natl. Acad. Sci. U. S. A.*. (advance online publication) doi: 10.1073/pnas.1913321117

Wright, I. J., Reich, P. B., Westoby, M., Ackerly, D. D., Baruch, Z., Bongers, F., ... Villar, R. (2004, Apr). The worldwide leaf economics spectrum. *Nature*, *428*(6985), 821–827. doi: 10.1038/nature02403

Wright, J. S., Fu, R., Worden, J. R., Chakraborty, S., Clinton, N. E., Risi, C., ... Yin, L. (2017, Aug). Rainforest-initiated wet season onset over the southern Amazon. *Proc. Natl. Acad. Sci. U. S. A.*, *114*(32), 8481–8486. doi: 10.1073/pnas.1621516114

Wu, M., Schurgers, G., Ahlström, A., Rummukainen, M., Miller, P. A., Smith, B., & May, W. (2017, May). Impacts of land use on climate and ecosystem productivity over the Amazon and the South American continent. *Environ. Res. Lett.*, *12*(5), 054016. doi: 10.1088/1748-9326/aa6fd6

Yang, Y., Donohue, R. J., & McVicar, T. R. (2016, Oct). Global estimation of ef-

fective plant rooting depth: Implications for hydrological modeling. *Water Resour. Res.*, *52*(10), 8260–8276. doi: 10.1002/2016WR019392

Zemp, D. C., Schleussner, C.-F., Barbosa, H. M. J., Hirota, M., Montade, V., Sampaio, G., ... Rammig, A. (2017, Mar). Self-amplified Amazon forest loss due to vegetation-atmosphere feedbacks. *Nat. Commun.*, *8*, 14681. doi: 10.1038/ncomms14681

Zhang, K., Castanho, A. D. d. A., Galbraith, D. R., Moghim, S., Levine, N., Bras, R. L., ... Moorcroft, P. R. (2015, Jul). The fate of Amazonian ecosystems over the coming century arising from changes in climate, atmospheric CO_2 and land-use. *Glob. Change Biol.*, *21*(7), 2569–2587. doi: 10.1111/gcb.12903

Supporting Information for "Impacts of Degradation on Water, Energy, and Carbon Cycling of the Amazon Tropical Forests"

Marcos Longo[1],Sassan Saatchi[2,3],Michael Keller[2,4,5],Kevin Bowman[2],António Ferraz[2,3],Paul R. Moorcroft[6],Douglas C Morton[7], Damien Bonal[8],Paulo Brando[9,10,11],Benoît Burban[12],Géraldine Derroire[13],Maiza N dos-Santos[5],Victoria Meyer[2],Scott Saleska[14],Susan Trumbore[15],Grégoire Vincent[16]

[1]NASA Postdoctoral Program Fellow, Jet Propulsion Laboratory, California Institute of Technology, Pasadena CA, United States

[2]Jet Propulsion Laboratory, California Institute of Technology, Pasadena, CA, United States

[3]Institute of Environment and Sustainability, University of California, Los Angeles, CA, United States

[4]International Institute of Tropical Forestry, USDA Forest Service, Rio Piedras, Puerto Rico

[5]Embrapa Informática Agropecuária, Campinas, SP, Brazil

[6]Department of Organismic and Evolutionary Biology, Harvard University, Cambridge, MA, United States

[7]NASA Goddard Space Flight Center, Greenbelt, MD, United States

[8]Université de Lorraine, INRAE, AgroParisTech, UMR Silva, F-54000 Nancy, France

[9]Department of Earth System Science, University of California, Irvine, CA, United States

[10]Woods Hole Research Center, Woods Hole, MA, United States

[11]Instituto de Pesquisa Ambiental da Amazônia, Brasília, DF, Brazil

[12]INRAE, UMR 0745 EcoFoG, Campus Agronomique, Kourou 97379, France

[13]CIRAD, UMR EcoFoG (AgroParisTech, CNRS, INRAE, Univ. Antilles, Univ. Guyane), Kourou 97379, France

[14]University of Arizona, Tucson, AZ, United States

[15]Max-Planck-Institut für Biochemie, Jena, Germany

[16]AMAP, Univ Montpellier, IRD, CIRAD, CNRS, INRAE, Montpellier, 34000 France

Contents to this file

1. Text S1 to S4
2. Figures S1 to S21
3. Table S1 to S4

Additional Supporting Information (Files uploaded separately)

1. Captions for Dataset S1

Introduction

This supporting material provides additional information on the study sites, methodology, and results in the main text. Text S1 provides information on the disturbance history of the selected study regions. Text S2 contains additional information on the airborne lidar and forest inventory plot data used in this study. Text S3 summarizes changes in the ED-2.2 model to improve the representation of forest structure and ecosystem functioning. Text S4 describes in detail the steps needed to obtain ED-2.2 initial conditions from airborne lidar.

Figures S1, S2 and S3 provide additional evaluation of the airborne lidar initialization, specifically the distribution of functional groups, the vertical leaf area index profile, and the evaluation of plots affected by reduced-impact logging in region BTE. Figures S4-

S9 complement the ED-2.2 model evaluation against eddy covariance towers, comparing fortnightly averages for multiple energy, water, and carbon cycle variables. Figure S10 shows the differences in the average seasonal cycle of daytime ground temperature for all the regions simulated by ED-2.2, as functions of the degradation history. Figure S11 shows the ED-2.2 predictions of average seasonal cycle of gross primary productivity as functions of local (patch) aboveground biomass for all focus regions. Figure S12 shows the distribution of evapotranspiration as function of local (patch) biomass and age since last disturbance, during the wet and dry seasons, for three selected regions across the precipitation gradient. Figure S13 shows the local (patch) distribution of leaf area index as a function of aboveground biomass for all the focus regions. Figure S14 shows the drought severity response of intact and degraded forests in region PRG, for multiple carbon and energy variables. Figure S15 complements Figure 9 shows how forest flammability varies as a function of drought length across degradation gradients at additional regions. Figure S16 is part of Text S2 and shows the fitted allometric models relating height, diameter at breast height, and individual leaf area, which are used by both the model initialization and model simulations. Figures S17 and S18 are also part of Text S2 and show multiple trait relationships derived from multiple data sets and implemented in the ED-2.2 model. Figure S19 is part of Text S3 and shows an example of how the vertical distribution of lidar returns is processed to obtain cohorts that are provided to the ED-2.2 model. Figure S19 is also part of Text S3 and shows the results of cross-validation of airborne lidar initialization using aggregated forest inventory plot metrics as benchmarks. Figure S21 is also part of Text S3 and summarizes the distribution of scaling factors to adjust the non-dimensional leaf area density profiles.

Table S1 shows a selection of metrics to assess the ED-2.2 model performance against multiple energy, water, and carbon cycle variables obtained from the eddy covariance towers. Table S2 is part of Text S1 and provides additional information of data used for the five focus regions and the ancillary regions. Table S3 is part of Text S2 and provides detailed information on ED-2.2 model settings. Table S4 is part of Text S3 and lists multiple goodness-of-fit statistics for the fitted models that relate airborne lidar metrics and aggregated, area-based forest properties.

S1. Disturbance history of the study regions

Here we briefly describe the disturbance history for each region, which in some cases comprised multiple sites. The disturbance history of most of the sites in Brazil has been previously described in ? (?), and detailed information on the disturbance history in GYF can be found in ? (?). A summary of data collected in each site is shown in Table S2.

1. *Paracou, French Guiana (GYF).* This is a research field station was established in 1983 to study the dynamics of logged forests under a variety of silvicultural treatments (?, ?). Since then the a broader range of studies on functional ecology and biodiversity have been established at the research station, including the areas of intact forests.

- *Logging experiment (PRC).* Twelve forest inventory plots (6.25 ha) were established to monitor the dynamics of logged forests under different logging treatments. Following the first survey (1984), plots were grouped into three categories according to their forest structure, and plots within categories were randomly assigned to one of the four treatments which were carried out between 1986 and 1988: (T1) conventional selective logging of commercial species (10 trees ha^{-1}; diameter at breast height DBH $\geq$ 50 cm); (T2) conventional logging as in T1, followed by canopy thinning by poison-girdling of non-

commercial species ($30\,\text{trees}\,\text{ha}^{-1}$, DBH $\geq 40\,\text{cm}$); (T3) similar to T2, but the additional logging of non-commercial species ($40 \leq \text{DBH} < 50\,\text{cm}$) for fuelwood; (T4) no treatment. No further logging treatment has been carried out since then. Additional information available in ? (?).

• *Guyaflux site (GFE).* This site is the footprint of the eddy covariance tower at Paracou, which was installed in 2003, along with 10 plots ($0.49 - -1\,\text{ha}$) within the tower footprint. The tower footprint covers mostly large hills with a small valley with a creek and a sandy plateau. See ? (?) for further details about the site.

2. *Belterra, Brazil (BTE).* Throughout the 20^{th} and early 21^{st} centuries, this region experienced multiple economic growth and stagnation cycles, which led to a complex mosaic of deforested and degraded forests interspersed with second-growth forests. Airborne lidar data were collected in four sites along the Cuiabá-Santarém highway, within or near the Tapajós National Forest.

• *Anambé base (ANA).* This site, within the Tapajós National Forest, was assigned as a forest concession for timber harvesting. Selective logging operations were carried out in 2015–2016 using reduced-impact techniques, and aimed at commercial species with DBH $\geq 55\,\text{cm}$ (?, ?).

• *Km 67 base (TNF).* This site is located in one of the ecological corridors within the Tapajós National Forest limits. No indication of recent anthropogenic disturbance exists within this site, which is considered intact forest. However, there is evidence that this intact forest has been previously impacted by drought disturbances both during the 1990s and during the 2015–2016 El Niño events (?, ?, ?, ?).

• *São Jorge (TSJ).* Forest near the settlement of São Jorge were originally within the boundaries of the Tapajós National Forest, but were excluded in 2012. Forests in this site constitute a mosaic of deforestation, fragmentation and degradation from fire and small-scale logging, with some areas experience secondary growth.

• *Eastern Sites (EBT).* The surveyed forests are located outside the Tapajós National Forest. The remaining forests are near several patches of pastures and croplands (mostly soy bean and maize), and thus fragmented and degraded. Logging activities have been occurring in this forests for at least 25 years, and some of the forests experienced one or multiple fires. Post-disturbance regrowth has been also observed in some forests.

3. *Paragominas, Brazil (PRG).* This region experienced significant expansion of selective logging starting in the 1960s, and became the largest center for hardwood processing in Brazil by the early 1990s (?, ?). Since then, agriculture and cattle ranching rapidly expanded, and became the main economic activity, and by the late 2000s about 45% of the forests in Paragominas had been cleared (?, ?). Three sites in the region were studied:

• *Cauaxi (CAU).* This site is privately managed by *Instituto Floresta Tropical*, and has been long used for teaching and training of reduced-impact logging techniques. About 800 ha were designated for logging from 2006 to 2012 (the year of the lidar survey used in this study). Nearly 600 ha of the forests were intact, including some areas within the logging work units that were in steep terrain (slope $> 20°$) and thus not suitable for logging. Selective logging harvested commercial trees (DBH ≥ 55 cm) extracted 11–28 $m^3\,ha^{-1}$ of timber. Additional information in (?, ?).

• *Andiroba (AND).* This site is in a private land and has been partially deforested and remaining forests are moderately degraded and fragmented. Some of the remaining forests

were logged (not using reduced-impact techniques) between 1999 and 2003. Understory forest fires affected the remaining forests in 2001 and 2009 (?, ?).

• *Nova Neonita (PAR).* This site, also in private landholding, is heavily degraded and fragmented. Some of the area was cleared in the 1980s and abandoned in the 1990s, leading to secondary growth. Other surveyed forests were damaged by intensive logging operations in the 1990s and in 2004–2006. Most of the remaining forests suffered extensive damage by three large fire events (1992, 2005, and 2008) (?, ?, ?).

4. *Feliz Natal, Brazil (FZN).* Before logging operations became common in this region in the later 1970s, forests were minimally disturbed. In the 1980s, this region experienced significant changes with widespread deforestation, first for pastures, and later for croplands (mostly soy beans). Because this region has a distinct dry season and also experience episodes of low atmospheric humidity, forests in this region are prone to large, multi-day fires (?, ?, ?). Four sites were surveyed in this region:

• *Long transect (FN2).* This long transect (50×0.2 km) sampled multiple areas with a broad range of disturbance histories typically found in FZN, including areas that were deforested, logged, burned and fragmented. Forest inventory plots were clustered in two segments, at 2 km north and 17 km south of the transect midpoint.

• *Vitória (FNA).* This site included some of the most degraded forests in our sample. Forests had been intensively logged in the 1990s, and experienced at least four severe fire events (2005, 2007, 2010, and 2012) (?, ?). Biomass at the degraded forests was depleted by more than 90% relative to the nearby gallery forests (?, ?).

• *Eastern site (FNC)..* Most forests in this site have been moderately degraded. Widespread selective logging disturbed parts of the surveyed forests between 1993–1996

or 2002–2005 (different locations). Some of the forests logged between 1993–1996 were affected by high-intensity fires in 1999, and since then have only experienced occasional low-intensity fires and additional logging.

• *Western site (FND)..* This area near this site has experienced significant deforestation since the 1980s, leading to highly fragmented forests. The surveyed forests are all within 1.5 km from the forest edge, and experienced high-intensity logging between 1993 and 2003. High-intensity, multi-day fires severely damaged some of the surveyed forests in 2007, 2010, and 2013, and created a range of forest structures due to gradients in disturbance exposure.

5. *Tanguro, Brazil (TAN).* Transitional forests in this region experience long (> 5 mo) and severe dry season and receive relatively low rainfall (1700 mm) (?, ?). The surveyed forests include minimally disturbed forests and forests that are part of a fire experiment.

• *Fire experiment (TGE).* This experiment to understand the dynamics of forests under different fire regimes was established in 2004, when three 50 ha plots were set in the legal reserve of a private property. One plot remained as the control (never burned), one plot was burned every three years (2004, 2007, 2010), and one plot was burned 6 times (every year between 2004 and 2010, except 2008). Fires were set at late dry season (August-September) using fire lines about 100 m apart from each other during 3 or 4 days (reigniting them in case they were extinguished at night). Additional details can be found in (?, ?, ?). After 2010, plots were never burned again. In 2014, two eddy-covariance towers were installed at the experiment site: one within the footprint of the control plot, and another within the footprint of the burned plots (?, ?).

• *Legal reserve (TGW).* This site includes areas immediately to the south and west of the fire experiment, also in the legal reserve of the Tanguro ranch. Surveyed forests generally do not show signs of recent disturbances despite being within 2 km of forest edges. These forests are considered mostly intact, with the exception of a 50 ha patch of forest that burned once in 2007.

S2. Additional information on airborne lidar and forest inventory plots

Each region contained one or multiple sites for which airborne lidar data were available. Many of these sites also contained forest inventory plots, and have been previously used in studies that quantified carbon losses due to degradation in the Amazon and plant area index estimation (?, ?, ?, ?). Table S2 provides additional information on each specific site. Further information on plots can be found in ? (?) (site PRC), ? (?) (site GFE), ? (?) (site TGE), and ? (?), ? (?) and ? (?) (other sites). To reduce the differences among plots regarding size and sampling effort, we considered only living individuals (trees, lianas, and palms) with diameter at breast height $D \geq 10$ cm, and split larger plots ($0.5 - 6.25$ ha) into sub-plots that were as close to 0.25 ha as possible. The location of all inventories in Brazil were geo-registered with sub-meter accuracy using differential Global Navigation Satellite Systems (GeoXH6000); forest inventories in French Guiana were geo-referenced with handheld Global Positioning System, with nominal accuracy of 2 m.

For the study areas in Brazil, airborne lidar data were collected between 2012 and 2017, and surveys used Optech ALTM instruments onboard an aircraft flying at average height of 850m above ground; the sensor scan angle was restricted to 5.6° off-nadir and an average swath sidelap between flight lines of 65% (?, ?); the point cloud data are publicly available

(?, ?). Airborne lidar data at GYF were collected in 2013; the aircraft flew at a height of 550m above ground carrying a Riegl LMSQ560; the scan angle was capped in 20° off-nadir, and the flight line sidelap was near 60% (?, ?). To ensure that the terrain elevation was well characterized, flights had to meet a minimum return density of $4\,\mathrm{m}^{-2}$ of 99.5% of the area (except water bodies and pastures), following previous recommendations for tropical forests (?, ?).

Some of the regions were only used to assist the calibration of the statistical models (Section S4.2), but not used in the simulations. Because our goal was to characterize the impacts of degradation on forest structure and ecosystem functioning, we did not include simulations from MAO, where all surveyed forests were intact, nor did we include JAM and FST, where all forests were logged (albeit using reduced-impact techniques). Forests in SFX were not included because the disturbance history based on Landsat analysis was uncertain due to widespread presence of vines. Finally, at RBR, none of the surveyed forests could be considered intact or logged using reduced-impact techniques, which precluded us to have a minimally-disturbed forest as reference.

S3. Additional ED-2.2 developments

S3.1. Allometric relations

To obtain an allometric equation for diameter at breast height (D, cm) as a function of tree height (H, m), we used all individual tree measurements from the plots included in steps 1 and 2 that were from living trees (excluding lianas and palms), and had field measurements of both D and H ($n = 15865$). Because the sampling effort was not even across tree sizes, and to reduce the effects of variability in tree measurements of height along the D range on local biases, we followed the approach by ? (?) and binned the

data into 50 evenly spaced $\log_e(D)$ classes between $D = 5$ and $D = 200\,\text{cm}$ (the range of D measurements). The binned data were fitted using standardized major axis regression. This choice ensures that the arithmetic inverse relationship (i.e. height as a function of D) could be also used in the ED-2.2 model:

$$\log_e(D) = \underbrace{(-2.01 \pm 0.25)}_{\log_e(d_1)} + \underbrace{(1.68 \pm 0.08)}_{d_2} \log_e(H), \tag{S1}$$

where H should be in m, and D should be in cm. The model fit is shown in Figure S16a.

We did not have any measurement of individual leaf area (L_i, $\text{m}^2_{\text{Leaf}}\,\text{plant}^{-1}$) at the study sites, therefore we developed an allometric equation based on the Biomass And Allometry Database (BAAD; ?, ?). Similar to many allometric equations for aboveground and leaf biomass (e.g., ?, ?), we used ($D^2\,H$) as the predictor. Because we did not seek a reversible equation, we fitted the model using minimum least squares with heteroskedastic distribution of residuals (?, ?, ?). The fitted model was:

$$L_i = \underbrace{(0.234 \pm 0.012)}_{\ell_1} \left(D^2\,H\right)^{\underbrace{0.641 \pm 0.011}_{\ell_2}} + E_{\mathcal{N}}\left[\mu = 0, \sigma = 0.241 \pm 0.026\,L_i^{1.001 \pm 0.056}\right], \tag{S2}$$

where coefficients are presented in the form Expected Value ± Standard Error; units for the empirical equation should be: D in cm, H in m, and L_i in $\text{m}^2_{\text{Leaf}}\,\text{plant}^{-1}$. The model fit is shown in Figure S16b.

In ED-2.2, the carbon stocks ($\text{kgC}\,\text{plant}^{-1}$) of different tissues — leaves (C_L), fine roots (C_R), sapwood (C_S), bark (C_B) and heartwood (C_H) — are defined through allometric equations. Leaf biomass (C_L) is obtained from Equation (S2):

$$C_L = \frac{L_i}{\text{SLA}}, \tag{S3}$$

where SLA ($m^2_{Leaf}\,kgC^{-1}$) is the individual plant's specific leaf area. Fine-root biomass and sapwood biomass are derived from leaf biomass, using the same relationships described in ? (?). Bark biomass followed a parameterization similar to sapwood:

$$C_R = q_R\,C_L, \tag{S4}$$

$$C_S = q_S\,H\,C_L, \tag{S5}$$

$$C_B = q_B\,H\,C_L, \tag{S6}$$

where $q_R = 1$ for all plant functional types, following ? (?). The leaf-to-sapwood (q_S) and leaf-to-bark (q_B) scaling factors (m^{-1}) are determined using the same formulation as ? (?):

$$q_S = \frac{\eta_c\,\mathrm{SLA}\,\rho_W\,1000}{\beta\,A_{L:S}}, \tag{S7}$$

$$q_B = \frac{\eta_c\,\mathrm{SLA}\,\rho_B\,1000}{\beta\,A_{L:B}} \tag{S8}$$

where η_c is an empirical shape parameter based on ? (?) parameterization for broadleaf trees; $A_{L:S}$ and $A_{L:B}$ ($m^2_{Leaf}\,m^{-2}_{Bark}$) are the leaf:sapwood and leaf:bark area ratios, respectively; ρ_W and ρ_B ($g\,cm^{-3}$) are the wood and bark densities, respectively; $\beta = 2.0\,kg\,kgC^{-1}$ is the oven-dry:carbon biomass ratio; and the factor 1000 is included for unit conversion. Values of these parameters are shown in Table S3.

The allometric equation for heartwood biomass (C_H) was obtained using both the pantropical allometric equation for aboveground biomass (C_{AG}, $kgC\,plant^{-1}$; ?, ?), and that total aboveground biomass is the sum of the biomass of the following tissues:

$$C_{AG} = \frac{1}{\beta}\,0.0673\,\left(\rho_W\,D^2\,H\right)^{0.976} \qquad \text{(from ?, ?)} \tag{S9}$$

$$C_{AG} = C_L + f_{AG}\,\left(C_S + C_B + C_H\right), \tag{S10}$$

where f_{AG} is the fraction of biomass above ground; $\beta = 2.0\,\mathrm{kg\,kgC^{-1}}$ is the oven-dry:carbon biomass ratio; and units for S9 should be: ρ_W in $\mathrm{g\,cm^{-3}}$, D in cm, H in m, and C_{AG} in $\mathrm{kgC\,plant^{-1}}$. To simplify the implementation of C_H in ED-2.2, we used Equations (S9), (S10) and (S1) to find C_H at $D = 10\,\mathrm{cm}$ (typical minimum diameter measured in inventories) and at $H = 46\,\mathrm{m}$ (maximum height allowed for tropical trees) and derive a function for C_H with the same form and units as Equation (S9):

$$C_H = \frac{1}{\beta}\,0.0608\,\left(\rho_W\,D^2\,H\right)^{1.004}. \tag{S11}$$

S3.2. Changes in the photosynthesis module

The photosynthesis module in ED-2.2 has been previously described in detail in (?, ?); here we show only a brief overview and highlight the main modifications. Similarly to previous versions, the net CO_2 assimilation rate (A, $\mathrm{molCO_2\,m^{-2}\,s^{-1}}$) for C_3 plants is defined as:

$$A = V_c - \frac{1}{2}V_o - R, \tag{S12}$$

$$V_o = \frac{2\,\Gamma}{c_i}\,V_c, \tag{S13}$$

$$\Gamma = \frac{o}{2\,\tau}, \tag{S14}$$

where V_c, V_o, and R ($\mathrm{molCO_2\,m^{-2}\,s^{-1}}$) are the carboxylation, oxygenation (photorespiration) and day respiration rates, respectively; Γ ($\mathrm{molCO_2\,mol^{-1}}$) is the CO_2 compensation point; ($\mathrm{molCO_2\,mol^{-1}}$) is the intercellular $o = 0.209\,\mathrm{molO_2\,mol^{-1}}$ is the oxygen mixing ratio; and τ is the carboxylase:oxygenase ratio. The terms R, Γ, and τ are calculated the same way as in (?, ?). The carboxylation rate V_c depends on environmental constraints, which ultimately limits the net assimilation rate A.

The maximum carboxylation rate given temperature ($V_c^{\max}$) is defined as in ? (?):

$$V_c^{\max} = \frac{V_{c15}^{\max} Q_V^{\frac{T-T_{15}}{10}}}{\{1+\exp\left[-f\ (T-T_{\rm c})\right]\}\ \{1+\exp\left[+f\ (T-T_{\rm h})\right]\}}, \tag{S15}$$

where $V_{c15}^{\max}$ ($\mathrm{mol\,m^{-2}\,s^{-1}}$) is $V_c^{\max}$ at temperature $T_{15} = 288.15\,\mathrm{K}$ ($15°C$); T (K) is the leaf temperature; Q_V determines the steepness of the temperature dependence of $V_c^{\max}$; f, T_c, and T_h are phenomenological parameters that reduce $V_c^{\max}$ at extreme temperatures, following the same formulation used in previous ED versions (?, ?, ?).

The maximum carboxylation rate can never be achieved because CO_2 inhibts oxygenation, and O_2 inhibits carboxylation (?, ?). The carboxylation rate at saturated Ribulose-1,5-Biphosphate (RuBP) conditions ($V_c^{\rm RuBP}$) is determined as:

$$V_c^{\rm RuBP} = V_c^{\max}\,\frac{c_i}{c_i + K_c\left(1+\dfrac{o}{K_o}\right)}, \tag{S16}$$

where K_c ($\mathrm{molCO_2\,mol^{-1}}$) and K_o ($\mathrm{molO_2\,mol^{-1}}$) are the Michaelis constants for carboxylation and oxygenation, respectively, and are also calculated as in (?, ?). Equation (S16) is the same described in (?, ?).

The RuBP regeneration depends on the electric transport rate (J, $\mathrm{mol\,m^{-2}\,s^{-1}}$), which in turns depends on the absorbed irradiance (I, $\mathrm{mol\,m^{-2}\,s^{-1}}$). If I is relatively low, then RuBP pools may decline, limiting the carboxylation rate. The RuBP-limited (also known as light-limited) carboxylation rate ($V_c^{\rm PAR}$) is defined as in ? (?):

$$V_c^{\rm PAR} = \frac{J}{4+8\,\dfrac{\Gamma}{c_i}}, \tag{S17}$$

and J is determined from an empirical quadratic equation (?, ?, ?):

$$J = \frac{(I_{\rm PSII}+J^{\max}) - \left[(I_{\rm PSII}+J^{\max})^2 - 4\,\varphi\,I_{\rm PSII}\,J^{\max}\right]^{\frac{1}{2}}}{2\,\varphi} \tag{S18}$$

$$J^{\max} = \frac{J_{15}^{\max} Q_J^{\frac{T-T_{15}}{10}}}{\{1+\exp\left[-f_c\ (T-T_{\rm c})\right]\}\ \{1+\exp\left[+f_h\ (T-T_{\rm h})\right]\}} \tag{S19}$$

$$I_{\mathrm{PSII}} = \frac{1}{2}\,\gamma_{\mathrm{PSII}}\,I \tag{S20}$$

where $J^{\max}$ ($\mathrm{mol\,m^{-2}\,s^{-1}}$) is the temperature-dependent maximum electron transport rate; $J_{15}^{\max}$ and Q_J are the equivalent of $V_{c15}^{\max}$ and Q_V for the electron transport rate, respectively; I_{PSII} ($\mathrm{mol\,m^{-2}\,s^{-1}}$) is the light effectively used by the photosystem II; $\varphi = 0.7$ is an empirical curvature parameter (?, ?, ?); $\gamma_{\mathrm{PSII}} = 0.85$ is the quantum yield of the photosystem II (?, ?, ?); and T_c, T_h, f_c, and f_h are empirical parameters to downscale photosynthetic activity at extreme temperatures (Table S3). Unlike the original implementation of V_c^{PAR} (?, ?, ?) the explicit representation on electron transport rate is advantageous because it accounts for the differences in temperature dependence of $J^{\max}$ and $V_c^{\max}$ (?, ?), and the saturation behavior of J as I becomes non-limiting.

In addition to light limitation, carboxylation rates may be limited by the triose phosphate utilization (TPU) for synthesizing sugars and starch (?, ?). The TPU limitation typically occurs when both CO_2 mixing ratio and irradiance are high, or when temperature is low (?, ?, ?), and is expected to become more important as atmospheric CO_2 increases (?, ?). The TPU-limited carboxylation rate (V_c^{TPU}) is defined as:

$$V_c^{\mathrm{TPU}} = 3\,E_{\mathrm{TP}}\,\frac{c_i}{c_i - \Gamma}, \tag{S21}$$

where E_{TP} ($\mathrm{mol\,m^{-2}\,s^{-1}}$) is the export rate of triose phosphate from chloroplasts, and is normally parameterized as a function of $V_c^{\max}$ ($E_{\mathrm{TP}} = \varepsilon_E\,V_c^{\max}$; ?, ?, ?, ?).

Similar to previous versions of ED-2, the net assimilation rate is determined through a law of minimum:

$$A = \min\left(A^{\mathrm{RuBP}}, A^{\mathrm{PAR}}, A^{\mathrm{TPU}}\right) \tag{S22}$$

where each of the cases on the right-hand side are calculated from Equations (S12) and (S13), by replacing V_c with each of the cases (Equations S16, S17, and S21), and using the algorithm described in ? (?).

Both $J_{15}^{\max}$ and E_{TP} are assumed to be proportional to $V_{c15}^{\max}$. To obtain the proportionality ratios, we used the data collected at multiple sites in Panama (?, ?, ?). Even though the ? (?) provided fits relating these quantities, we refitted the functions to eliminate the intercept, and corrected for the fact that ? (?) provides values at 25°C and ED-2.2 needs the reference at 15°C:

$V_c^{\max}$ ($J_{15}^{\max} = \varepsilon_J \, V_{c15}^{\max}$)

The values of ε_J and ε_E are determined from the data collected at multiple sites in Panama and described in ? (?). Although ? (?) provided empirical fits relating $V_c^{\max}$, $J^{\max}$ and E_{TP}, we obtained the relationships using standardized major axis (SMA) to account for the variability on both variables, and corrected for the fact that ? (?) values use a different reference temperature (25°C):

$$\varepsilon_J = \underbrace{\frac{J_{25}^{\max}}{V_{c25}^{\max}}}_{\varepsilon'_J} \frac{Q_V}{Q_J}, \tag{S23}$$

$$\varepsilon E = \frac{E_{\mathrm{TP}}}{V_{c25}^{\max}}, \tag{S24}$$

where $J_{25}^{\max}$ and $V_{c25}^{\max}$ are the values at 25°C, obtained directly from ? (?). The SMA line, coefficients ε'_J and ε_E and the R^2 are shown in Figure S17.

S3.3. Updated trait and trade-off relationships

In ED-2.2, we represent the functional diversity within ecosystems by defining multiple plant functional types (PFTs). PFTs are defined by both morphological characteristics (e.g. tree or grass) and by a set of traits that determine a variety of life strategies within the

ecosystems. Many traits and trade-offs of tropical forest PFTs had not been changed since the original ED-1.0 release (?, ?), despite the increase in data availability for the tropics. Here, we aggregated data from multiple trait-based studies and trait data bases such as GLOPNET and TRY (?, ?, ?, ?, ?, ?, ?, ?, ?, ?, ?, ?), to revise the values associated with each PFT. For this revision, we focused on the following traits: wood density, leaf turnover rate, specific leaf area, leaf carbon:nitrogen ratio, maximum carboxylation rate, maximum electron transport rate, and maximum triose-phosphate utilization rate. These traits were selected because we obtained a sufficiently large ($n > 50$) number of samples that could be used to build trade-off relationships and were already used to define trade-offs in ED-2.2, and traits known to directly or indirectly influence gross primary productivity and thus light- and water-use efficiencies. To remove confounding factors such as canopy position, we only used data for sun leaves, or individuals that were either emergent or canopy trees.

Wood density was the most widely available trait in our data base, and also the indicative trait used to define PFTs in ED-1.0 (?, ?). To re-define the PFTs, we used the data from all forest inventory plots available, attributed wood density for each individual using the wood density data base compiled by ? (?). We then calculated the probability distribution function of wood density (weighted by basal area), and split the distribution based on quantiles (the lower, middle, and upper 33% of the distribution associated with early-successional, mid-successional, and late-succesional trees, respectively). The expected values of wood density for each PFT was assumed to be the mid-point within each quantile (i.e. 16.67%, 50%, and 83.33% quantiles, respectively).

To determine the trade-off axes between traits, we fitted standardized major axes (SMA). Because most wood density data came from the ? (?) compilation (only wood

density data were available), we aggregated data to species to seek relationships between wood density and other traits. Most traits were not correlated with wood density: leaf turnover rate showed the most significant, yet weak correlation with wood density (Figure S18a). For leaf traits, we were able to obtain large number of paired observations (i.e. two trait measurements from the same individual) between specific leaf area (SLA) and the other traits, and thus we fitted the standardized major axes using SLA as one of the variables (Figures S18b, S18c, and S18d).

The revised trait values for the plant functional types used in these simulations are shown in Table S3.

S4. ED-2.2 initial conditions using airborne lidar

The approach to obtain initial conditions for ED-2 using airborne lidar data is summarized in three steps: (1) derivation of unscaled vertical profiles of leaf area density from the vertical distribution of returns, and the height-dependent proportion of leaf area density allocated to each plant functional type; (2) estimation of plot-level properties of the forest (biomass, basal area, and individual's stem density) from airborne lidar; (3) optimization of scaling factors to obtain absolute leaf area density profiles and the initial conditions for ED-2. This approach requires only representative, geo-referenced forest inventory plots for calibration, and small-footprint, discrete-return airborne lidar point cloud data with high density of returns, in addition to knowledge of individual-based allometric equations that relate diameter at breast height (D) to tree height, above-ground biomass and leaf biomass.

S4.1. Vertical foliage profiles

To obtain vertical profiles of leaf area density (Figure 2, Box 1) across the areas surveyed by airborne lidar, we first clipped the full point cloud domain into $50 \times 50\,\mathrm{m}$ columns. For each column, we simulated a pseudo-waveform from the discrete point clouds to create a continuous and smooth distribution of return energy in the vertical (see one example in Figure S19a). Our simulated waveform function (E) is based on the algorithm described by ? (?) and ? (?):

$$E\left(h_i\right) = X\left(h\right) * Z\left(h, h_i\right), \tag{S25}$$

$$X\left(h\right) = \sum_{n=1}^{N} \begin{cases} 1 \text{ if } h_n \in \left[h - \dfrac{\Delta h}{2}; h + \dfrac{\Delta h}{2}\right] \\ 0 \text{ otherwise} \end{cases}, \tag{S26}$$

$$Z\left(h, h_i\right) = \frac{1}{\sigma_h \sqrt{2\,\pi}} \exp\left[-\frac{\left(h - h_i\right)^2}{2\,\sigma_h^2}\right], \tag{S27}$$

where h_i is the mean elevation of each bin; $\Delta h = 10\,\mathrm{cm}$ is the thickness of each bin layer; $X\left(h\right)$ is the energy distribution function across the laser beam trajectory (horizontal); $Z\left(h\right)$ is the energy distribution function in the vertical (i.e. along the laser beam trajectory); σ_z is the pulse width in the vertical, which controls the smoothness of the simulated waveform; and $*$ is the convolution operator. Similar to ? (?), we binned the return counts before applying the convolution to improve computational efficiency. When the goal is to simulate the signal of large-footprint waveform lidar (e.g. GLAS or GEDI), the energy distribution function across the laser beam trajectory is frequently assumed Gaussian (?, ?, ?, ?). In our case, however, we sought to characterize the average vegetation profile for the entire column and assumed a uniform (rectangular) distribution across the entire column area instead (Eq. S26). In addition, as we will discuss in later in this text, it is important that the waveform is not excessively noisy to obtain realistic leaf area index,

yet it should retain sufficient features to ensure the vegetation structure is not overly aggregated (Figure S19a). We defined $\sigma_h = 50\,\mathrm{cm}$ which resulted in a good compromise in preliminary tests. Finally, following ? (?), we calculated the waveform functions for vegetation (E_v) and ground (E_g) returns separately, in order to obtain the integrated return energy (R_v and R_g):

$$R_v\left(h_i\right) = \sum_{j=i}^{N_I} E_v\left(h_j\right), \tag{S28}$$

$$R_g = \sum_{j=1}^{N_I} E_g\left(h_j\right), \tag{S29}$$

where N_I is the total number of layers. In our case, we defined layers up to $h_T = 70\,\mathrm{m}$ to ensure that the tallest sampled trees would be completely characterized.

To obtain the relative vertical distribution of leaf area density ($\lambda\left(h\right)$; $\mathrm{m}^2_{\mathrm{Leaf}}\,\mathrm{m}^{-2}$), we applied the Beer-Lambert light extinction approach, following the approach originally developed by ? (?) and adapted for lidar profiles (e.g., ?, ?, ?, ?). In this approach, $\lambda\left(h\right)$ is a function of the gap probability (P, non-dimensional):

$$\lambda(h) = \frac{\cos\varphi}{G\left(h,\varphi\right)} \frac{1}{P\left(h,\varphi\right)} \frac{\partial P\left(h,\varphi\right)}{\partial h}, \tag{S30}$$

where h is the height, φ is the angle of incident light, and $G\left(h,\varphi\right)$ is the leaf area projection factor. For most lidar surveys used in this study, the maximum off-nadir scan angle was 5.5° (?, ?); the only exception was Paracou (GYF), where the off-nadir angle was 20° (?, ?). As a first approximation, we assumed $\varphi \approx 0$, and thus $P\left(h,\varphi\right) \approx P\left(h\right)$, but we acknowledge that this introduces an error ($5 - 8\%$ for 10% of the points at GYF). The leaf area projection factor is dependent upon the mean leaf orientation. For simplicity, we assumed isotropic (random) orientation, i.e. $G\left(h,\varphi\right) = 0.5$ (?, ?, ?).

Following ? (?), the vertical profile of gap probability can be described by the integral of the lidar return energy $[R_v(h)]$ between height h and the top canopy height (h_T):

$$-\frac{\mathrm{d}R_v\left(h\right)}{\mathrm{d}h} \;=\; J_0\, r_v \frac{\mathrm{d}P\left(h\right)}{\mathrm{d}h}, \tag{S31}$$

where J_0 is the irradiance emitted by the lidar sensor and r_v is the canopy reflectivity. Using the boundary conditions at the top canopy $[R_v\left(h_T\right) = 0; P\left(h_T\right) = 1]$ and that the total energy reflected by the ground is proportional to the total gap fraction, we obtain:

$$R_v\left(h_i\right) \;=\; J_0\, r_v \left[1 - P\left(h_i\right)\right], \tag{S32}$$

$$R_{v0} \;=\; J_0\, r_v \left[1 - P\left(h = 0\right)\right], \tag{S33}$$

$$R_g \;=\; J_0\, r_g\, P\left(h = 0\right), \tag{S34}$$

where r_g is the soil reflectivity and $R_{v0} = R_v\left(h = 0\right)$. The irradiance emitted by the sensor (J_0) is not provided in the data set, however it is possible to combine Equations (S32)-(S34) to suppress J_0 from the definition of $P\left(h\right)$:

$$P\left(h_i\right) \;=\; 1 - \frac{R_v\left(h_i\right)}{R_{v0} + k_r\, R_g}, \tag{S35}$$

where $k_r = \frac{r_v}{r_g}$, the ratio between vegetation and ground reflectivities. By substituting Equations (S31), (S33), and (S35) into Equation (S30) for the $\varphi = 0; G = 0.5$ case, we obtain:

$$\lambda\left(h\right) \;=\; 2\,\frac{\mathrm{d}}{\mathrm{d}h} \ln\left[R_{v0} + k_r\, R_g - R_v\left(h\right)\right]. \tag{S36}$$

It is possible to determine k_r from airborne lidar surveys that have reflectance data (?, ?), or from optimization using independent local measurements of leaf area index (?, ?). Neither information is easily obtained for large areas, and thus we assumed $k_r = 1.03$, following ? (?). We found that the results are not sensitive to small variations in k_r,

366 particularly when the gap fraction is low. On the other hand, the approximation of return
367 counts is only a proxy to the return energy, and therefore, we assumed that the profile
368 obtained from Equation (S36) was considered unscaled, and will be referred as $\lambda^{\star}(h)$.
369 Following ? (?), we excluded the profile below 5 m, as estimates of leaf area density near
370 the surface often show large uncertainty due to the limited fraction of returns near the
371 surface in denser canopies.

372 Cohorts in ED-2 are defined as discrete groups of individuals with similar size and same
373 life strategy (plant functional type; PFT). To separate the vertical profile into discrete
374 layers of similar size, we assumed that the layers with the most significant population can
375 be identified by local maxima, or by local saddle points when the layers are not completely
376 separated, as shown in Figure S19b. The boundary between consecutive layers is defined as
377 either the local minima or inflection points that are not saddle points (Figure S19b). These
378 features were automatically determined based on the function `peaks` (package `RSEIS`, ?,
379 ?), which was modified to capture inflection points and local minima.

380 The last stage of step 1 was to attribute the fraction of each plant functional type in each
381 vertical layer, which was used to define the cohorts (Figure S19c). Because the airborne
382 lidar data was from a single band, we could not use spectral mixture analyses (e.g., ?, ?).
383 To overcome this limitation, we also simulated waveforms for all plots that had complete
384 overlap with airborne lidar data in all of the study sites, and complemented with data
385 from the Sustainable Landscapes Brazil project (?, ?, ?, ?) (total of 817 $0.25 - ha$ plots).
386 For each plot, we determined the expected relative proportion of each PFT p (early-
387 successional, ETR; mid-successional, MTR; and late-successional, LTR) as a function of
388 height ($q_p(h)$) and the associated profile of return heights and built a look-up table. The

normalized profile of each column was compared with the normalized profile of all plots in the look-up table using the Kolmogorov-Smirnov test, and the least dissimilar profile found in the look-up table was used to determine the relative proportion of PFTs in the column of interest (Figure S19c).

S4.2. Statistical models for plot-level properties

For the second step (Figure 2, Box 2), we developed parametric statistical models that related summary metrics describing the distribution of return heights with four plot-level properties ($D \geq 10\,\mathrm{cm}$): aboveground biomass carbon density (ABCD, $\mathrm{kg_C\,m^{-2}}$), basal area (BA, $\mathrm{cm^2\,m^{-2}}$), (maximum, allometry-based) leaf area index (LAI, $\mathrm{m^2_{Leaf}\,m^{-2}}$), and stem number density (ND, $\mathrm{m^{-2}}$). Similar to Step 1 (Section S4.1), we considered again all plots that were entirely within the areas surveyed by airborne lidar (total of 817 $0.25-$ha plots, Section 4). For each plot-level property, we selected the most informative yet simple model using the subset selection of regression method method (?, ?). Additionally, we only considered models that did not show strong signs of multicollinearity, quantified by the variance inflation factor (VIF < 4). The selected model was fitted assuming heteroskedastic distribution of residuals (?, ?, ?). Field inventory above-ground biomass was determined using the same models as in ? (?). Individual-based maximum leaf area was determined using an allometric model derived from the Biomass And Allometry Database (BAAD; ?, ?) and presented in Section S4.3.

We obtained the following models:

$$\begin{aligned}\mathrm{ABCD_{ALS}} \;=\; & 0.132^{+0.072}_{-0.045}\;\; \mu_h^{\,1.59^{+0.14}_{-0.14}} \\ & + E_{\mathcal{N}}\left[\mu = 0, \sigma = 0.95^{+0.35}_{-0.25}\;\; \mathrm{ABCD}_{\mathrm{ALS}}^{\,0.49^{+0.15}_{-0.13}}\right], \end{aligned} \tag{S37}$$

$$\begin{aligned}
\mathrm{BA}_{\mathrm{ALS}} &= 1.81^{+1.19}_{-0.65}\ \exp\left[-5.77^{+1.19}_{-0.94}\ f_{1-2.5}\right] h_{75}^{0.85^{+0.12}_{-0.15}} \\
&\quad + E_{\mathcal{N}}\left[\mu = 0, \sigma = 1.45^{+1.54}_{-0.39}\ \mathrm{BA}_{\mathrm{ALS}}^{0.39^{+0.16}_{-0.26}}\right], \qquad \text{(S38)} \\
\mathrm{LAI}_{\mathrm{ALS}} &= 0.37^{+0.33}_{-0.13}\ \exp\left[-5.8^{+1.7}_{-2.0}\ f_{1-2.5}\right] \mu_h^{0.91^{+0.12}_{-0.20}} \\
&\quad + E_{\mathcal{N}}\left[\mu = 0, \sigma = 0.462^{+0.141}_{-0.045}\ \mathrm{LAI}_{\mathrm{ALS}}^{0.49^{+0.14}_{-0.22}}\right], \qquad \text{(S39)} \\
ND_{\mathrm{ALS}} &= 0.0337^{+0.0053}_{-0.0083}\ \exp\left[-8.5^{+2.0}_{-1.8}\ f_{1-2.5} + 0.77^{+0.31}_{-0.17} F_{7.5}\right] \\
&\quad + E_{\mathcal{N}}\left[\mu = 0, \sigma = 0.038^{+0.069}_{-0.027}\ \mathrm{ND}_{\mathrm{ALS}}^{0.37^{+0.26}_{-0.40}}\right], \qquad \text{(S40)}
\end{aligned}$$

where $f_{1-2.5}$ is the fraction (range $0.0 - 1.0$) of returns coming from the layer between 1 and 2.5 m; $F_{7.5}$ is the fraction (range $0.0 - 1.0$) of returns from above 7.5 m; h_{75} is the third quartile of the distribution of return heights; and μ_h is the mean of the distribution of return heights. Numbers after the coefficients are the 68% range (equivalent to $\pm 1\sigma$ if the distribution was Gaussian) of 1000 replicates using a nested bootstrap sampling. We separated the plots by study regions, then for each replicate, we first randomly selected which study regions to include in the model fitting stage, then randomly selected plots from the these regions. Plots from regions excluded from the model fitting stage were used for cross-validation.

The fitted models for ABCD, BA, and LAI showed similar-quality fits, and both explained over 70% of the inventory-plot variance (Table S4), whereas the model for ND explained 64% of the observed variance (Figure S20c; Table S4). Cross-validation assessment show that all fitted models are robust: models show similar fraction of unexplained variance, and none of them are significantly biased (Figure S20; Table S4).

S4.3. Plot-specific scaling factors and absolute cohort demography

For the third step of this approach (Figure 2, box 3), the unscaled profiles obtained in step 1 were calibrated using the stem number density (ND), basal area (BA) and above-ground biomass carbon density (ABCD) estimated from the parametric models developed in step 2. First, we obtain the unscaled leaf area index of each cohort layer i ($\Lambda_i^\star$):

$$\Lambda_i^\star = \int_{h_i^-}^{h_i^+} \lambda^\star(h)\,\mathrm{d}h, \tag{S41}$$

where $\left(h_i^-; h_i^+\right)$ are the lower and upper bounds of the discrete layer associated with cohort i (Figure S19). We then estimated the unscaled stem number density of cohort i ($n_i^\star$, m^{-2}) following the same approach by ? (?), which assumes that the leaf area index is directly proportional to $n_i^\star$, and individual leaf area (L_i, $\mathrm{m}^2_{\mathrm{Leaf}}\,\mathrm{plant}^{-1}$), assumed to be a function of the tree size:

$$n_i^\star = \frac{1}{L_i\left(D_i, H_{t_i}\right)}\,\Lambda_i^\star, \tag{S42}$$

where D_i (cm) is the diameter at breast height, and H (m) is the tree height. Neither L_i nor D_i can be directly retrieved by airborne lidar, therefore we developed allometric equations based on available data. To be consistent with the ED-2.2 simulations, we used the allometric equations for height and individual leaf area described in Supplement S3.1.

The unscaled stem number density of each cohort ($n_i^\star$) is obtained by substituting Equations (S2) and (S1) into Equation (S42):

$$n_i^\star = \nu_1\,H^{\nu_2}\,\Lambda_i^\star, \tag{S43}$$

$$\nu_1 = \frac{1}{\ell_1\,d_1^{2\,\ell_2}}, \tag{S44}$$

$$\nu_2 = -\left(2\,d_2+1\right)\,\ell_2. \tag{S45}$$

Once all $n_i^\star$ values are determined, it is possible to derive unscaled, column-aggregated values of aboveground biomass carbon density (ABCD*), basal area (BA*) and stem number density (ND*):

$$\mathrm{ABCD}^\star = \sum_{i=1}^{I}\left(n_i^\star\, f_C\, a_1\, \left\{\rho_{p(i)}\, \left[D\left(H\right)\right]^2\, H\right\}^2\right), \tag{S46}$$

$$\mathrm{BA}^\star = \sum_{i=1}^{I}\left\{n_i^\star\, \frac{\pi}{4}\, \left[D\left(H\right)\right]^2\right\}, \tag{S47}$$

$$\mathrm{LAI}^\star = \sum_{i=1}^{I}\left\{n_i^\star\, \Lambda_i^\star\right\}, \tag{S48}$$

$$\mathrm{ND}^\star = \sum_{i=1}^{I} n_i^\star, \tag{S49}$$

where I is the total number of cohorts in the analyzed column, $(\rho_{\mathrm{ETR}}; \rho_{\mathrm{MTR}}; \rho_{\mathrm{LTR}}) = (0.450; 0.615; 0.790)$ g cm^{-3} are the wood density values for each PFT $p(i)$, and $(a_1; a_2) = (0.0673; 0.976)$ are the empirical coefficients from the pantropical allometric equation developed by ? (?). The unscaled values are compared with the properties estimated using the statistical model using airborne-lidar metrics (Section S4.2), denoted by $\left(\mathrm{ND}^\odot; \mathrm{BA}^\odot; \mathrm{LAI}^\odot; \mathrm{ABCD}^\odot\right)$:

$$e_A = \frac{\mathrm{ABCD}^\odot}{\mathrm{ABCD}^\star}, \tag{S50}$$

$$e_B = \frac{\mathrm{BA}^\odot}{\mathrm{BA}^\star}, \tag{S51}$$

$$e_L = \frac{\mathrm{LAI}^\odot}{\mathrm{LAI}^\star}, \tag{S52}$$

$$e_N = \frac{\mathrm{ND}^\odot}{\mathrm{ND}^\star}, \tag{S53}$$

where $(e_A; e_B; e_L; e_N)$ are the scaling factor that would match the estimates from the third step with estimates from the first step. The minimum overall error when taking all variables into account can be determined from the global minimum of function S based

on the weighted least squares:

$$S(e) = \frac{w_A\ (e - e_A)^2 + w_B\ (e - e_B)^2 + w_L\ (e - e_L)^2 + w_N\ (e - e_N)^2}{w_A + w_B + w_L + w_N}, \tag{S54}$$

where $(w_A; w_B; w_L; w_N) = (0.279; 0.251; 0.292; 0.177)$ are the weights of ABCD, BA, LAI, and ND, respectively, and are proportional to the inverse of the fraction of unexplained variance for the full model (Table S4). The scaling factor e that minimizes can be determined analytically:

$$e = \frac{w_A\, e_A + w_B\, e_B + w_L\, e_L + w_N\, e_N}{w_A + w_B + w_L + w_N}, \tag{S55}$$

which is equivalent to the weighted average of the scaling factors. The scaled number density of each cohort i is then assumed to be $n_i = e\, n_i^\star$.

S4.4. General scaling factor

The scaling factor in step 3 (Equation S55) could be obtained for any airborne lidar column, as it only relies on the local vertical profile of returns (Section S4.1) and statistical models based on airborne lidar metrics (Equations S37–S40). However, the statistical models (Equations S37–S40) are based on plots with $D \geq 10\,\text{cm}$, which is relatively high for the most degraded forests. Consequently, the statistical models cannot fully constrain the leaf area density profiles at the most degraded forests, because the return energy above 11 m (equivalent to $D \geq 10\,\text{cm}$) may represent a small fraction of the return energy. To overcome this limitation introduced by the lack of small trees in our forest inventory data set, we sought to define a characteristic scaling factor that could be applied to all lidar scenes. To do so, we used the results from the regional cross validation at all sites (Table S2) to analyze the distribution of scaling factors e. The distribution of factors from all the plots are shown in Figure S21. The distribution has a well-defined peak, and

the mode of the global distribution is close to the median value $e_{50} = 1.357$. Although the distribution of factors vary by each site (Figure S21b), for simplicity we used a single factor equivalent to the median at all sites.

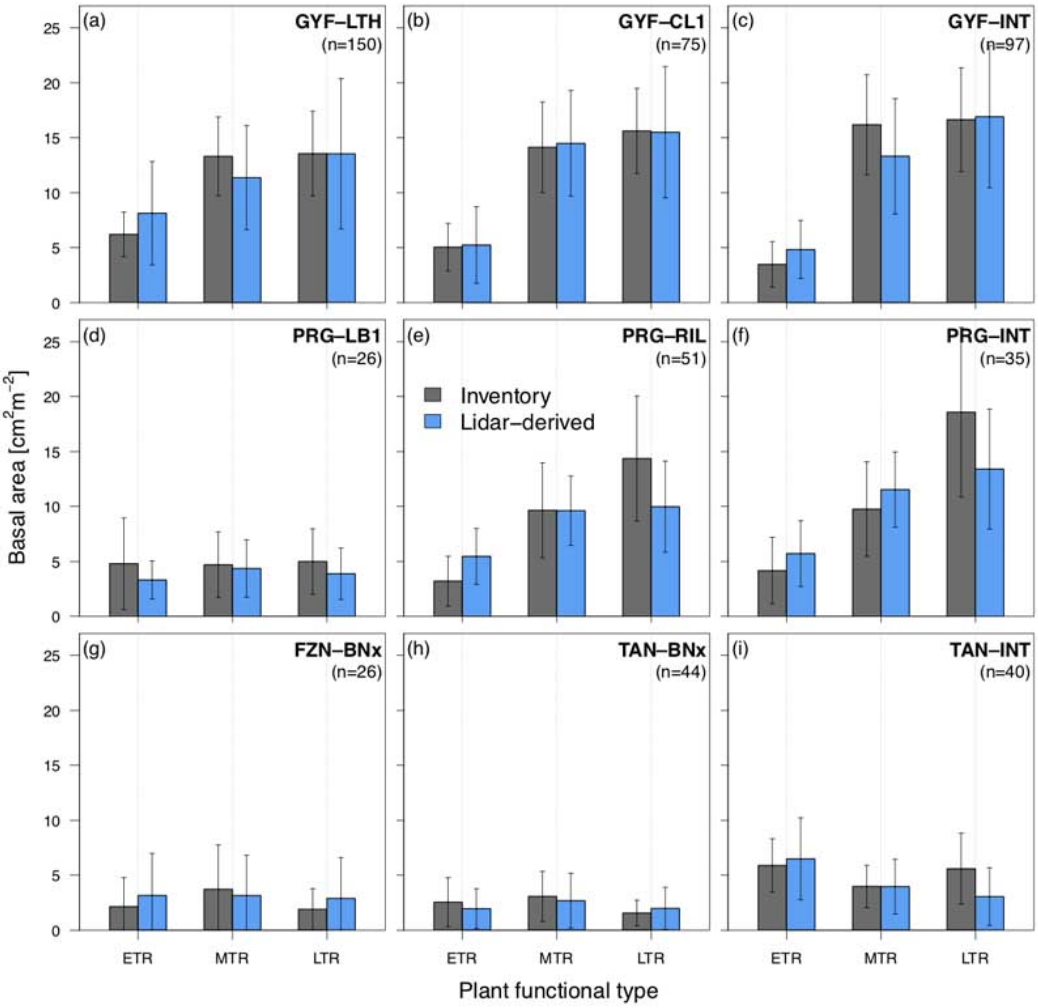

Figure S1. Assessment of basal area by plant functional types (PFTs), for different study regions and degradation levels. Plant functional types are early-successional tropical tree (ETR), mid-successional tropical tree (MTR) and late-successional tropical tree (LTR). Grey bars are obtained from forest inventory plots, and blue bars are obtained from the airborne lidar initialization using a 612-fold regional cross-validation (i.e. excluding all plots from region in the calibration stage). Whiskers correspond to the standard deviation either across all plots in the same category (inventory) or across all plots and replicates (lidar). Sites: GYF – Paracou, PRG – Paragominas, FZN – Feliz Natal, TAN – Tanguro. Disturbance classes: BNx – Burned twice or more, CL1 – conventional logging (once), LB1 – logged and burned once, LTH – logged and thinned, RIL – reduced-impact logging, INT – intact.

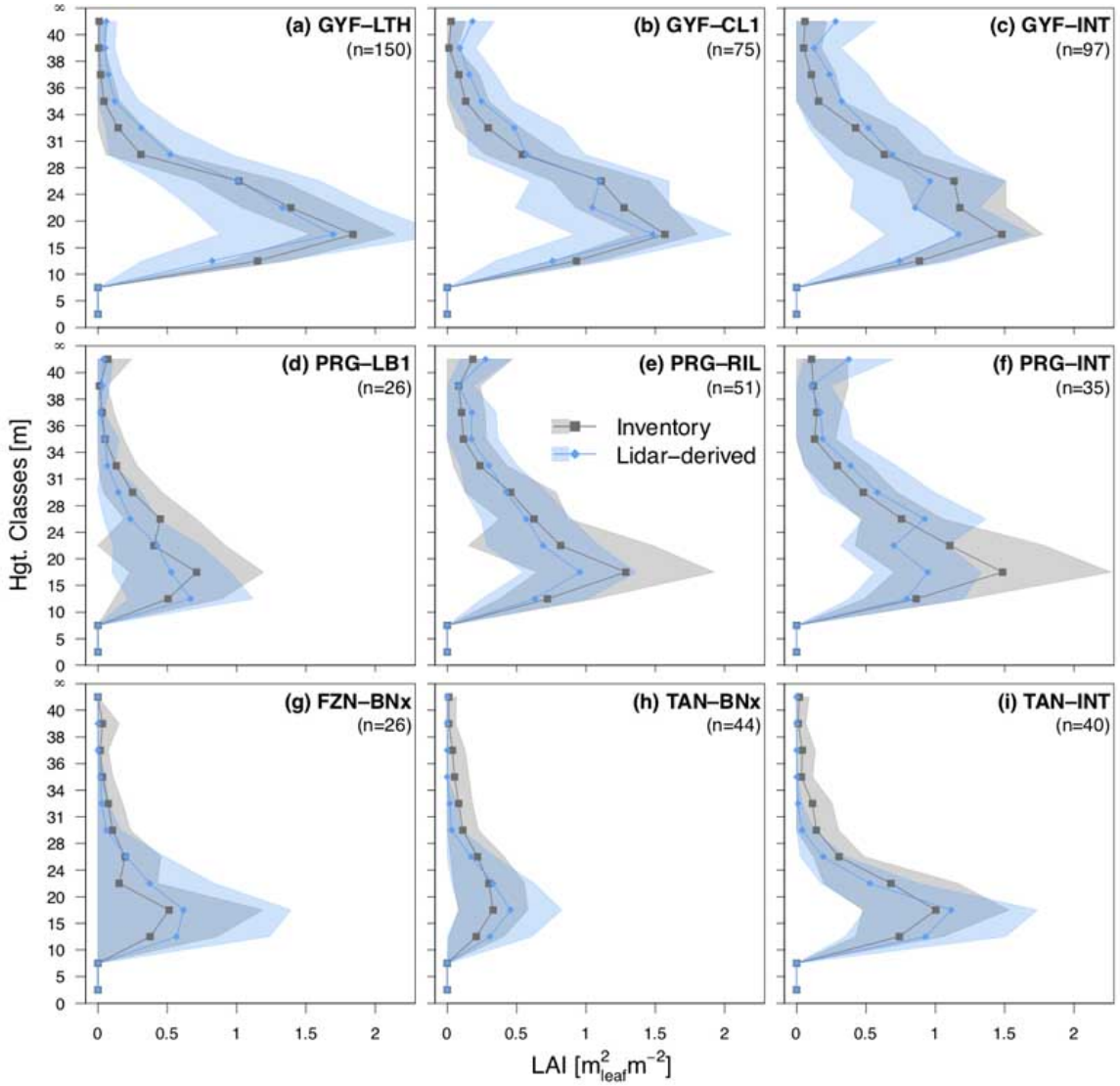

Figure S2. Assessment of leaf area index distribution as a function of height for different study regions and degradation levels. Grey points are obtained from forest inventory plots, and blue points are obtained from the airborne lidar initialization using a 612-fold regional cross-validation (i.e. excluding all plots from region in the calibration stage). Bands around points correspond to the standard deviation either across all plots in the same category (inventory) or across all plots and replicates (lidar). Sites: GYF – Paracou, PRG – Paragominas, FZN – Feliz Natal, TAN – Tanguro. Disturbance classes: BNx – Burned twice or more, CL1 – conventional logging (once), LB1 – logged and burned once, LTH – logged and thinned, RIL – reduced-impact logging, INT – intact.

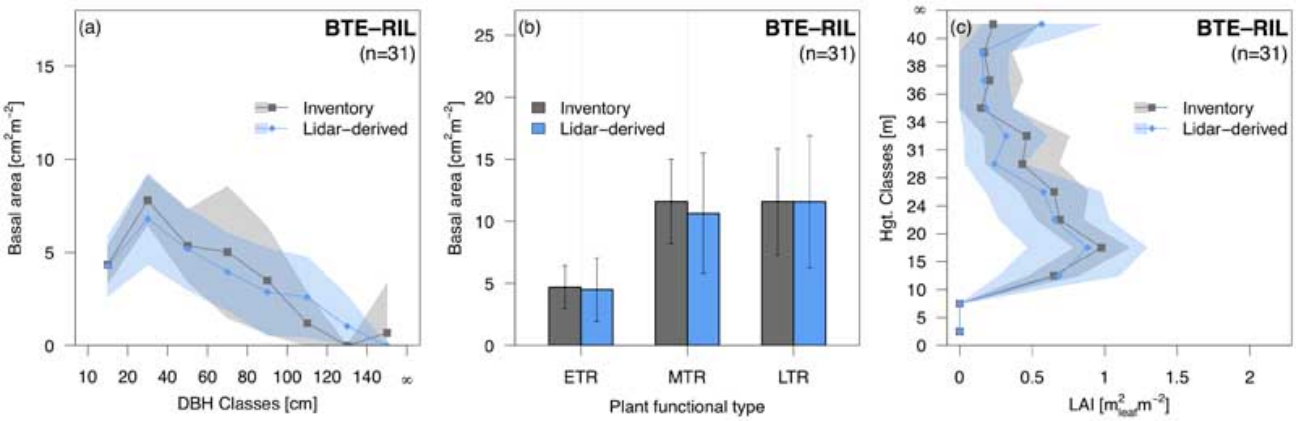

Figure S3. Assessment of airborne lidar initialization for Belterra (BTE). Comparison of (a) basal area distribution across diameter of breast height (DBH) classes, (b) basal area distribution among plant functional types (PFTs), and (c) leaf area index distribution as a function of height, for reduced-impact logging (RIL, the only disturbance type with $n > 20$ plots in BTE). Plant functional types are early-successional tropical tree (ETR), mid-successional tropical tree (MTR) and late-successional tropical tree (LTR). Grey points and bars are obtained from forest inventory plots, and blue points and bars are obtained from the airborne lidar initialization using a 612-fold regional cross-validation (i.e. excluding all plots from region in the calibration stage). Bands around points and whiskers correspond to the standard deviation either across all plots in the same category (inventory) or across all plots and replicates (lidar).

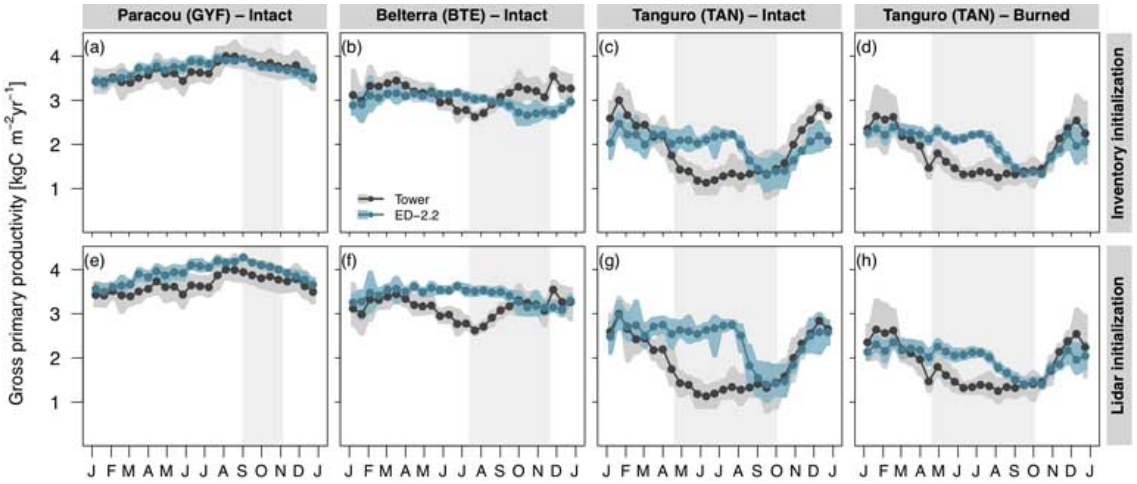

Figure S4. Model assessment of gross primary productivity. Fortnightly averages of gross primary productivity at (a,e) Paracou (GYF), intact forest; (b,f) Belterra (BTE), intact forests; (c,g) Tanguro (TAN), intact forests; (d,h) Tanguro (TAN), burned forests, initialized with (a-d) forest inventory plots and (e-h) airborne lidar. Fortnightly averages for both ED-2.2 and tower estimates were calculated using only hours with available data from the tower, and were integrated by obtaining the mean diurnal cycle then averaging the mean diurnal cycle to avoid biases due to data gaps. Bands around the averages correspond to the 95% confidence interval of the means, obtained through bootstrap. The grey rectangle in the background corresponds to the average dry season.

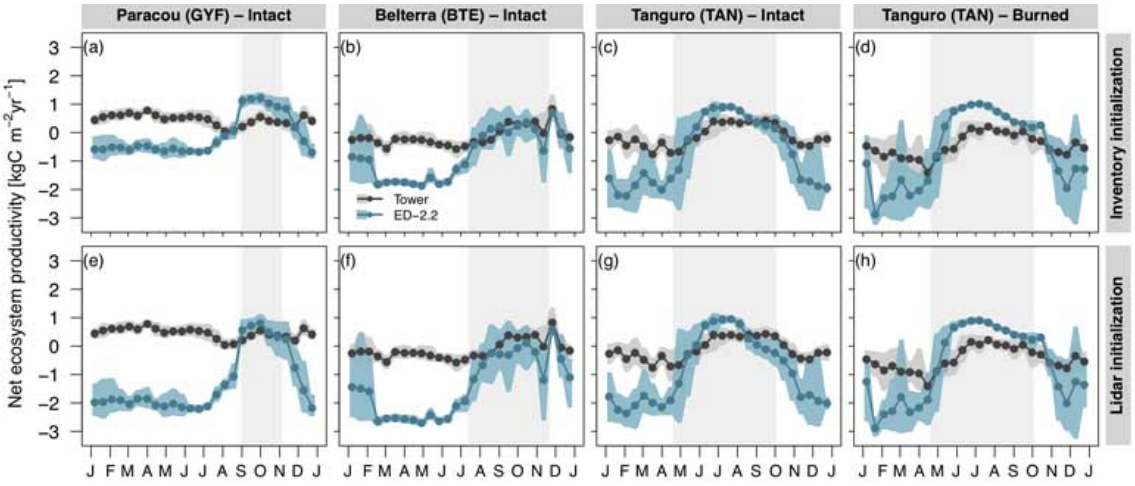

Figure S5. Model assessment of net ecosystem productivity. Fortnightly averages of net ecosystem productivity at (a,e) Paracou (GYF), intact forest; (b,f) Belterra (BTE), intact forests; (c,g) Tanguro (TAN), intact forests; (d,h) Tanguro (TAN), burned forests, initialized with (a-d) forest inventory plots and (e-h) airborne lidar. Positive fluxes mean net uptake. Fortnightly averages for both ED-2.2 and tower estimates were calculated using only hours with available data from the tower, and were integrated by obtaining the mean diurnal cycle then averaging the mean diurnal cycle to avoid biases due to data gaps. Bands around the averages correspond to the 95% confidence interval of the means, obtained through bootstrap. The grey rectangle in the background corresponds to the average dry season.

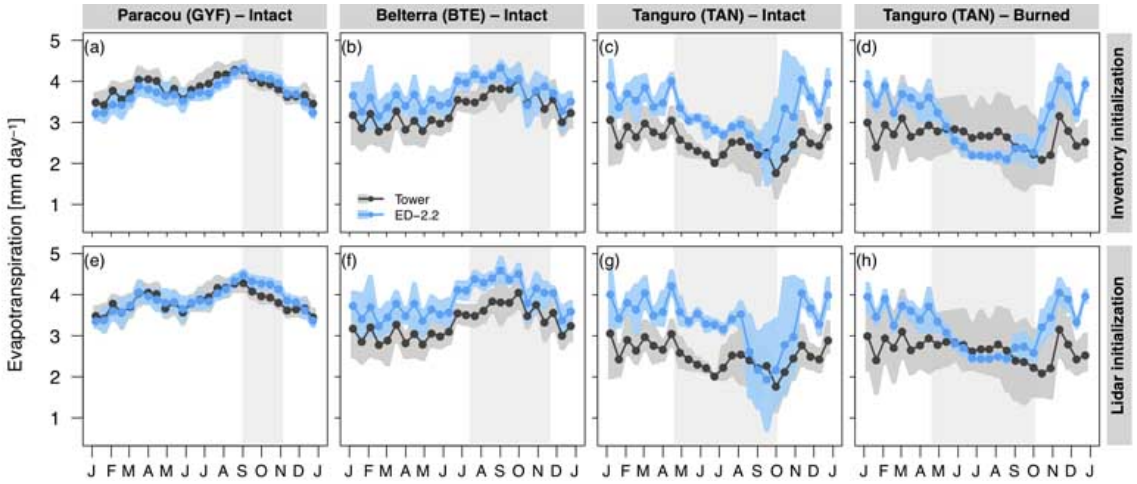

Figure S6. Model assessment of evapotranspiration. Fortnightly averages of water heat flux at (a,e) Paracou (GYF), intact forest; (b,f) Belterra (BTE), intact forests; (c,g) Tanguro (TAN), intact forests; (d,h) Tanguro (TAN), burned forests, initialized with (a-d) forest inventory plots and (e-h) airborne lidar. Fortnightly averages for both ED-2.2 estimates and tower measurements were calculated using only hours with available data from the tower, and were integrated by obtaining the mean diurnal cycle then averaging the mean diurnal cycle to avoid biases due to data gaps. Bands around the averages correspond to the 95% confidence interval of the means, obtained through bootstrap. The grey rectangle in the background corresponds to the average dry season.

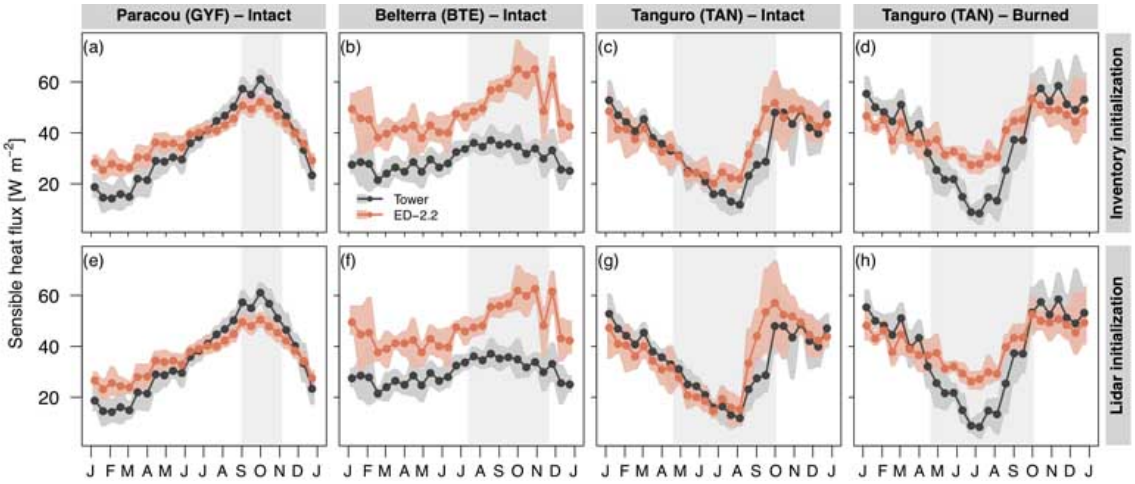

Figure S7. Model assessment of sensible heat flux. Fortnightly averages of sensible heat flux at (a,e) Paracou (GYF), intact forest; (b,f) Belterra (BTE), intact forests; (c,g) Tanguro (TAN), intact forests; (d,h) Tanguro (TAN), burned forests, initialized with (a-d) forest inventory plots and (e-h) airborne lidar. Fortnightly averages for both ED-2.2 estimates and tower measurements were calculated using only hours with available data from the tower, and were integrated by obtaining the mean diurnal cycle then averaging the mean diurnal cycle to avoid biases due to data gaps. Bands around the averages correspond to the 95% confidence interval of the means, obtained through bootstrap. The grey rectangle in the background corresponds to the average dry season.

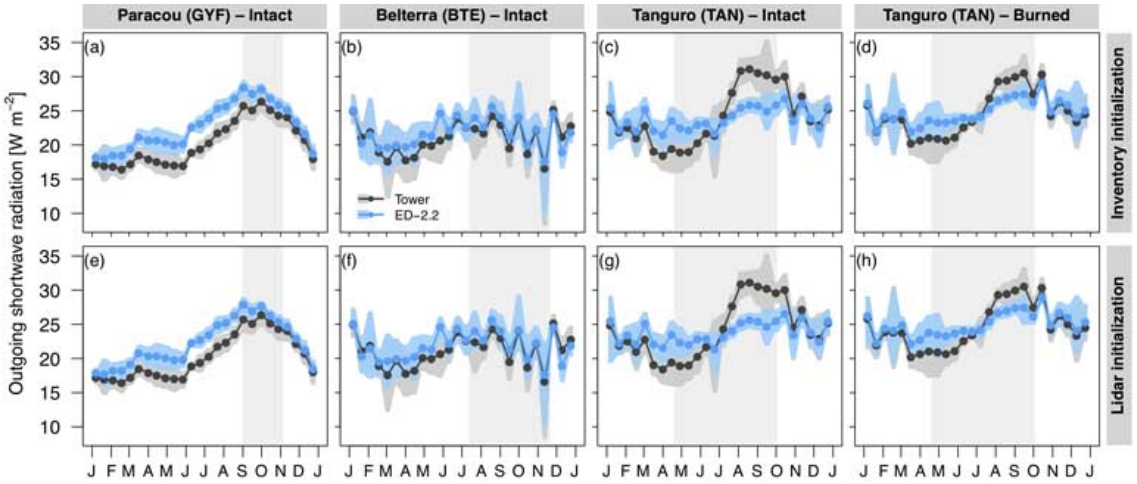

Figure S8. Model assessment of outgoing shortwave radiation. Fortnightly averages of outgoing shortwave radiation at (a,e) Paracou (GYF), intact forest; (b,f) Belterra (BTE), intact forests; (c,g) Tanguro (TAN), intact forests; (d,h) Tanguro (TAN), burned forests, initialized with (a-d) forest inventory plots and (e-h) airborne lidar. Fortnightly averages for both ED-2.2 estimates and tower measurements were calculated using only hours with available data from the tower, and were integrated by obtaining the mean diurnal cycle then averaging the mean diurnal cycle to avoid biases due to data gaps. Bands around the averages correspond to the 95% confidence interval of the means, obtained through bootstrap. The grey rectangle in the background corresponds to the average dry season.

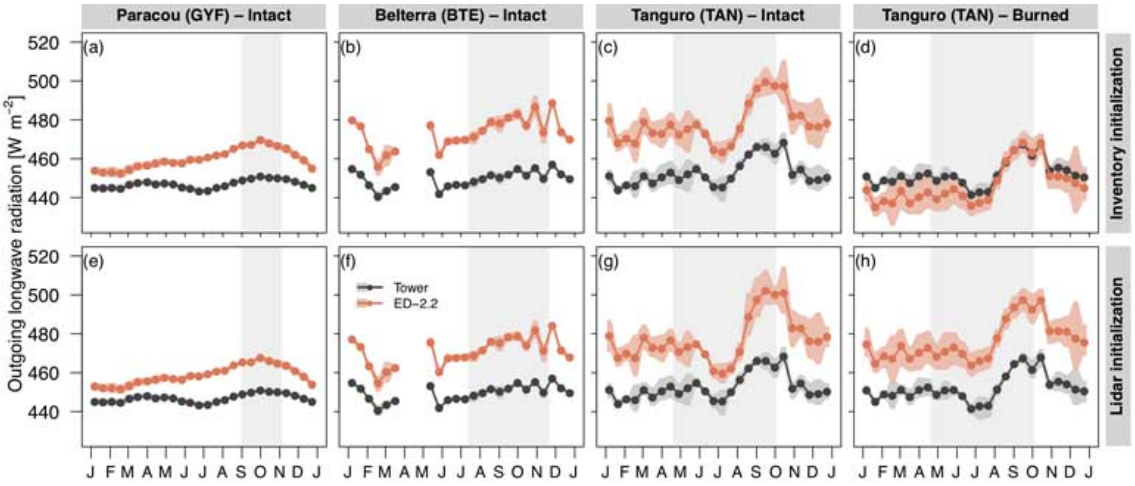

Figure S9. Model assessment of outgoing longwave radiation. Fortnightly averages of outgoing longwave radiation at (a,e) Paracou (GYF), intact forest; (b,f) Belterra (BTE), intact forests; (c,g) Tanguro (TAN), intact forests; (d,h) Tanguro (TAN), burned forests, initialized with (a-d) forest inventory plots and (e-h) airborne lidar. Fortnightly averages for both ED-2.2 estimates and tower measurements were calculated using only hours with available data from the tower, and were integrated by obtaining the mean diurnal cycle then averaging the mean diurnal cycle to avoid biases due to data gaps. Missing fortnightly periods at BTE did not have sufficient measurements to characterize the entire diurnal cycle. Bands around the averages correspond to the 95% confidence interval of the means, obtained through bootstrap. The grey rectangle in the background corresponds to the average dry season.

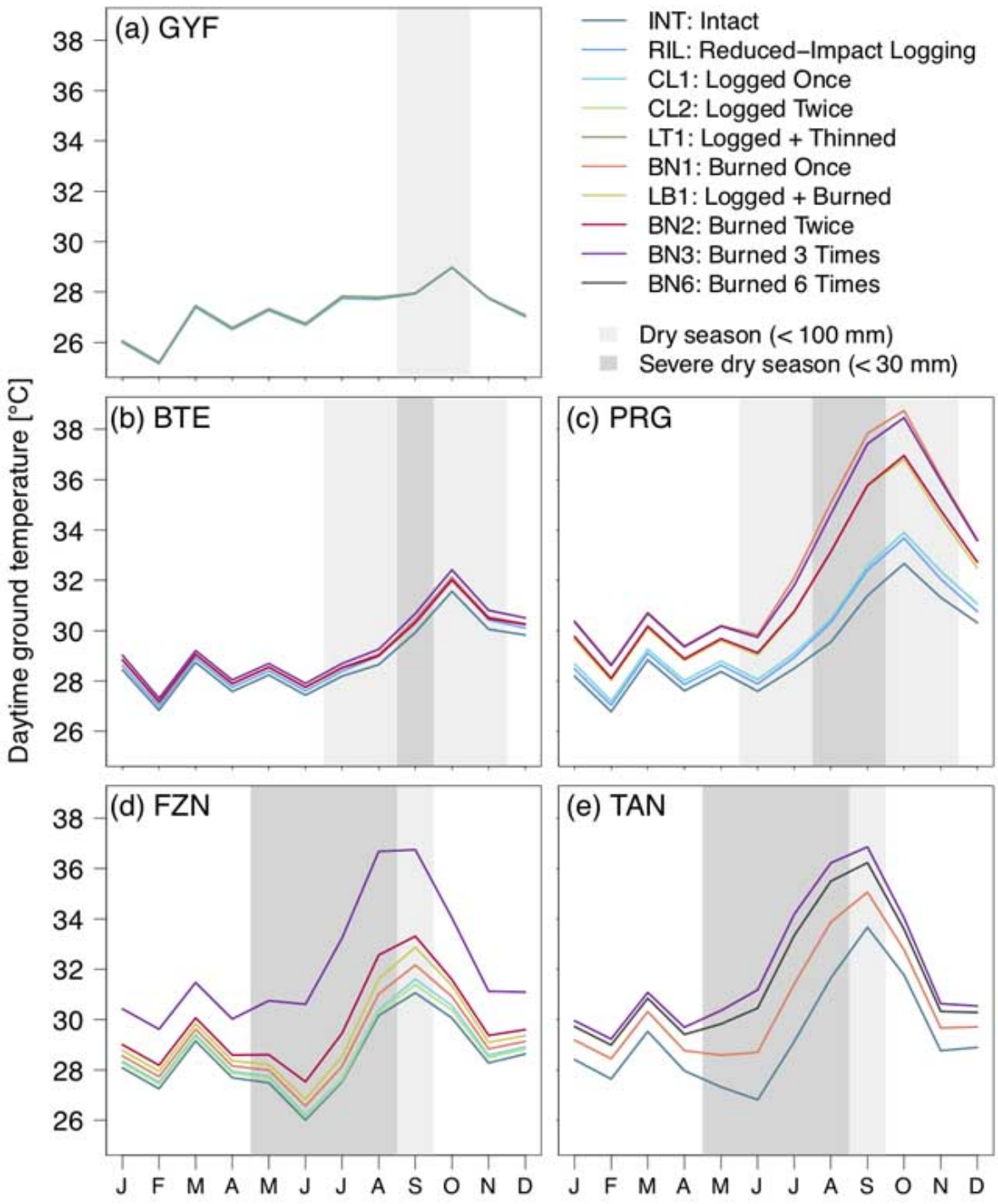

Figure S10. Multi-decadal average daytime ground temperate as a function of region and degradation. Monthly means of ground temperature (1980–2016), simulated by ED-2.2 and driven by MERRA-2 and MSWEP-2.2 for (a) Paracou (GYF), (b) Belterra (BTE), (c) Paragominas (PRG), (d) Feliz Natal (FZN), and (e) Tanguro (TAN), aggregated by degradation history (lines). Grey rectangles in the background correspond to the average dry season.

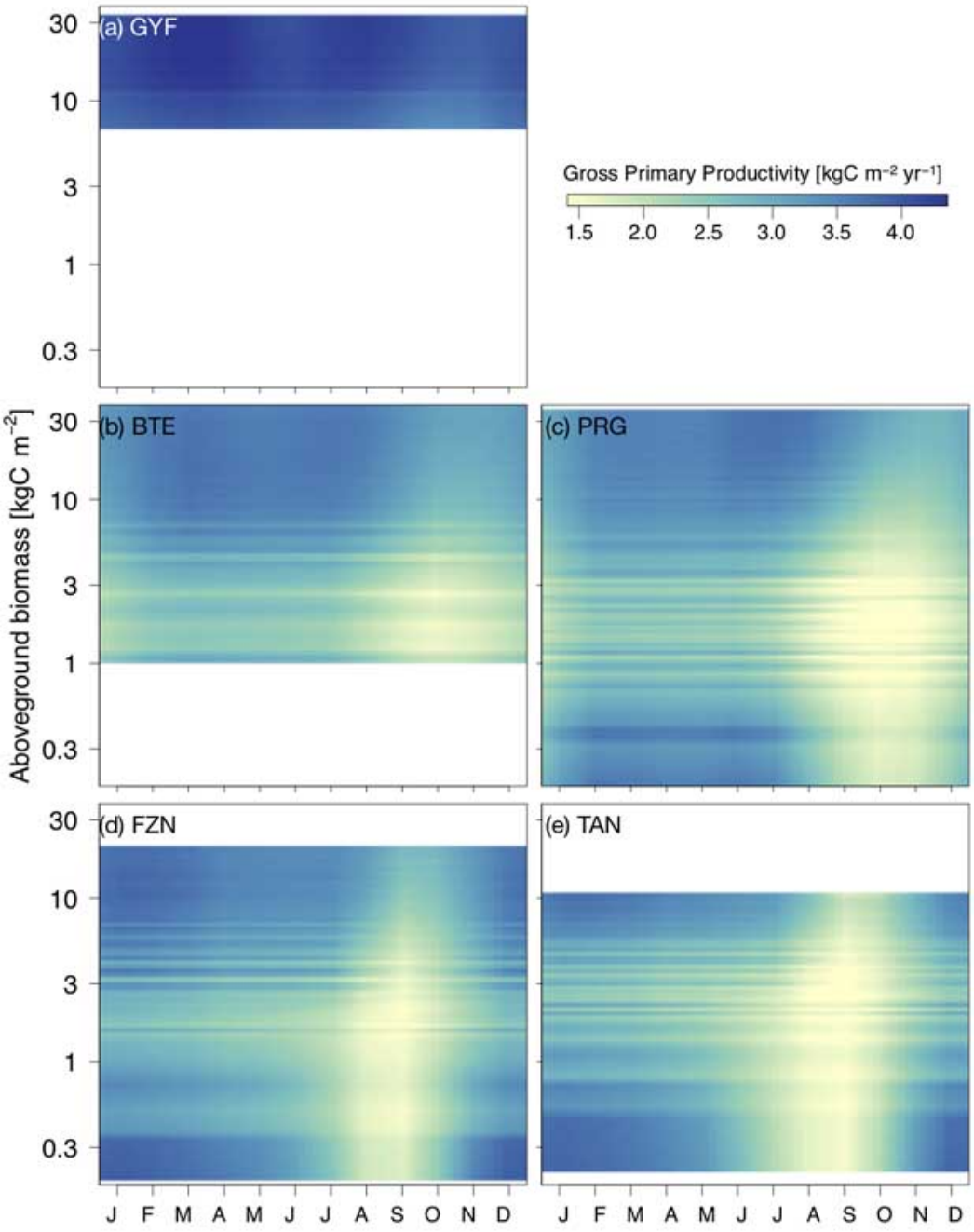

Figure S11. Monthly mean daytime gross primary productivity as a function of region and local (patch) aboveground biomass. Monthly averages correspond to the 1980–2016 period, simulated by ED-2.2 for (a) Paracou (GYF), (b) Belterra (BTE), (c) Paragominas (PRG), (d) Feliz Natal (FZN), and (e) Tanguro (TAN), and the y axis corresponds to the aboveground biomass for each patch, linearly interpolated for visualization. White areas are outside the range of biomass of each region and thus excluded.

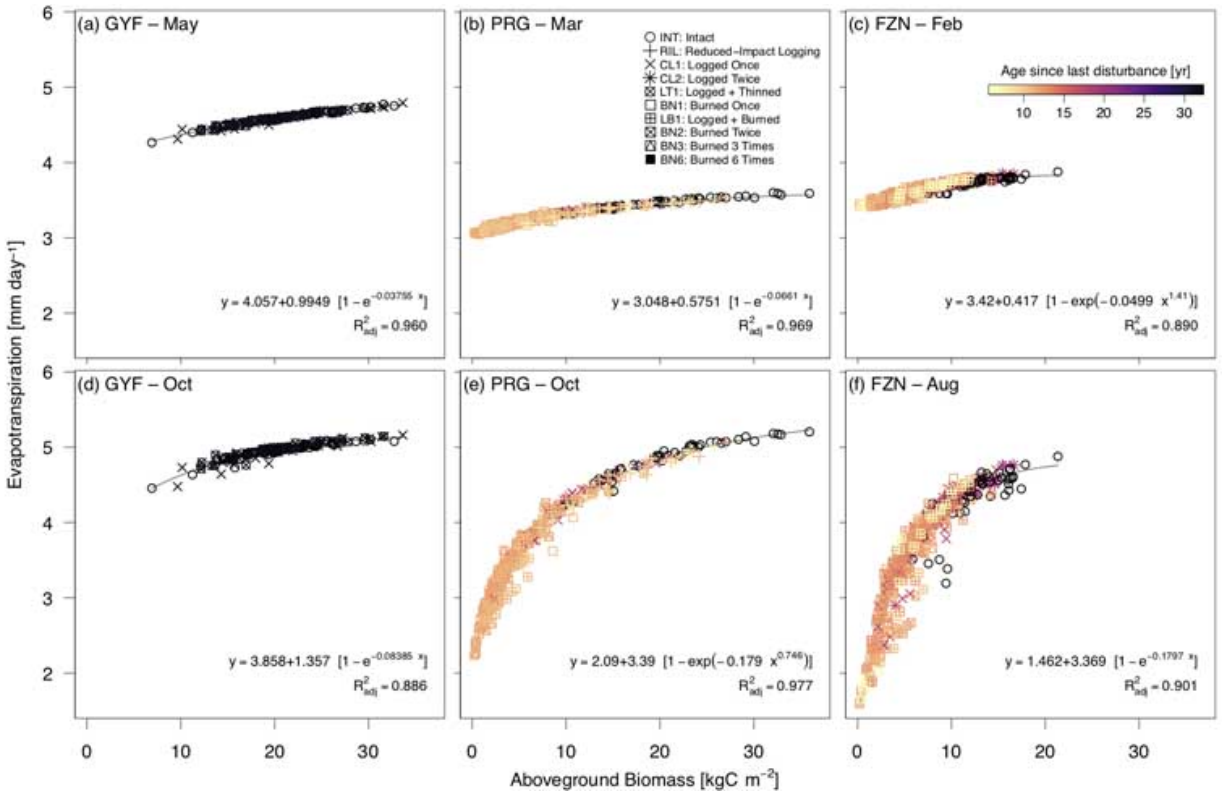

Figure S12. Variability of evapotranspiration (ET) as a function of local (patch) aboveground biomass (AGB). Scatter plot of AGB (x axis) and water flux (y axis) at sites (a,d) Paracou (GYF), (b,e) Paragominas (PRG), (c,f) Feliz Natal (FZN), for (a-c) the peak of wet season — May (GYF), March (PRG), and February (FZN) — and (d-f) peak of dry season — October (GYF and PRG), and August (FZN). Each point represents the 1980–2016 average ET of each patch solved by ED-2.2; point shapes correspond to the disturbance history, and point colors represent the time between the last disturbance (undetermined for intact forests) and lidar data acquisition. Curves correspond to non-linear least squares fits of the most parsimonious function, defined from Bayesian Information Criterion (?, ?), between shifted exponential or shifted Weibull functions.

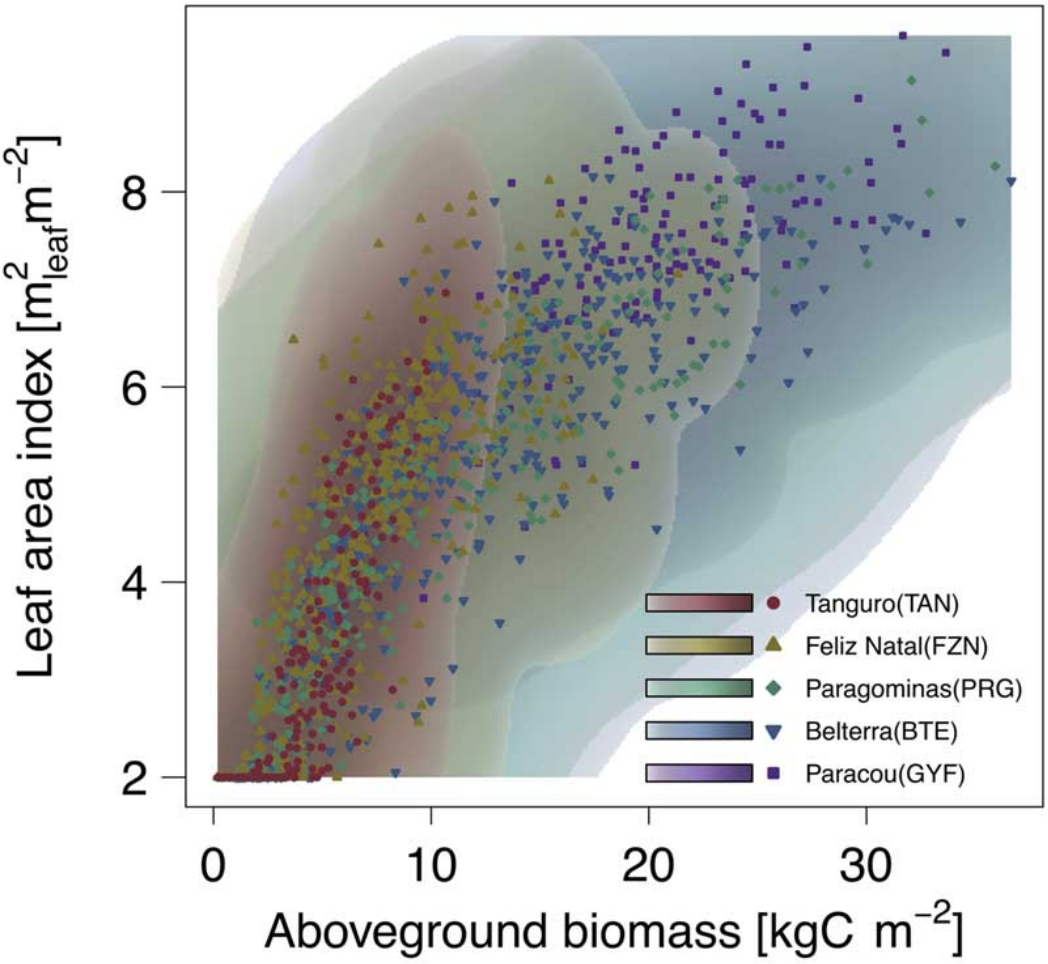

Figure S13. Leaf area index as a function of aboveground biomass. Scatter plot shows the leaf area index (x axis) and aboveground biomass (y axis) for each simulated patch across all regions. Density cloud (background color) was produced through a bi-dimensional kernel density estimator; points are the averages used to generate each density cloud. Color ramps (logarithmic) range from $0.1 - 100\%$ of the maximum computed scale.

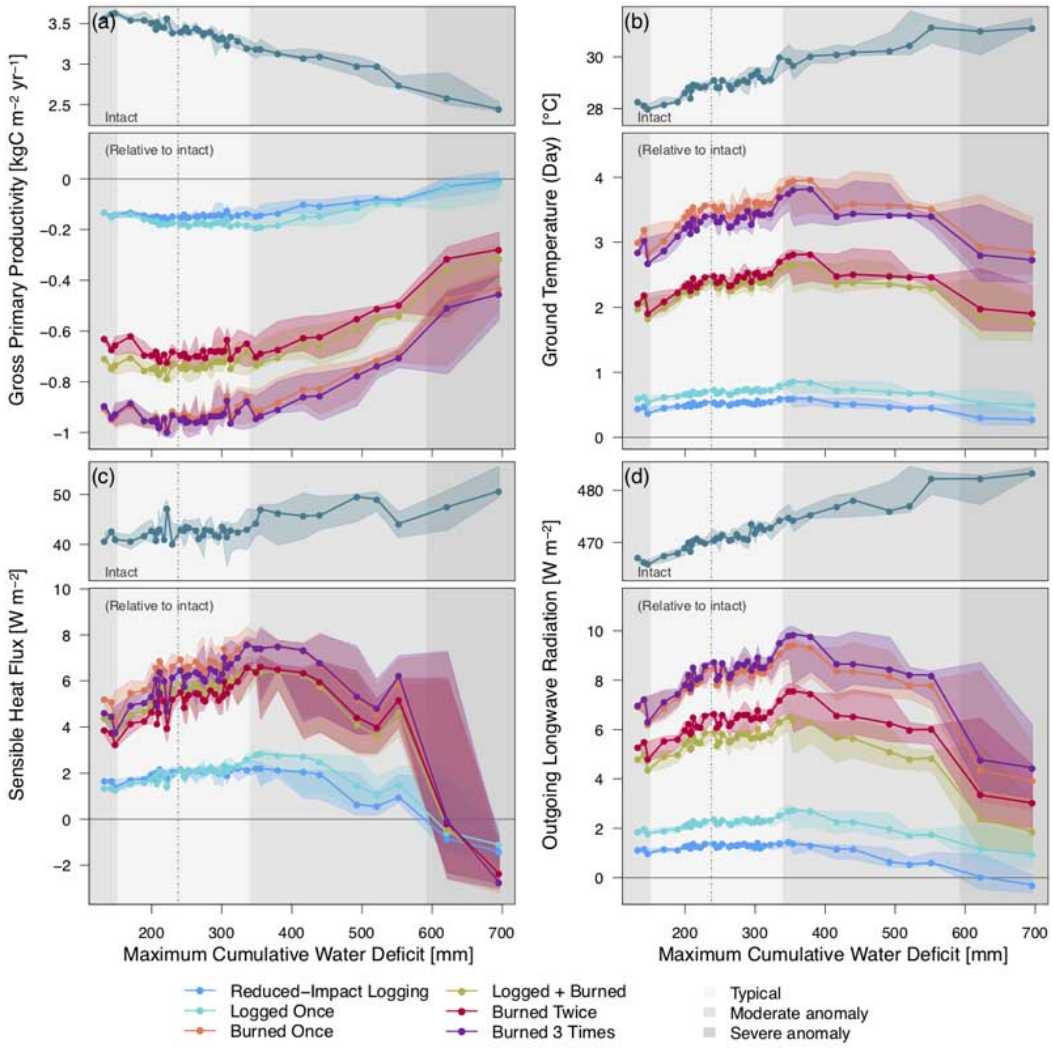

Figure S14. Response of the carbon and energy cycle components across a forest degradation gradient and drought severity in Paragominas (PRG). Selected components: (a) gross primary productivity, (b) daytime ground temperature, (c) sensible heat flux, and (d) outgoing longwave radiation. Points correspond to the median value of 12-month running averages, aggregated into 40 quantiles along the range of maximum cumulative water deficit (MCWD). Bands around the points correspond to the 95% range within each MCWD bin. Top panels are the absolute value for intact forests, and bottom panels are the absolute difference between degraded and intact forests. Background shades denote the MCWD anomaly: light grey – 68% range around the median (dot-dash vertical line); intermediate grey – 95% range; dark grey – anomalies exceeding the 95% range.

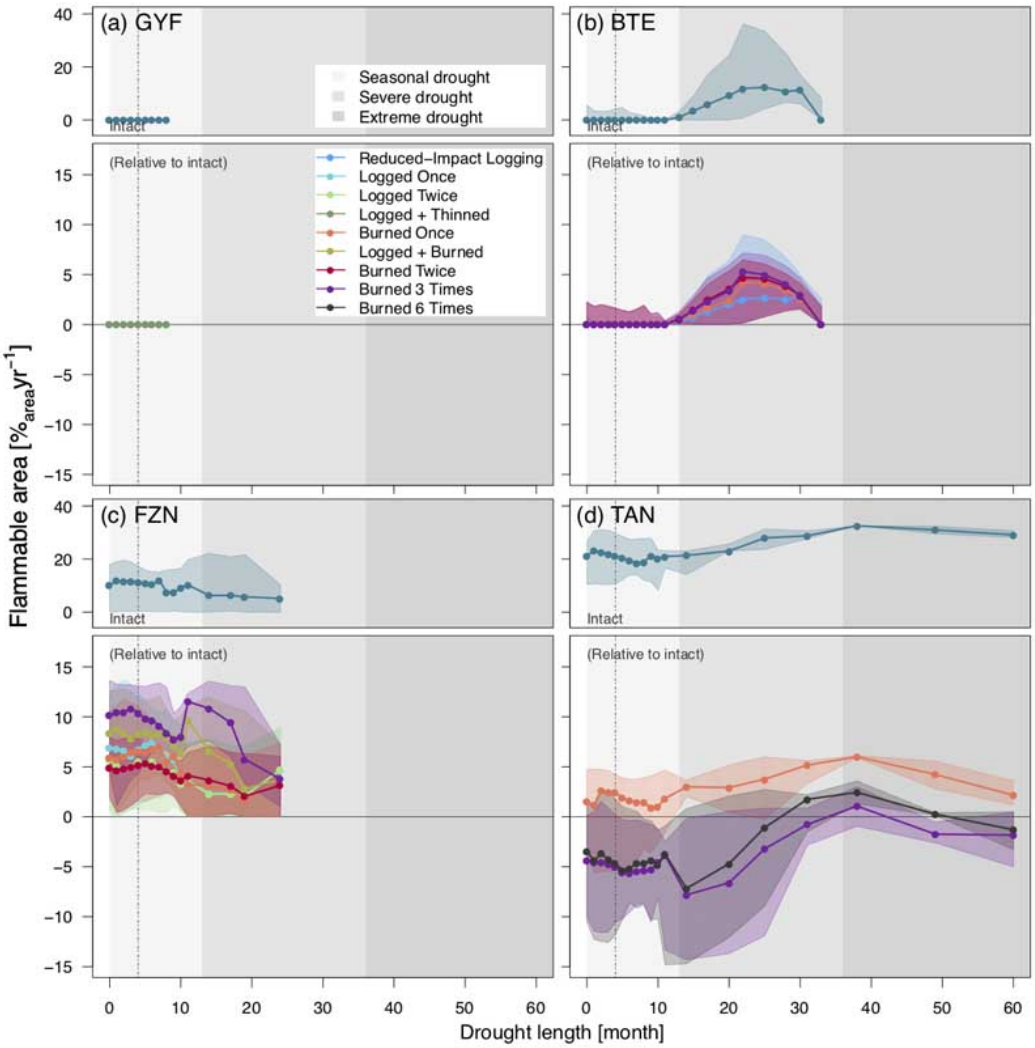

Figure S15. Flammable area as a function of degradation history and drought length (number of consecutive months with water deficit in excess of 20 mm) for regions (a) Paracou (GYF), (b) Belterra (BTE), (c) Feliz Natal (FZN), and (d) Tanguro (TAN). Points correspond to the median value of 12-month running averages, aggregated into quantiles along the drought length. Bands around the points correspond to the 95% range within each drought length bin. Top panels are the absolute value for intact forests, and bottom panels are the absolute difference between degraded and intact forests. Background shades denote drought-length classes used in the text: seasonal (light gray, less than 12 months); severe (intermediate gray, 12–36 months); extreme (dark grey; more than 36 months).

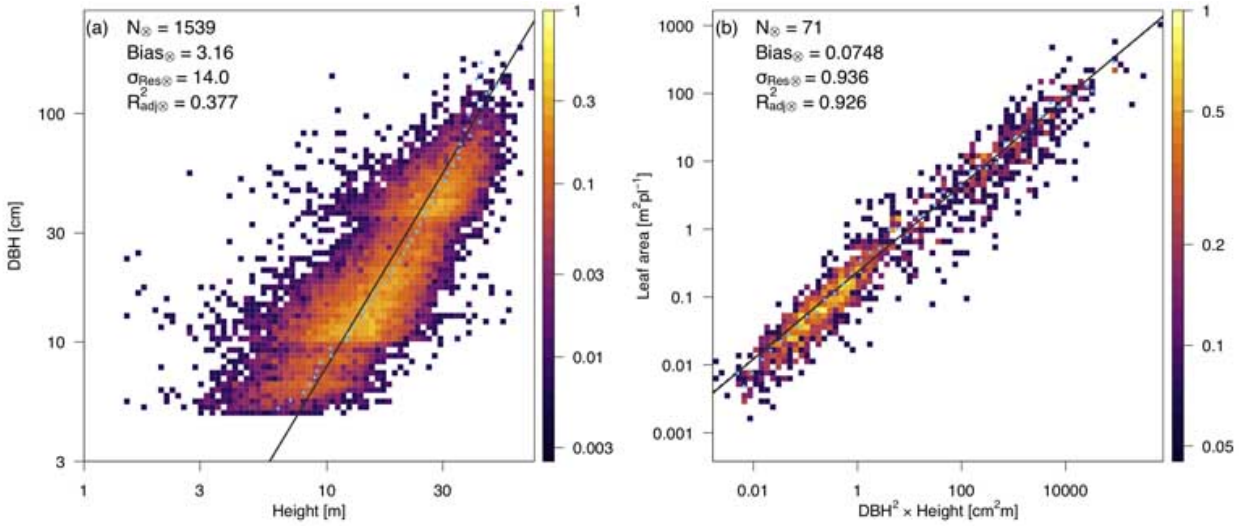

Figure S16. Fit of the allometric equations developed for the airborne lidar initialization and for ED-2.2 simulations. (a) Diameter at breast height (D) as a function of tree height (H); line corresponds to the standardized major axis equation defined by Equation (S1). (b) Individual leaf area (L) as a function of size ($D^2\,H$). Shaded background corresponds to the density of observed points. The results of the binned sampling with the lowest root mean square error are also shown: blue dots correspond to the binned sampled points used for the model fitting, black lines are the fitted model, and the goodness-of-fit metrics for the cross validation are shown for reference.

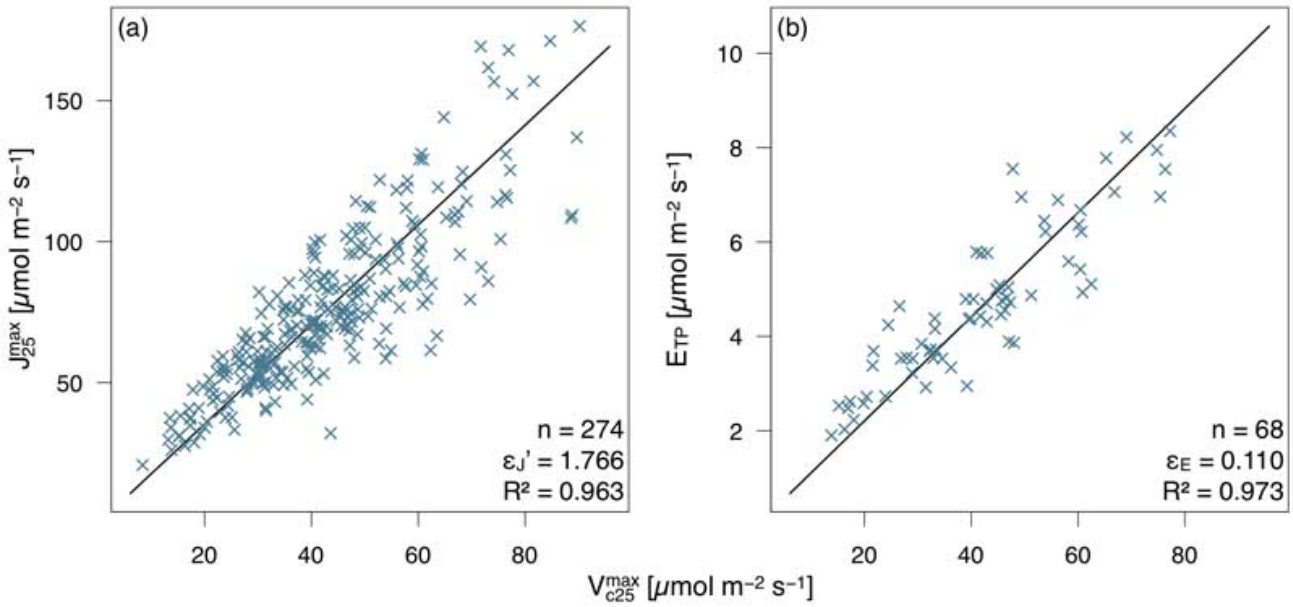

Figure S17. Scatter plots of (a) maximum electron transport rate at 25°C ($J_{25}^{\max}$) and (b) triose phosphate utilization rate (E^{TP}) as functions of maximum carboxylation rate at 25°C ($C_{c25}^{\max}$). Data were pooled from ? (?). The slopes ε'_J and ε_E were obtained by fitting standardized major axes (SMA) and imposing zero intercept. The number of points (N), the slope of the SMA line (ε'_J and ε_E, respectively), and the R^2 for the SMA curve are also shown for reference.

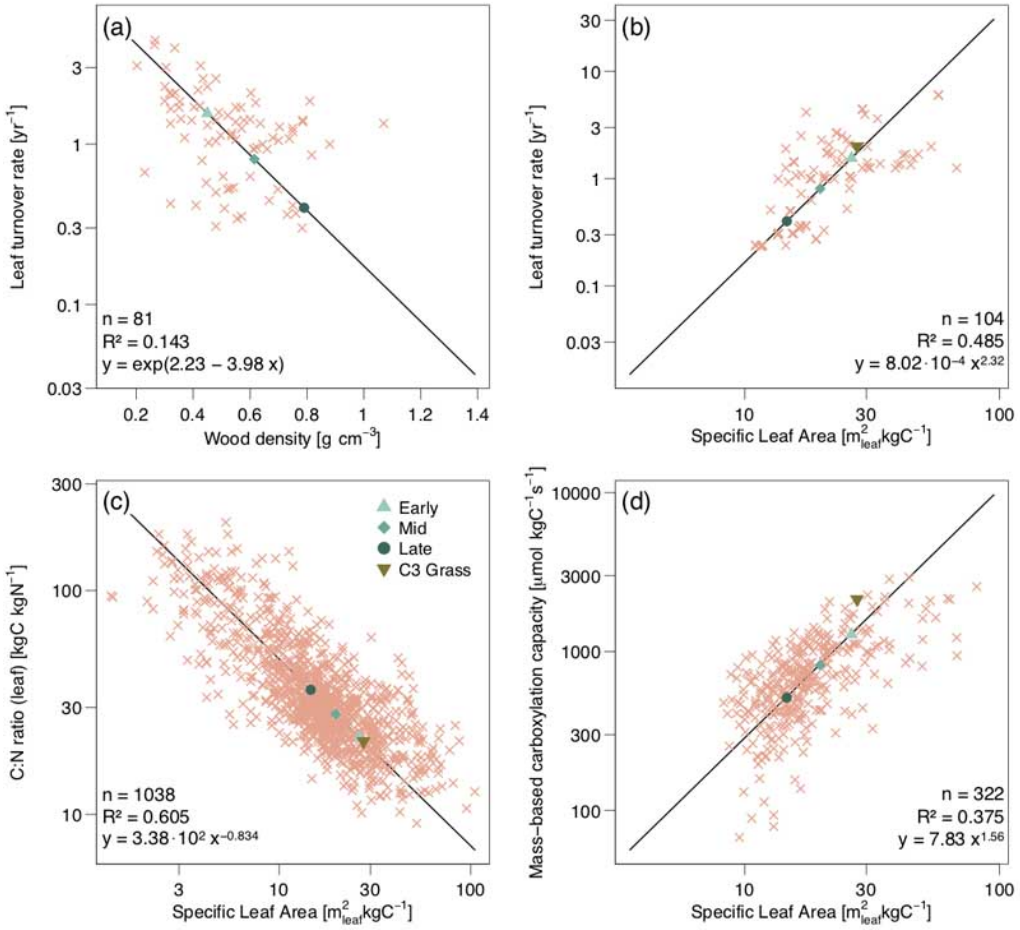

Figure S18. Scatter plots of trait relationships obtained from multiple studies and trait data bases, including GLOPNET and TRY (?, ?, ?, ?, ?, ?, ?, ?, ?, ?, ?). (a) Wood density and leaf turnover rate; and specific leaf area (SLA) against (b) leaf turnover rate; (c) leaf carbon:nitrogen ratio; and (d) mass-based maximum carboxylation capacity. For panel (a), values were aggregated to species to increase sample size, otherwise individual measurements were used. Black line is the fitted standardized major axes, and the equations along with the number of points (n) and squared correlation (R^2) are shown for reference. Values for each PFT are shown in the plot for reference. Grasses are included, but their fitted relationship were carried out separately for the relationships shown in panels (b) and (d).

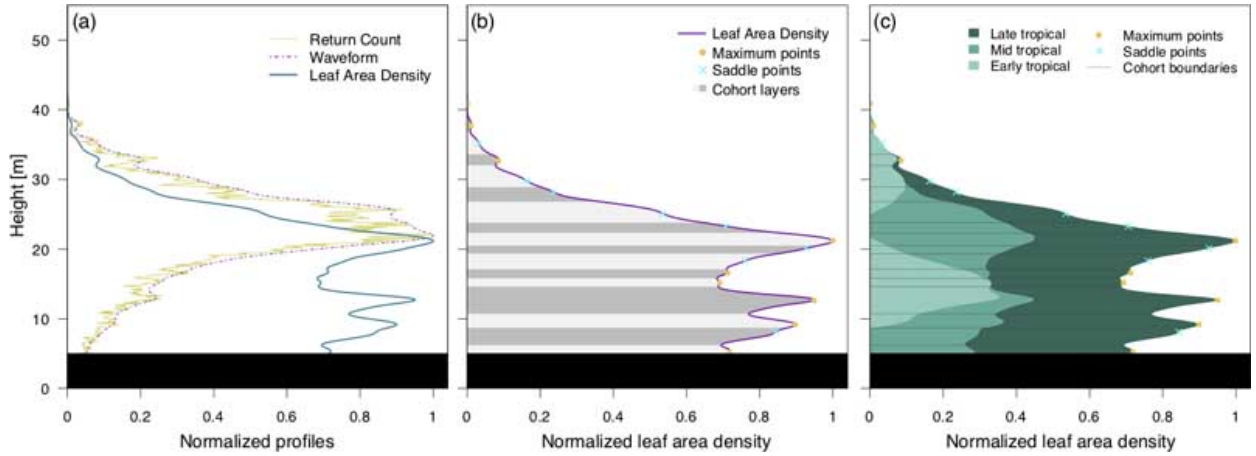

Figure S19. Example of how cohorts are obtained from the vertical distribution of returns, from one 50×50 m column at Paracou (GYF). (a) Thin lines: vertical profiles of return counts (X_v; Eq. S26); dot-dashed lines: waveform function (E_v; Eq. S25); thick lines: leaf area density ($\lambda^\star$; Eq. S30). (b) Discrete layers based on the curve features of leaf area density (thick line); Circles are the local maximum points and crosses are the saddle points. Discrete cohort layers are shown in alternate background shades. (c) Plant functional type (PFT) and cohort attribution. Cohorts are defined by the cohort layers, and further split by the existing PFTs in each layer. The unscaled leaf area index of each cohort is defined by the integral of the curve between each discrete layer and within each plant functional group. Black rectangles near ground are the bottom layer that is excluded from the cohort attribution.

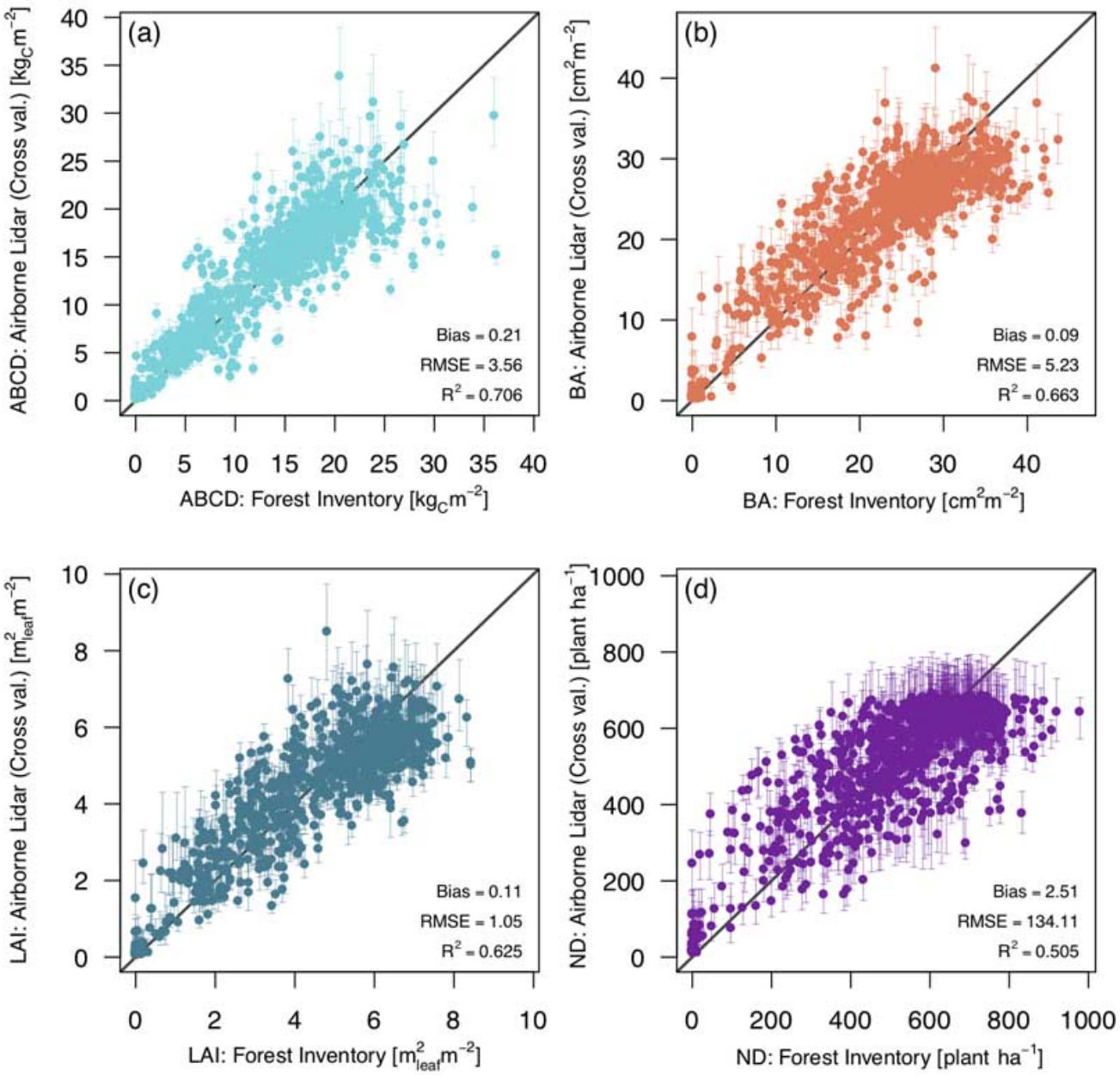

Figure S20. Comparison between forest inventory and airborne-lidar estimates of plot-level properties. (a) aboveground biomass carbon density (ABCD), (b) Basal area (BA), (c) (maximum, allometry-based) leaf area index and (d) stem number density (ND). For the airborne-lidar estimates, we show the average results from cross-validation: for each plot, we averaged all replicates which did not include the plot region in the model training step. Bars correspond to the 95% range of cross-validation predictions. Median bias, root mean square error (RMSE) and adjusted coefficient of determination (R^2_{adj}) for cross-validation predictions are shown for reference.

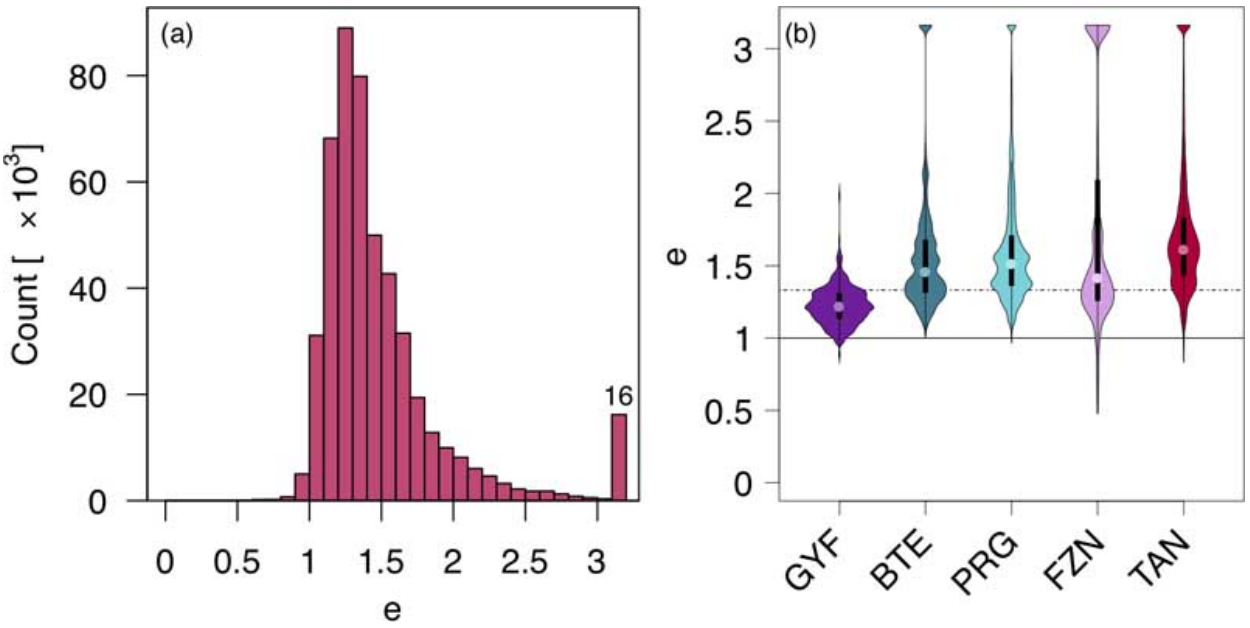

Figure S21. Statistics of the scaling factor e (Equation S55). (a) Histogram of e obtained from all plots and realizations of the regional cross-validation; the x axis was truncated at $\sqrt{10}$ to improve legibility, and the number of replicates exceeding this threshold is shown in the last bar of the histogram. (b) Violin plots for the five study regions: GYF – Paracou, BTE – Belterra, PRG – Paragominas, FZN – Feliz Natal, TAN – Tanguro; dot-dashed line represents the median ($e_{50} = 1.357$) used as the general scaling factor. The distribution was also truncated at $\sqrt{10}$, and the density function at the largest values along the y axis includes all values that exceed $\sqrt{10}$.

Table S1. Summary of model evaluation for eddy covariance tower sites Paracou (GYF) – Intact, Belterra (BTE) – Intact, Tanguro (TAN) – Intact, and Tanguro (TAN), Burned. In all cases, we only used daily averages for those days without gaps in tower observations or estimates. The following metrics are presented: number of daily averages observations (N), bias, root mean square error (RMSE), mean absolute error (MAE), Pearson's correlation coefficient (r). Units for bias, RMSE and MAE are presented in brackets; other metrics are dimensionless.

Variable	Metric	Paracou (GYF), Intact		Belterra (BTE), Intact		Tanguro (TAN), Intact		Tanguro (TAN), Burned	
		Inventory	Lidar	Inventory	Lidar	Inventory	Lidar	Inventory	Lidar
Gross Primary Productivity $\left[\mathrm{kgC\,m^{-2}\,yr^{-1}}\right]$	N	2305	2305	884	884	262	262	245	245
	Bias	0.102	0.316	-0.104	0.313	-0.046	0.394	0.296	0.242
	MAE	0.395	0.476	0.430	0.497	0.673	0.781	0.622	0.575
	RMSE	0.514	0.602	0.529	0.607	0.803	0.976	0.725	0.677
	r	0.832	0.826	0.498	0.528	0.506	0.478	0.455	0.501
Net Ecosystem Productivity $\left[\mathrm{kgC\,m^{-2}\,yr^{-1}}\right]$	N	2305	2305	884	884	262	262	245	245
	Bias	-0.555	-1.719	-0.647	-1.287	-0.745	-0.834	0.149	0.0824
	MAE	1.04	1.98	0.96	1.46	1.22	1.31	1.03	0.971
	RMSE	1.18	2.27	1.13	1.72	1.56	1.60	1.31	1.26
	r	0.407	0.299	0.476	0.489	0.494	0.514	0.574	0.577
Evapotranspiration $\left[\mathrm{mm\,day^{-1}}\right]$	N	3001	3001	932	932	539	539	603	603
	Bias	-0.0077	0.117	0.374	0.541	0.687	0.825	-0.0622	0.174
	MAE	0.45	0.47	0.58	0.65	0.89	1.17	0.90	0.86
	RMSE	0.57	0.58	0.74	0.82	1.08	1.32	1.18	1.13
	r	0.820	0.820	0.767	0.793	0.722	0.681	0.453	0.476
Sensible heat flux $\left[\mathrm{W\,m^{-2}}\right]$	N	2064	2064	930	930	291	291	324	324
	Bias	0.46	-1.16	17.7	16.9	6.84	6.38	11.2	11.0
	MAE	7.49	7.51	17.9	17.0	12.9	13.4	18.3	17.8
	RMSE	9.49	9.42	20.2	19.3	16.7	19.0	21.1	20.5
	r	0.864	0.866	0.767	0.783	0.811	0.754	0.808	0.821
Outgoing shortwave radiation $\left[\mathrm{W\,m^{-2}}\right]$	N	3784	3784	158	158	1039	1039	1318	1318
	Bias	2.182	1.807	0.297	0.067	-0.173	-0.298	0.167	0.280
	MAE	2.34	2.04	1.24	1.23	2.80	2.85	1.83	1.81
	RMSE	2.70	2.41	1.70	1.68	3.43	3.51	2.23	2.20
	r	0.970	0.969	0.932	0.932	0.873	0.868	0.940	0.940
Outgoing longwave radiation $\left[\mathrm{W\,m^{-2}}\right]$	N	3943	3943	396	396	1039	1039	1318	1318
	Bias	13.1	11.8	23.9	21.4	25.5	24.8	-5.6	23.9
	MAE	13.1	11.8	23.9	21.4	25.5	24.8	7.6	23.9
	RMSE	14.3	13.0	24.9	22.2	26.6	26.6	9.4	25.2
	r	0.647	0.658	0.938	0.938	0.891	0.863	0.889	0.889

Table S2. Detailed information of each study region. Density corresponds to the average number of returns per unit area. For plots that used sub-plots to sample individuals with diameter at breast height $D < 35\,\text{cm}$, we provide the size of the sub-plot in parentheses. Ancillary regions and sites used only to establish the statistical models are shown in *italics*.

Region (Code)	Site	Coordinates	Lidar			Inventory		
			Area [ha]	Density [m^{-2}]	Date	Count	Size (Sub-Size) [m × m]	Date
Paracou (GYF)	GFE	5.28°N; 52.93°W	963[a]	22.4[a]	Sep 2013[a]	22	35 × 70 (16); 50 × 50 (6)[b]	Mar 2013
	PRC	5.27°N; 52.93°W				300	50 × 50[c]	Mar 2013
Belterra (BTE)	ANA	3.36°S; 55.00°W	989	20.11	Mar 2017	32	50 × 50	Jul 2015
	EBT	3.18°S; 54.88°W	1004	54.9	Apr 2015	14	50(5) × 50	Nov 2014
	TNF	2.86°S; 54.95°W	1048	19.3	Mar 2017	9	50 × 50	Dec 2015 – Mar 2016
	TSJ	3.13°S; 54.97°W	1012	30.0	Jul–Aug 2013	12	50 × 50	Sep 2013
Paragominas (PRG)	AND	2.55°S; 46.83°W	1000	38.2	Jun 2014	20	50(5) × 50	Aug 2013
	CAU	3.75°S; 48.48°W	1214	28.3	Jul 2012	85	20(2) × 125[d]	Jan–Mar 2012
	PAR	3.32°S; 47.53°W	1003	40.0	Jun 2014	39	20(2) × 125[d]	Mar–Apr 2013
	TAC[e]	2.77°S; 48.52°W	983	24.2	Nov 2013	13	50 × 50	May-Jun 2015
Feliz Natal (FZN)	FN2	11.86°S; 54.19°W	995	30.7	Mar 2016	7	50(5) × 50	Aug 2015
	FNA	12.50°S; 55.01°W	1200	38.3	Aug 2013	20	50 × 50	Oct 2013
	FNC	12.00°S; 54.20°W	903	15.2	Apr 2017	9	50(5) × 50	Aug 2015
	FND	12.27°S; 55.08°W	1099	13.2	Apr 2017	20	50(5) × 50	Aug 2015
Tanguro (TAN)	TGE	13.08°S; 52.38°W	1006[a]	13.1[a]	Aug 2012[a]	72	20(10) × 125[f]	Jun 2012
	TGW	13.09°S; 52.40°W				20	20(2) × 125[d]	Nov 2012
São Félix do Xingu (SFX)	*SX1*	6.41°S; 52.90°W	993	30.1	Aug–Sep 2012	9	40 × 40	Oct 2011
	SX2	6.60°S; 51.79°W	1005	30.1	Aug–Sep 2012	22	40 × 40	Aug 2012
Jamari (JAM)	*JAM*	9.12°S; 63.01°W	1673	31.0	Sep 2013	23	50(5) × 50	Dec 2013
Rio Branco (RBR)	*BON*	9.87°S; 67.29°W	600	33.4	Sep 2013	10	50(10) × 50	Jul 2014
	HUM	9.76°S; 67.65°W	501	66.7	Sep 2013	10	50(10) × 50	Jun–Jul 2014
	TAL	10.26°S; 67.98°W	500	40.7	May 2014	5	50(10) × 50	Jul 2014
Saracá Taquera (FST)	*FST*	1.62°S; 56.22°W	1021	32.9	Aug 2013	19	50(5) × 50	Nov 2013
Manaus (MAO)	*DUC*	2.95°S; 59.94°W	1248	22.7	Feb 2012	25	26(⋆) × 100[g]	Sep 2011

[a] Both sites were covered by the same airborne lidar survey.
[b] Original plot sizes 70 × 70 m (8), 50 × 100 m (1) and 100 × 100m (1), split in 35 × 70 m or 50 × 50 m blocks to be comparable with other areas.
[c] Original plot size 250 × 250 m, split in 50 × 50 m blocks to be comparable with other areas.
[d] Original transect size 20 × 500 m, split in 20 × 125 m blocks to be comparable with other areas.
[e] The lidar survey includes only second-growth forests and forest plantations, which are outside the scope of this study. All plots were located in second-growth forests.
[f] Original transect size 20 × 1500 m, split in 20 × 125 m blocks to be comparable with other areas. Sub-sampling was applied to trees with $D \leq 20\,\text{cm}$.
[g] Sampling effort varied depending on the D, following ? (?). Nominal plot size defined from the largest surveyed tree ($D = 128.5\,\text{cm}$).

Table S3. Configuration and parameters used in the simulations and described in Text S2. For parameters that are specific to each plant functional type (PFT), we use the format (x_{C4G}; x_{ETR}; x_{MTR}; x_{LTR}), for C_4 grasses, early-, mid-, and late-successional tropical trees, respectively.

Process	**Method**	
Integration scheme	4^{th} order Runge-Kutta	
Soil bottom boundary condition	Free drainage	
Leaf phenology	Evergreen	
Parameter	**Value**	**Units**
Biophysics time step	240	s
Number of soil layers	16	—
Depth of the deepest soil layer	10.50	m
Depth of the shallowest soil layer	0.04	m
Biomass:carbon ratio (β, all tissues)	2.0	$\mathrm{kg\,kgC^{-1}}$
Fine-root:leaf ratio (q_R)	1.0	$\mathrm{kg_{Root}\,kg_{Leaf}^{-1}}$
Empirical parameter (η_c; Equations S7 and S8)	0.886	—
Leaf (η_c; Equations S7 and S8)	0.886	—
Leaf:sapwood area ratio ($A_{L:S}$, Equation S7)	13513	$\mathrm{m^2_{Leaf}\,m^{-2}_{Sapwood}}$
Leaf:bark area ratio ($A_{L:B}$, Equation S8)	292523	$\mathrm{m^2_{Leaf}\,m^{-2}_{Bark}}$
Aboveground fraction (f_{AG})	0.7	—
Curvature parameter (φ)	0.7	—
Quantum yield of photosystem II (γ_{PSII})	0.85	—
Q_{10} factor for carboxylation (Q_V)	2.43	—
Q_{10} factor for electron transport (Q_J)	1.81	—
ε_J – Equation (S23)	1.766	—
$\varepsilon_{\mathrm{TP}}$ – Equation (S24)	0.110	—
Parameter f_c – Equation (S19)	0.3	—
Parameter f_h – Equation (S19)	0.6	—
Parameter T_c – Equation (S19)	288.15	K
Parameter T_h – Equation (S19)	310.65	K
PFT-dependent parameter	**Value**	**Units**
Wood density	(–; 0.45; 0.62; 0.79)	$\mathrm{g\,cm^{-3}}$
Bark density	(–; 0.44; 0.46; 0.45)	$\mathrm{g\,cm^{-3}}$
Specific leaf area	(27.6; 26.2; 19.7; 14.6)	$\mathrm{m^2_{Leaf}\,kgC^{-1}}$
Leaf turnover rate	(2.00; 1.56; 0.80; 0.40)	$\mathrm{yr^{-1}}$
Maximum carboxylation rate (V_{c15}^{max})	(21.2; 20.3; 17.3; 14.6)	$\mu\mathrm{mol\,m^{-2}\,s^{-1}}$
Leaf carbon:nitrogen ratio	(21.2; 22.1; 28.0; 36.0)	$\mathrm{kgC\,kgN^{-1}}$

Table S4. Summary goodness-of-fit statistics for fitted models for above-ground biomass carbon density (ABCD), basal area (BA), (maximum, allometry-based) leaf area index (LAI) and stem number density (ND), both for the full model (*Full*; all plots used for calibration) and the cross-validation (*X-Val*; the median statistics obtained from 1000 hierarchical bootstrap replicates (goodness-of-fit were assessed from plots in regions not included in the model training stage). The 68% range (equivalent to $\pm 1\sigma$ if the distribution was Gaussian) relative to the median is also shown. Bias, mean absolute error (MAE) and root mean square error (RMSE) are show in percentage relative to the average value of all plots (inventory-based), to simplify comparison across properties. The other statistics are: adjusted coefficient of determination (R^2_{adj}); Kolmogorov-Smirnov statistics (D_{KS}) and *p-value* (p_{KS}).

Statistics	ABCD		BA		LAI		ND	
	Full	X-Val	Full	X-Val	Full	X-Val	Full	X-Val
%Bias	0.0	$1.5^{+5.5}_{-5.6}$	0.0	$0.4^{+6.5}_{-7.4}$	0.0	$2.4^{+5.8}_{-12.6}$	0.0	$0.5^{+6.3}-6.1$
%MAE	17.8	$18.9^{+4.2}_{-3.1}$	15.8	$17.5^{+4.5}_{-3.0}$	15.7	$18.4^{+3.0}_{-2.6}$	18.2	$20.7^{+2.7}_{-4.1}$
%RMSE	25.2	$26.6^{+5.4}_{-4.9}$	20.9	$23.1^{+3.9}_{-3.9}$	20.7	$23.3^{+3.2}_{-2.8}$	24.1	$26.7^{+3.1}_{-5.1}$
R^2_{adj}	0.779	$0.706^{+0.080}_{-0.209}$	0.754	$0.66^{+0.10}_{-0.30}$	0.79	$0.63^{+0.13}_{-0.27}$	0.65	$0.50^{+0.18}_{-0.34}$
D_{KS}	0.049	$0.120^{+0.068}_{-0.045}$	0.086	$0.151^{+0.078}_{-0.052}$	0.087	$0.172^{+0.158}_{-0.062}$	0.18	$0.20^{+0.10}_{-0.06}$
p_{KS}	0.28	$0.066^{+0.363}_{-0.065}$	0.005	$0.018^{+0.245}_{-0.018}$	0.004	$0.013^{+0.230}_{-0.013}$	0.0000	$0.0017^{+0.0628}_{-0.0017}$